9-9-2010

Model electrode structures for studies of electrocatalyst degradation

Ronald Goeke

Ronald Steven Goeke
Candidate

Chemical and Nuclear Engineering
Department

This dissertation is approved, and it is acceptable in quality and form for publication:

Approved by the Dissertation Committee:

, Chairperson

MODEL ELECTRODE STRUCTURES FOR STUDIES OF ELECTROCATALYST DEGRADATION

BY

RONALD S. GOEKE

B.S. Chemical Engineering, New Mexico State University, 1985
M.S., Chemical Engineering, University of New Mexico, 2003

DISSERTATION

Submitted in Partial Fulfillment of the
Requirements for the Degree of

Doctor of Philosophy
Engineering

The University of New Mexico
Albuquerque, New Mexico

July, 2010

DEDICATION

To my wonderful wife, Susan. Thank you for believing in me. None of this would have been possible without your love and support. To my granddaughter Zoey, you always put a smile on my face. Thank you for being in my life.

-Ron

ACKNOWLEDGEMENTS

This work was made possible by the support of my advisors Professor Abhaya Datye and Professor Plamen Atanassov. I am eternally thankful for their technical guidance and all that I have learned from them throughout this research.

Thank you to all the support I received from friends at Sandia National Laboratories. Specifically the support of time and equipment from: Mike Saavedra, Cathy Sobczak, David Saiz and Dennis Yazzie.

I also want to thank Neil Lapetina, Bob Poole and Gil Herrera for the letters of support when I started on this journey.

I would like to thank Dr. Shengxiang Ji and Professor Paul Nealey at the University of Wisconsin for their expertise and support with the block copolymers.

I would like to acknowledge financial support from the National Science Foundation under grants IIP-0718781 and EEC04-36455 to the I/UCRC Ceramic Composite Materials Center.

I would like to acknowledge the financial and time support from my employer Sandia National Laboratories through my enrollment in the University Part Time program.

MODEL ELECTRODES FOR STUDIES OF ELECTROCATALYST DEACTIVATION

BY

RONALD S. GOEKE

ABSTRACT OF DISSERTATION

Submitted in Partial Fulfillment of the
Requirements for the Degree of

Doctor of Philosophy
Engineering

The University of New Mexico
Albuquerque, New Mexico

July, 2010

MODEL ELECTRODE STRUCTURES FOR STUDIES OF ELECTROCATALYST DEGRADATION

By

Ronald S. Goeke

B.S., Chemical Engineering, New Mexico State University, 1985
M.S., Chemical Engineering, University of New Mexico, 2003
Ph.D., Engineering, University of New Mexico, 2010

ABSTRACT

Proton exchange membrane fuel cells (PEMFCs) are being extensively studied as power sources because of their technological advantages such as high energy efficiency, high energy and power densities, environmental friendliness, low noise, rapid refueling, and fuel flexibility. The most effective catalyst in these systems consists of nanoparticles of Pt or Pt-based alloys on carbon supports. Understanding the role of the nanoparticle size and structure on the catalytic activity and degradation is needed to optimize the fuel cell performance and reduce the noble metal loading. Electrocatalyst degradation is believed to occur by four mechanisms; particle sintering (Ostwald ripening and migration and coalescence), carbon corrosion and catalyst dissolution. Increasing catalyst layer durability is becoming a major challenge and a growing focus of research attention in PEM fuel cell durability studies. Typical model systems utilized to study catalyst activity are single crystal materials or bulk polycrystalline materials which are not useful for studying catalyst degradation mechanisms as no particles exist. Powder catalysts on RDE electrodes can be

very useful for catalyst evaluation and general degradation studies, but contain a distribution of particle sizes on a high surface area support that make them difficult to analyze.

We addressed this gap in research needs with the development of model electrode structures, which consist of catalytic nanoparticles on planar model supports for easy analysis. We improve upon this basic concept by engineering the nanoparticle dispersion directly on the planar carbon support as ordered arrays. Ordered nanoparticle arrays of controlled size and spacing were fabricated by adapting a previously developed templating techniques using diblock copolymers. These well defined model electrode structures were applied to the study of electrocatalyst degradation and the dissolution reaction of Pt catalyst in acid medium. It is shown that these electrodes can be transferred between the electrochemical cell and SEM imaging without impact on the individual Pt nanoparticles. Control over the Pt particle size is demonstrated by changing the metal loading, annealing conditions and diblock copolymer templating.

Pt nanoparticle sintering on many of these surfaces was observed to proceed through the formation of Pt nanowires. Degradation mechanisms of particle detachment were observed specifically under the harsh potential cycling conditions ($0 - 1.4V_{RHE}$) used for the initial conditioning and when potential is cycled in oxygen saturated electrolyte. Ostwald ripening and dissolution were observed through the use of particle size distributions; particle migration and coalescence was observed upon close examination of repeat SEM images taken of the same area. For the first time ordered arrays of Pt nanoparticles on glassy carbon electrode have been fabricated and tested.

Table of Contents

ABSTRACT ..... **vii**

TABLE OF CONTENTS ..... **ix**

LIST OF FIGURES ..... **xi**

CHAPTER 1 INTRODUCTION **1**
1.1 Proton Exchange Membrane Fuel Cells (PEMFC) 3

CHAPTER 2 DURABILITY AND DEGRADATION **10**
2.1 Catalyst Surface Area Loss Mechanisms 11
2.1.1 Ostwald ripening 12
2.1.2 Migration and coalescence 14
2.1.3 Carbon corrosion 16
2.1.4 Dissolution 18
2.2 Nernst Equation and the Pt Pourbaix Diagram 20
2.2.1 Application of the Nernst Equation to Nanoparticles 23
2.3 Previous Sintering Studies 25

CHAPTER 3 RESEARCH OBJECTIVES **28**

CHAPTER 4 EXPERIMENTAL METHODOLOGY **30**
4.1 Cyclic Voltammetry 30
4.2 Rotating Disk Electrode 31
4.3 EQCM 35
4.4 Electrochemical active surface area (ECSA) 39
4.5 Model Electrode Fabrication and Characterization 43
4.5.1 Electrochemical Cell 43
4.5.2 SEM Imaging 45
4.5.3 Model Supports 46
4.5.4 Catalyst Deposition 47

CHAPTER 5 PLATINUM EQCM **49**
5.1 Pt Reduction/Oxidation Explored by EQCM 50
5.2 EQCM Dissolution Study 59
5.3 EQCM Nanoparticle Sintering Study 62
5.4 Summary 67

CHAPTER 6 PT ON GC MODEL ELECTRODE **69**
6.1 Particle size control 69
6.2 Nanoparticle size effects 73
6.3 Oxygen Reduction Reaction 75
6.4 Aging studies 77
6.4.1 Microscopic Aging Study 81
6.5 Summary 85

CHAPTER 7 NANOPARTICLE ARRAYS **86**

7.1 Block Copolymer Theory 87
7.2 Copolymer Template Process 89
7.2.1 Control of Surface Interactions 89
7.2.2 Polymer Template 90
7.2.3 Metal Particle Formation 92
7.3 Pt Nanoparticle Arrays Results 95
7.4 Nanoparticle Arrays on Glassy Carbon 97
7.5 Summary 101
CHAPTER 8 CONCLUSIONS 102
CHAPTER 9 REFERENCES 105

List of Figures

Figure 1.1 - Schematic cross section of a typical PEM fuel cell MEA [6]. 3

Figure 1.2 -The three-phase boundary in a GDE [2] 5

Figure 1.3 - Schematic of (a) fuel cell polarization curve compared to ideal voltage [11] 7

Figure 2.1 - Proposed catalyst deactivation mechanisms in PEMFCs: (a): dissolved Pt species from smaller particles diffuse through ionomer phase and redeposit onto the surfaces of larger particles (Ostwald ripening); (b): Pt nanoparticles migrate on the surface of carbon support and coalesce; (c): Pt nanoparticles detach from the carbon support and/or agglomerate due to carbon corrosion; (d): Soluble Pt species from the cathode are reduced and precipitated out in the ionomer due to chemical reduction by permeated hydrogen molecules from the anode 12

Figure 2.2 - Pt Pourbaix Diagram[38]. The oxidative reaction potentials for a pH of 1 are indicated. 21

Figure 2.3 – Bulk Pt Pourbaix diagram recreated with expanded corrosion region 23

Figure 2.4 - Particle size effect on the equilibrium cell potential and the impact on the Pourbaix diagram (PtO formation) at a 3 nm particle size. 24

Figure 2.5 - Pt Pourbaix diagram for 3nm particles 25

Figure 2.6 - PSDs and TEM micrographs of (a) the pristine Pt/Vulcan powder sample and (b) powders scraped away from the cathode surface of the cycled MEA [46] 26

Figure 4.1 - Cyclic Voltammetry (a) Cyclic potential sweep, (b) Resulting cyclic voltammogram 31

Figure 4.2 - Schematic of a) rotating disk electrode with indicated fluid path b) ring disk electrode design 32

Figure 4.3 – Plot of Koutecky-Levich equation for RDE electrode with slow kinetics 34

Figure 4.4- Experimental RDE setup and schematic 35

Figure 4.5 - SRS Electrochemical Quartz Crystal Microbalance (a) and schematic (b) 38

Figure 4.6 - EQCM setup 39

Figure 4.7 - Cyclic voltammogram of Pt Catalysts with hydrogen desorption region highlighted 40

Figure 4.8 - CO stripping voltammogram on Pt Catalysts 42

Figure 4.9 - Characterization Cycle between SEM ⇔ RDE 46

Figure 4.10 - (a) Wetting film growth and (b) Non-wetting growth 48

Figure 5.1- Cyclic voltammogram of sputtered Pt film with corresponding mass changes at scan rate of 200mV/s. Arrows show associated scan direction for hysteresis 52

Figure 5.2 - Pt charging curve as a function of potential at a scan rate of 200 mV/s in 0.1M $HClO_4$ 55

Figure 5.3 - Anodic mass change as a function of cumulated charge at a scan rate of 200 mV/s 56

Figure 5.4 - Cyclic voltammograms on Pt coated QCM at 50mV/s in 0.1M $HClO_4$ 57

Figure 5.5 - EQCM observed mass loss during CV cycling at 50mV/s (0 - 1.3V_{RHE}) 60

Figure 5.6 - Massogram showing mass loss during potential cycling 60

Figure 5.7 - Potentiostatic mass loss at 1.0V 61

Figure 5.8 - XPS results from sputtered carbon film with peak fitting results 62

Figure 5.9 - Schematic of Pt/C EQCM sample 63

Figure 5.10 - CV of Pt/C QCM 64

Figure 5.11 - SEM of Pt sintering at a loading of 2.1 ug/cm2 after (a,b)initial conditioning and (c,d) after 190 cycles 0 – 1.2V 65

Figure 5.12 - SEM of Pt sintering at a loading of 1.0 ug/cm^2 after (a,b)initial conditioning and (c,d) after 190 cycles 0 – 1.2V 66

Figure 6.1. - SEM images of Pt nanoparticles on a model glassy carbon support with a surface loading of (a) 1.1 μg/cm^2 and (b) 2.1 μg/cm^2. These samples were heated to 800 °C to generate observed particle size distribution with an average size of 2.7 nm in (c) and 4.3 nm in(d). 70

Figure 6.2 - Pt particle size distribution as a function of annealing temperature (a) as deposited, (b) 800°C, (c) 1000°C, (d) 1100°C 71

Figure 6.3 - Custom SEM boat for glassy carbon electrodes (a) SEM boat, GCE and tools (b) mounted in the IN-LENS SEM holder 73

Figure 6.4 - Pt oxide reduction peak shift with cathodic scan at 200 mV/s. Pt nanoparticles on GC of 3.4nm, 4.1nm vs. a bulk polycrystalline Pt electrode. 74

Figure 6.5 - Pt oxide cathodic scan peak shift at 200 mV/s. Pt nanoparticles on GC vs. a bulk polycrystalline Pt electrode 75

Figure 6.6 - ORR RDE results on model catalyst (a) 2.1 μg/cm^2 Pt/glassy carbon and (b) solid polycrystalline Pt. 76

Figure 6.7 - SEM image of Pt/C after ORR cycling. Pt nanoparticles and carbon corrosion are visible 77

Figure 6.8 - 2.1 μg/cm^2 Pt annealed at 800C (a) initial PSD, (b) after conditioning (0 - 1.4V), (c) 500 cycles 0.6 – 1.2V_{RHE} 78

Figure 6.9 - 2.1 μg/cm^2 Pt as deposited (a) initial PSD, (b) after conditioning (0 - 1.4V), (c) 500 cycles 0.6 – 1.2V_{RHE} (d) initial conditioning cathodic peak shift 80

Figure 6.10 - SEM images of the same area during aging process with cycles of 0.6 – 1.2 V_{RHE} at 50mV/s 82

Figure 6.11 - SEM image of Pt nanoparticles on a model glassy carbon support with a surface loading of 2.1 μg/cm2 (top). Close-ups of SEM images reveals particle migration and coalescence (middle and bottom). 83

Figure 6.12 - Surface area loss noticeable in the CV and ESCA with potential cycling of 0.6 – 1.2 V_{RHE} at 50mV/s 84

Figure 7.1 - Diblock copolymer phase diagram[106] 88

Figure 7.2 - SEM images of copolymer template (a) 20nm pores from a Mn = 67.1 kg/mol and (b) 10nm pores from a Mn=31.5 kg/mol P(S-b-MMA). 91

Figure 7.3. - Schematic of the Pt nanoparticle synthesis path using a block copolymer template and a SEM image of the polystyrene template 93

Figure 7.4 - Deposition thickness to particle size relation ship 94

Figure 7.5 – Pt lift-off process (a) secondary electron (SE) image and (b) backscatter electron (BSE) image 94

Figure 7.6 - Particle size control (a-c) SEM images of 9.8, 3.6, 1.2 μg/cm2 pore loadings (d-f) corresponding PSDs 96

Figure 7.7 - μ-wire EDM cutting of glassy carbon electrodes (a) AGIE system and (b) wafer schematic 98

Figure 7.8 - Glassy carbon array (a) after 1.7 nm Pt deposition, (b) after lift-off and (c) after 700°C anneal 99

Figure 7.9 - Pt nanoparticle arrays after initial conditioning, particle movement visible .. 100

Figure 7.10 - Particle agglomeration from detachment/reattachment 100

Chapter 1

Introduction

A catalyst can be defined as a substance which enhances the *rate* of a chemical reaction without being either consumed or generated in the process. Analogous to catalysis, is electrocatalysis, which is the combination of electrochemistry and heterogeneous catalysis materials investigated to promote *electrochemical* reactions. One of the main goals in (*electro)*-catalysis is to a create link between the microscopic level of understanding the atomic and electronic structure of a catalyst and the macroscopic reaction rate of a process, i.e. the activity of the catalyst. For this kind of *fundamental* research, the use of well-defined model surfaces is essential since investigations on three dimensional porous materials is often too complex and difficult to interpret. Only recently, the frequent use of well-defined surfaces has become meaningful to electrocatalysis with the advent of new preparation methods as well as modern analytical tools such as high resolution scanning electron microscopy, atomic force microscopy, cyclic voltammetry, electrochemical quartz crystal microbalance and the rotating disk electrode technique.

Fuel cells are an important application of such fundamental research on electrocatalyst. Although the basic concept of a fuel cell as a device for direct conversion of chemical energy into electric energy was described by Grove [1] well before the invention of either the internal combustion engine or the steam generator, the technological implementation has proved difficult. As a result it was the heat engine rather than the electrochemical engine which was chosen as the main source of motive power, although the latter offers

theoretically a higher efficiency for energy conversion. More recently fuel cells have become technological relevant however, as primary energy resources remain abundant and inexpensive, the use of fuel cells has been limited to specific areas such as the use of fuel cells in the NASA Apollo space program. In the last decade, the rising concern about environmental consequences of the use of fossil fuels and the increasing dependence on oil have led to a resurgence of interest in the fuel cell technology. Now flexible power devices and fuel cell powered vehicles are being reconsidered as industrialized countries seek to decentralize power generation and reduce emissions [2]. Catalysts and supports with reduced precious metal loading, increased activity and durability, and lower costs are the major challenges remaining to fuel cell commercialization. The basic reaction of a fuel cell is the oxidation of hydrogen and the reduction of oxygen to form water. The electrode surfaces in the fuel cell serve as the catalyst where adsorbed molecules from the fuel can react. Consequently, the field of electrocatalysis is directly tied to the development of fuel cells into commercially useful devices. To understand the surface chemistry and deactivation mechanisms, the development of new electrocatalysts should start with the study of a model system [3, 4]. The strength of the binding of reactants to the surface is a fundamental property to catalytic science. Therefore model surfaces are an important research tool to further our knowledge of the relationship between activity and measurable fundamental properties.

These well defined model surfaces, with the addition of nanoparticle structures are applied to the study of electrocatalysts degradation in this research. The addition of nanoparticle structures to the electrode surface addresses the gap in literature between single crystal and powder catalyst studies. The model electrode enables measurements by

surfaces surface science techniques such as high resolution scanning electron microscopy (HRSEM) while the nanoparticle structures provide relevant particle sizes for electrochemical measurements.

1.1 *Proton Exchange Membrane Fuel Cells (PEMFC)*

To understand the factors involved in fuel cell durability, first the materials, components and PEMFC operation must be examined. Fuel cells are electrochemical devices that convert chemical energy as fuels into electrical energy directly with high efficiency and low environmental impact. The proton exchange membrane fuel cells (PEMFCs) are being extensively studied as power sources because of their technological advantages such as high energy efficiency, high energy and power densities, environmental friendliness, low noise, rapid refueling, and fuel flexibility. Though fuel cells could, in principle, process a wide variety of fuels and oxidants, of most interest today are low temperature PEMFCs that use hydrogen as a reductant, and ambient air as the oxidant [5].

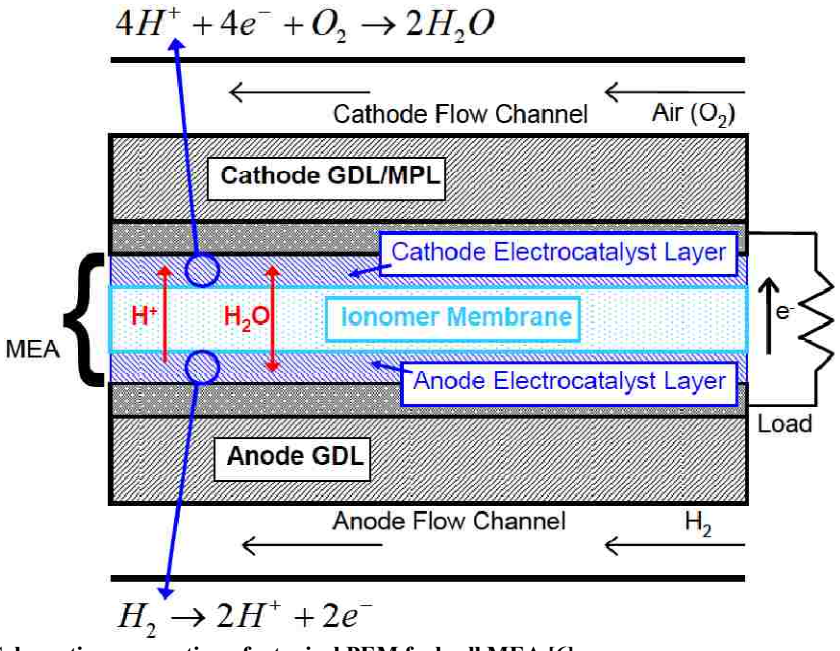

Figure 1.1 - Schematic cross section of a typical PEM fuel cell MEA [6].

The schematic cross section of a single cell of a PEMFC showing individual components is shown in Figure 1.1 [6]. The individual cell consists of a cathode, an anode, and a separating polymer-electrolyte membrane referred to as the ionomer membrane. The ionomer is typically a specific perfluorosulfonic acid (PFSA) material known as Nafion®, a commercially available PFSA membrane offered by Dupont. Each electrode has an electrocatalyst layer and a gas diffusion layer (GDL). The fuel, typically hydrogen, is fed continuously to the anode (negative electrode) and an oxidant (often oxygen from air) is fed continuously to the cathode (positive electrode). The electrochemical reactions take place at the electrodes to produce an electric current through the electrolyte, while driving a complementary electric current that performs work on the load.

Polymer electrolyte membrane fuel cells (also called PEMFC, PEFC or PEM) are able to efficiently generate high power densities, thereby making the technology potentially attractive for mobile and portable applications. Especially the application of PEMFC as a prime energy source for automobiles has captured the imagination of many. PEMFC technology differentiates itself from other fuel cell technologies in that a solid phase polymer membrane is used as the cell separator/electrolyte. Because the cell separator is a polymer film and the cell operates at relatively low temperatures, issues such as sealing, assembly, and handling are less complex than most other fuel cells. The need to handle corrosive acids or bases is eliminated in this system. PEMFCs typically operate at low temperatures (60 to 80 ^{o}C), allowing for potentially faster startup than higher temperature

fuel cells. The PEMFC is seen as the main fuel cell candidate technology for light-duty transportation applications [5].

Each electrode has an electrocatalyst layer, and a gas diffusion layer (GDL). The catalyst layers can be attached to either the membrane or at times to the GDL material (termed the gas diffusion electrode, GDE). Electrodes for PEMFCs have to be porous to gas diffusion to ensure the supply of the reactant gases to the active zones, where the noble metal catalyst is in contact with the ionic and electronic conductor. The fabrication of gas diffusion electrodes, although commercially available, is an intricate process in which all details of the structure are important. The structure of the GDEs is crucial for fuel cell performance and depends strongly on the manufacturing process. The function of the electrodes is actually for more than just catalyzing a reaction which is carried out by the catalyst particles. A good electrode is a three-phase boundary between the gas supply, the catalyst particle and the ionic conductor as shown in Figure 1.2 [2].

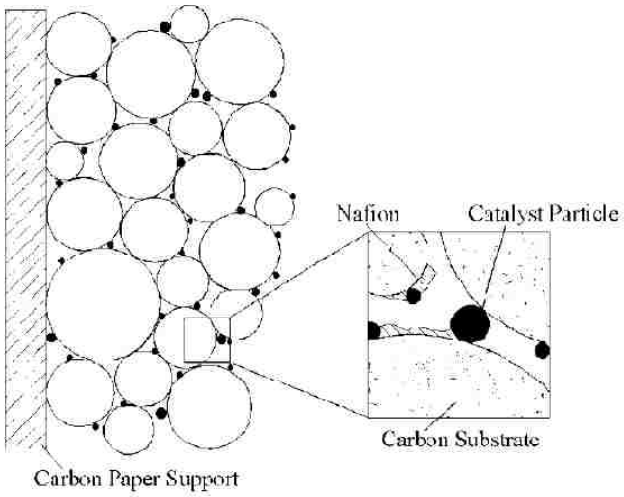

Figure 1.2 -The three-phase boundary in a GDE [2]

The catalyst must be in direct contact with both an electronic and ionic conductor. The electronic conductivity is usually provided by a carbon support.

Protons produced from oxidation of hydrogen in the anode flow to the cathode through the membrane and combine with oxygen to form water in the cathode. The oxygen reduction reaction (ORR) at the cathode is a good example of the importance of the triple junction shown in Figure 1.2. The diffusion of oxygen through the gas diffusion layer, the diffusion of protons through the ionomer and conduction of electrons through the carbon support must all come together at the Pt nanoparticle surface. A compensating charge in the form of electrons flows through the external circuit and provides the useful work done by the fuel cell [7]. These anodic and cathodic reactions as well as the overall cell reaction are shown in equations (1-1), (1-2) and (1-3).

Anode $$H_2 \rightarrow 2H^+ + 2e^- \quad (1\text{-}1)$$

Cathode $$\frac{1}{2}O_2 + 2H^+ + 2e^- \rightarrow H_2O \quad (1\text{-}2)$$

Overall $$H_2 + \frac{1}{2}O_2 \rightarrow H_2O \quad (1\text{-}3)$$

The main fundamental problems of PEMFCs are the lack of practical efficiency due to the high overpotential for the oxygen reduction reaction (ORR), the high amount of noble metal catalysts used and the degradation of the catalyst during operation [8-10]. The cell voltage of a fuel cell is the difference between the two half cell reactions equations (1-1) and (1-2). As both half cell reactions suffer from losses, the cell voltage also decreases with increasing current density. The expected open circuit voltage of 1.23V is not realized as a deviation from this potential occurs, known as over potential. This is depicted in

Figure 1.3 where the losses due to the cell resistance and mass transport are shown. The large initial loss on the cathode plot is due to slow kinetics and is the reason for all the research focus on the cathode catalyst [11].

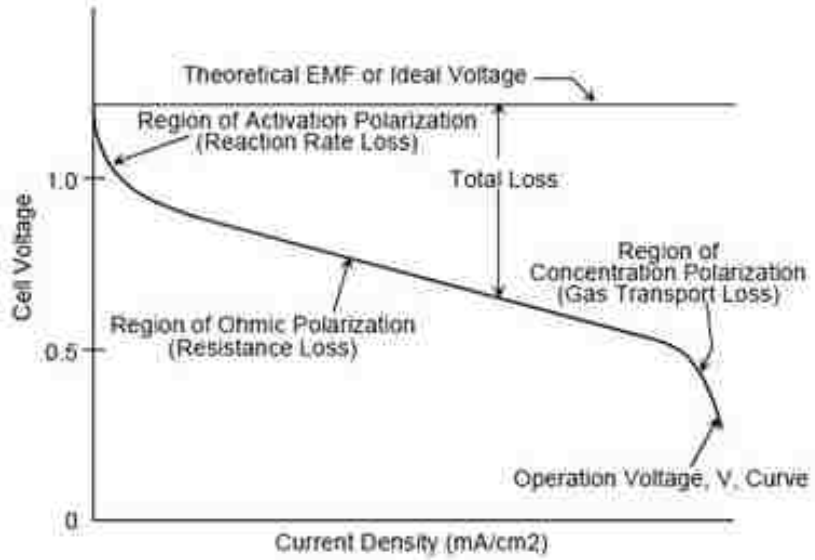

Figure 1.3 - Schematic of (a) fuel cell polarization curve compared to ideal voltage [11]

The most effective catalyst in these systems consists of nanoparticles of Pt or Pt-based alloys on carbon supports. Because of the expense of platinum catalyst, there have been numerous efforts to minimize the use of platinum in the catalyst layer. The platinum particle size has been extensively optimized, and general agreement is that a ~3.5 nm particle size on a suitable carbon support is close to optimal (i.e. the activity per unit mass of platinum is near optimal under these conditions). There have been numerous efforts to substitute other materials for platinum, most of these attempts focused on platinum alloys (usually with transition metals). So far, these efforts have not demonstrated a decisive cost advantage over pure platinum catalysts.

The relatively short life of polymer electrolyte membrane (PEM) fuel cells is a significant barrier to their commercialization in stationary and mobile applications. A longer life span for fuel cell components should be achieved to ensure high reliability, low maintenance costs and to justify fuel cells as economical alternative energy systems. The lifetime target of the department of Energy (DOE) by 2010 requires PEM fuel cells to achieve 5000 h for mobile and 40,000 h for stationary applications. Currently, the lifetime targets can only be met under best laboratory conditions. For example, Mercedes–Benz claims a lifetime of above 2000 h without performance degradation for their current fuel cell stacks operated in test-vehicles all over the world [12].

Automotive fuel cell systems need to be as durable and reliable as current automotive engines. Thus, automotive fuel cell systems will have to last for at least 5,000 h (equivalent to 150,000 driven miles) and be able to function properly over the full range of external ("ambient") temperatures (-40°C to +40 °C). Membranes, which are critical components of the fuel cell stack, must be able to perform over the full range of system operating temperatures with less than 5% performance loss at the end of life without external humidification, which adds cost and complexity to the system. Catalyst lifetime is also important and can be compromised by platinum sintering and dissolution, especially under load cycling and high electrode potentials. Carbon-support corrosion is another challenge at high electrode potentials and can worsen with load cycling and high-temperature operation. Fuel cells for stationary applications will likely require more than 40,000 h of reliable operation. Stationary fuel cells with lifetimes routinely greater than 40,000 h have been demonstrated, but these fuel cells are based upon PAFC (phosphoric acid) and have made limited market penetration to date. PEM fuel cell tests for stationary applications have

lasted up to 20,000 h, but market acceptance likely requires increased reliable operating duration, including over the full range of external temperatures (-35 °C to +40 °C). U.S. DOE lifetime status and targets (with cycling and <5% rated power degradation at the end of fuel cell life) for integrated transportation PEM fuel cell power systems fueled by hydrogen are as follows: a 2005 status of 1,000 h, and a 2010/2015 target of 5,000 h. The lifetime status and targets (with <10% rated power degradation at the end of fuel cell life) for integrated stationary PEM fuel cell power systems fueled by reformate are as follows: a 2003 status of 15,000 h, a 2005 status of 20,000 h, and a 2011 target of 40,000 h [6].

Chapter 2

Durability and Degradation

Typical causes of PEM fuel cell failure are likely low level contamination, corrosion of the plates leading to increased contact resistance, thermal or hydration cycling leading to mechanical stress, catalyst particle ripening, swelling of polymer materials in the active catalyst layer change water removal characteristics, compaction of the gas diffusion layer due to mechanical stresses and surface chemistry changes in gas diffusion layer.

The durability or irreversible degradation of the membrane electrode assembly (MEA), strictly related to the lifetime, is defined as the ability of a MEA to resist permanent change, in performance over time; that is degradation that does not lead to catastrophic failure but simply a decrease in performance that is not recoverable or reversible. Normally lifetime degradation is not a catastrophic failure. Typically, a PEMFC exhibits a gradual decline in power output during operation. Initially, the cumulative effect of this gradual decline is acceptable; that is, the power output of the cell or stack is still high enough to effectively operate the device to which it provides power. But with time, the cumulative effect of this gradual decline can become so large that the cell or stack can no longer deliver the required power. The degradation is then unacceptable.

The causes of the gradual performance decline are not completely understood, especially the degradation mechanisms that occur in the fuel cell's different components and the relative contribution of each component's degradation to the degradation of the entire fuel cell. However, such understanding is required for PEMFC developers to develop new materials that last longer but are not prohibitively expensive [6].

Many mechanisms of MEA degradation have been proposed. These factors include PEM thinning [13], catalyst layer degradation due to platinum sintering [14, 15], or carbon support corrosion [16], and gas diffusion layer (GDL) degradation [17]. Among these, catalyst layer degradation is one of the most critical factors. More and more experimental results have shown severe catalyst degradation in both automotive and stationary applications. Increasing catalyst layer durability is becoming a major challenge and a growing focus of research attention in PEM fuel cell durability studies [6, 12, 18].

2.1 *Catalyst Surface Area Loss Mechanisms*

One of the more significant causes of fuel cell performance degradation is the cathode catalyst deactivation during extended operation. It is generally accepted that there are four mechanisms that are considered relevant to the loss of electrochemically active surface area of Pt in the fuel cell electrodes that contribute to cathode catalyst degradation. The first two mechanisms are forms of catalyst particle sintering. The first is an electrochemical form of Ostwald ripening, where a dissolved Pt species diffuses through the electrolyte from smaller particles and redeposits on the surfaces of larger particles. The second is migration and coalescence, which is when the nanoparticles move on the surface of the carbon support. The second two mechanisms involve a loss of the Pt from the carbon surface either by particle detachment from corrosion of the carbon support or dissolution of the Pt into the electrolyte [7, 18-20].

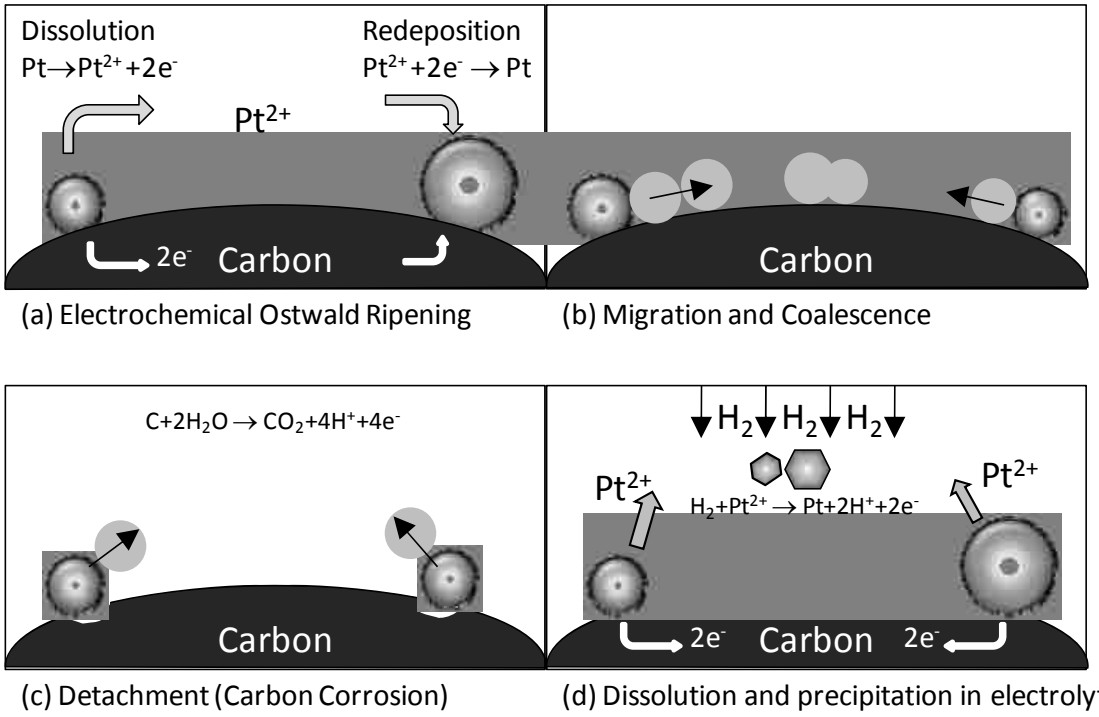

Figure 2.1 - Proposed catalyst deactivation mechanisms in PEMFCs: (a): dissolved Pt species from smaller particles diffuse through ionomer phase and redeposit onto the surfaces of larger particles (Ostwald ripening); (b): Pt nanoparticles migrate on the surface of carbon support and coalesce; (c): Pt nanoparticles detach from the carbon support and/or agglomerate due to carbon corrosion; (d): Soluble Pt species from the cathode are reduced and precipitated out in the ionomer due to chemical reduction by permeated hydrogen molecules from the anode

2.1.1 Ostwald ripening

The electrochemical version of Ostwald ripening based coarsening of individual Pt nanoparticles on carbon involves dissolution of Pt from small particles, diffusion of the soluble Pt species from small to large particles in the ionomer phase or on the carbon surface followed by redeposition of the soluble Pt onto large particles on the nanometer-scale, as shown in Figure 2.1a. This process is analogous to the well known gas phase Ostwald ripening process [21]. This transport of atoms from small particles to large particles and growth of the large particles at the expense of small ones is driven by the

reduction in the surface energy. Assuming the occurrence of particle growth in PEMFC electrodes by such a mechanism, the total number of particles naturally decreases as the particle size increases, and the catalyst surface area decreases leading to a loss of electrocatalytic activity. This mechanism is likely to be responsible for some of the surface area loss in the fuel cell cathode when the cathode is exposed to voltages higher than 0.8 V vs the reversible hydrogen electrode (RHE), either at steady-state or transient potentials, where the solubility of Pt nanoparticles is significant.

Meyers and Darling [22] showed that Pt dissolution in PEM fuel cells is negligible at low and high potentials, but is remarkable at intermediate potentials. In their kinetic model of Pt dissolution in PEMFCs, they explained the effect of potential in the following way [23]. They considered three reactions:

$$Pt \rightarrow Pt^{2+} + 2e^{-} \quad \text{(platinum dissolution)} \tag{2-1}$$

$$Pt + H_2O \rightarrow PtO + 2H^{+} + 2e^{-} \quad \text{(platinum oxide film formation)} \tag{2-2}$$

$$PtO + 2H^{+} \rightarrow Pt^{2+} + H_2O \quad \text{(chemical dissolution of platinum oxide)} \tag{2-3}$$

Their model and experimental data indicated that at lower potentials, such as the conditions of normal H_2/air fuel cell operation, the solubility of platinum in acid is quite low. At high potentials in air, Pt forms an oxide layer effectively insulating the platinum particles from dissolution. At intermediate potentials, however, the uncovered surface is prone to high rates of platinum dissolution.

The rate of of platinum dissolution is slow to approach equilibrium which has a rather serious implication for Pt stability: Pt is stable at low potentials due to the low equilibrium concentration of Pt^{2+} at these potentials, and Pt is fairly stable at higher potentials due to the protective oxide layer. However, transitions between high and low potentials can undermine the stability of the Pt crystallites, as the concentration of Pt^{2+} in solution can increase by orders of magnitude over that which is stable at either low or high potentials. It is worth noting that this window of instability for a PEMFC occurs between the H_2-air open-circuit mixed potential at the cathode (~0.95 V) and the air-air open circuit potential (~1.229 V). Once the Pt^{2+} dissolves into solution, it can be recaptured by the electrode from which it was liberated, but it can also diffuse to other regions of the MEA and permanently lower Pt content within the cathode. Thus, these transitions at start-up and shutdown can have profound implications on electrochemical area and performance of PEMFC cathodes [24].

2.1.2 Migration and coalescence

Pt crystal migration and coalescence, which involves motion of Pt particles and coalescence when two particles collide on the carbon support, as shown in Figure 2.1b. Crystallite migration and coalescence in the absence of electrolyte is observed in gas-phase sintering studies of Pt/C catalysts but is insignificant at low temperatures [25]. Although unique experimental evidence of crystal migration of Pt nanoparticles in low-temperature fuel cells has not been reported, it has been proposed that this process is responsible for surface area loss in the fuel cell cathode when the cell voltages are low, since the solubility of Pt nanoparticles is believed to be negligible at voltages lower than 0.7 V vs. RHE from bulk Pt measurements.

The two primary arguments in support of Pt coarsening via crystal migration are based on the absence of voltage dependence and the shape and growth of the particle size distributions. Prior studies of Pt nanoparticles supported on carbon did not observe a significant potential dependence (0 V to ~0.8 V) of the Pt area loss over time in phosphoric acid (H_3PO_4), from which it was concluded that simple Pt dissolution and redeposition cannot be the dominating mechanism [25]. Gruver et al. [26] have shown that the change in the electrochemical surface area of Pt nanoparticles supported on carbon varies to a small extent with the applied potential up to 0.75 V vs. RHE, and no change in Pt loading is noted in the cathode. The particle migration mechanism has implications for the growth rate and asymptotic shape of the particle size distribution. The mechanism can be described generally by surface migration of adatoms on the Pt crystal surface, 2D motion of Pt crystals on the carbon support, and coalescence when crystals meet [27]. In the crystal migration model, Granqvist and Buhrman have used a simple statistical method, to show that the asymptotic particle size distribution is log-normal with respect to volume (with a distinctive tail at large particle sizes) and Ruckenstein and Pulvermacher [28] have shown that the rate of particle growth is dependent on particle loading on support. These properties have been used to identify when crystal migration is occurring. Blurton et al. have shown an asymptotic Pt particle size distribution of Pt nanoparticles with a tail at large particle sizes in an electrode exposed to air and held at 0.6 V and 163 ºC for 645 h [29]. Based on the shape of this asymptotic distribution, these authors related the surface area loss of Pt nanoparticles in the PA fuel cell environment to the mechanism of crystal migration and coalescence. The correlation between steady-state particle size distribution and the coarsening process has been used by Wilson et al. [30] in understanding the

degradation of Pt nanoparticles supported on Vulcan aged under a constant voltage (0.5 V) or constant current density (1.5 A/cm2) over a few thousands of hours of operation in a hydrogen/oxygen PEM fuel cell. Asymptotic Pt particle size distributions with a tail toward large particle sizes were found in their cathode, a growth mechanism via crystal migration was proposed.

2.1.3 Carbon corrosion

Detachment of Pt nanoparticles from the carbon support and agglomeration of Pt nanoparticles is generally induced by carbon corrosion, as shown in Figure 2.1c. The extent by which this process contributes to the loss of electrochemical activity of fuel cell electrodes is dependent on the cell voltage, the nature of interactions between Pt nanoparticles and the carbon support, the degree of graphitization of carbon support, and potentially other factors, such as the relative humidity. Although corrosion of conventional carbon supports such as Vulcan is considered negligible at cell voltages lower than 0.8 V in low-temperature fuel cells, carbon corrosion and weight loss has been shown to be significant at voltages higher than 1.1 V vs. RHE [7, 31]. It is well known that carbon can thermodynamically corrode above 0.207 V to carbon dioxide and corrosion currents reach significant levels around 1V and above [32]. Carbon support on the hydrogen-fed anode side is generally very stable, except during voltage reversal due to fuel starvation. On the other hand, the cathode is generally operated in a potential window (0.6 – 1.0 V) that is thermodynamically susceptible to carbon corrosion. To make situations worse, start-up and shutdown of fuel cell systems can result in local cathode potential as high as 1.5V [33]. Also, after shutdown, the anode and cathode compartments may be filled with air, setting the electrode potential to around 1.2V. Such high voltages during start-up and shutdown of

a fuel cell dramatically enhance carbon corrosion. Although a large body of corrosion data on platinized carbon support is available under PAFC operating conditions [32], only limited work has been published on corrosion of carbon support under PEM operating conditions [34].

Carbon is thermodynamically unstable at typical operating conditions of the air electrode. The equilibrium potential for carbon oxidation to carbon dioxide is 0.207 V relative to a reversible hydrogen electrode (RHE) at 25°C. PEM fuel cell cathodes generally operate at potentials in the range of 0.5–0.9 V RHE, significantly more anodic than the equilibrium potential for carbon corrosion. The carbon corrosion reaction is quite slow at typical operating temperatures (~70°C), even in the presence of platinum and water. Stable performance after prolonged operation at these potentials suggests that the rates of carbon loss are so low as to be largely negligible over the required lifetimes of fuel cell power plants, provided that the local cathode potential does not exceed about 1 V [22].

$$C + 2H_2O \rightarrow CO_2 + 4H^+ + 4e^- \quad (E^0=0.207 \text{ V vs RHE}) \tag{2-4}$$

The hydrogen and oxygen reactions may proceed in either direction, but the carbon reaction is allowed to proceed only in the anodic direction. The irreversibility of the reaction in equations (2-4) and (2-5), in aqueous systems is generally accepted [32]. Significant oxidation of carbon to CO_2 can be expected to decrease the performance of a PEM fuel cell by the detachment and loss of Pt nanoparticles. Electrochemical oxidation of carbon at room temperature to CO_2 and CO, has been reported to occur at potentials above $0.9V_{RHE}$. There is presently no detailed, widely accepted mechanism in the literature that explains carbon surface oxide generation and conversion into CO_2. One proposed stepwise

mechanism of surface oxide formation and CO_2 evolution is shown here where water is understood to be the source of oxygen in the reaction [23].

$$\vdash C\text{-}H \rightarrow \vdash C\text{-}OH \rightarrow \vdash C\text{-}O \rightarrow \vdash C\text{-}OOH \rightarrow \vdash H + CO_2(g) \quad (2\text{-}5)$$

Stevens and Dahn [35] studied effect of Pt on the carbon oxidation in air at high temperature. They measured the weight loss on heating catalyst samples in air, ranging from 0 to 80 wt% Pt on high surface area BP2000 carbon. The base carbon when heated in air at 195 °C showed no weight loss even after 3000 h. With the Pt/C samples, significant weight loss occurred arising presumably from the catalyzed combustion of carbon with oxygen. This weight loss increased with the temperature over the range of 125 to 195 °C and also increased with Pt loading.

2.1.4 Dissolution

Dissolution and reprecipitation of Pt single crystals in the ionomer membrane from the chemical reduction of dissolved Pt by hydrogen molecules results in the loss of Pt from the carbon support and loss of electrode activity, as shown in Figure 2.1d. Hydrogen molecules can permeate through the proton-conducting membranes in the MEA resulting in chemical reduction of any dissolved Pt resulting in deposition. The location of this Pt deposition in the membrane is dependent on the partial pressure of oxygen in the cathode. The higher the partial pressure of oxygen, the farther from the cathode the Pt deposition occurs. Understanding and reducing Pt dissolution is key to increase Pt catalyst stability in low-temperature fuel cells. In particular, dissolution underlies the 3D Ostwald ripening mechanism, which can enable the growth of large Pt nanoparticles at the expense of small ones and loss of Pt from the carbon support via precipitation of Pt in the ionomer and

membrane. Therefore, it is of great importance to understand processes and parameters that influence Pt dissolution so that they can be controlled. Pt is electrochemically stable in acids at low potentials relative to RHE potential but Pt dissolves in acidic solutions at high potentials. [7].

The presence of Pt particles in the matrix of phosphoric acid fuel cells and Pt loss from the cathode has been reported, which has provided direct evidence for Pt dissolution from supported Pt nanoparticles in the cathode and reduction of the dissolved Pt species with permeated hydrogen gas molecules in the membrane. Yasuda et al. [36, 37] have detected the appearance of numerous Pt single crystals on the order of 10 – 100 nm in the membrane after potential holds at high voltages such as 0.8 V and 1.0 V in air and nitrogen in PEM fuel cells. In addition, the amount of Pt found in the matrix and thus the amount of Pt dissolution was shown to increase with increasing cathode potentials.

2.2 *Nernst Equation and the Pt Pourbaix Diagram*

In electrochemistry, the Nernst equation can be utilized to determine the equilibrium potential for reduction-oxidation reactions. For a simple reversible redox reaction in solution like equation (2-6) the representative Nernst equation is (2-7).

$$Ox + ne^- \leftrightarrow Red \tag{2-6}$$

$$E = E^o - \frac{RT}{nF}\log\frac{[Red]}{[Ox]} \tag{2-7}$$

The concept of *solution potential* introduced by Nernst, shows the importance of determining the pH of a solution as well as the potential in the study of chemical and electrochemical oxidation-reduction phenomena. Pourbaix introduced the method of plotting the thermodynamic equilibrium conditions of all the reactions that can occur for a metal in contact with an aqueous solution on a potential-pH diagram, now known as Pourbaix diagrams. These diagrams show the conditions under which the occurrence of a given oxidation or reduction reaction is possible.

The dissolution of the Pt nanoparticles is fundamental to a few of the sintering mechanisms outlined in chapter 2, so it follows that a thorough understanding of the Pourbaix diagram for the Pt system is important. The focus will be on the region around our test conditions of pH=1 and the potential in the water window of E=0 to 1.23 V versus the standard hydrogen electrode (SHE). Take a look at the Pt Pourbaix diagram in Figure 2.2 and pH=1 (0.1M $HClO_4$), we see Pt will form $Pt(OH)_2$ above a potential of 0.92 V and will transform to PtO_2 above a potential of 0.99 V. It is believed that this first potential

represents the potential for dissolution and that PtO_2 passivates the surface preventing dissolution.

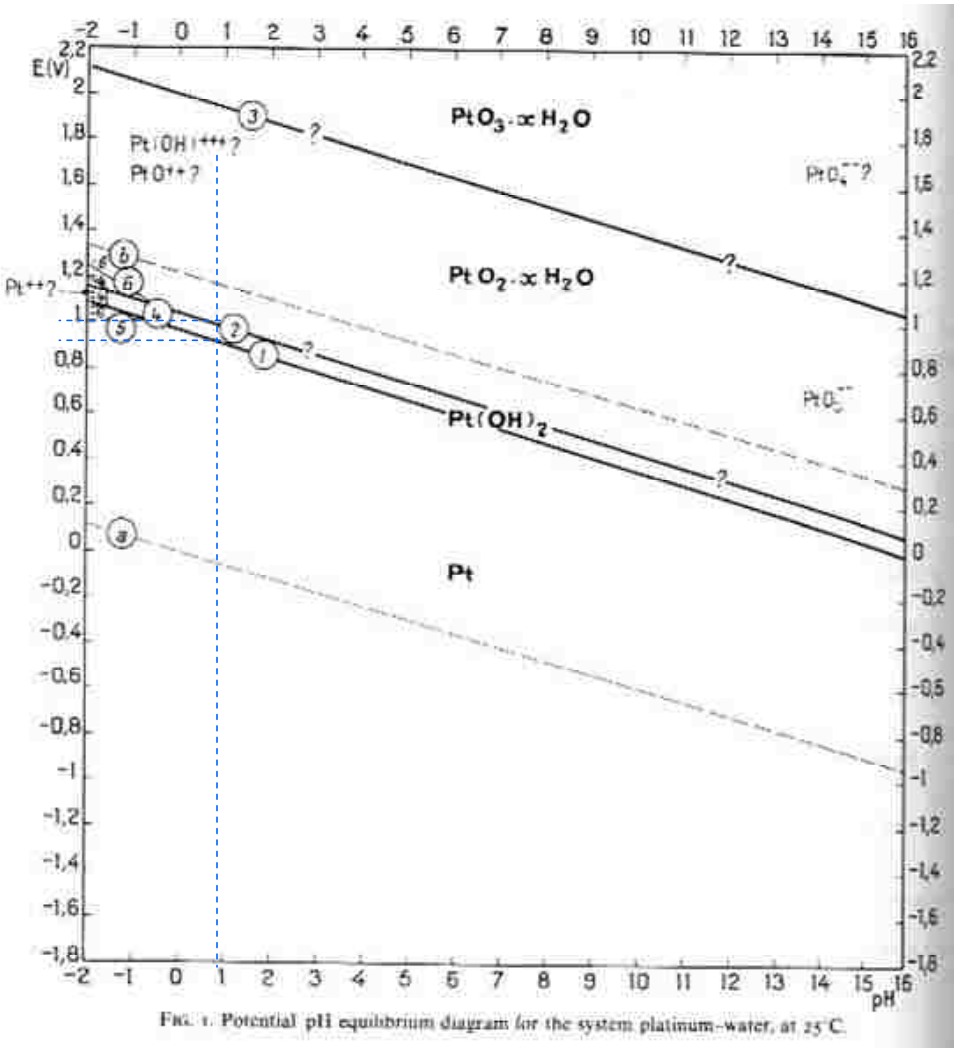

FIG. 1. Potential pH equilibrium diagram for the system platinum-water, at 25°C.

Figure 2.2 - Pt Pourbaix Diagram[38]. The oxidative reaction potentials for a pH of 1 are indicated.

The corrosion region of interest isn't very well shown on this published diagram in Figure 2.2, so the Pourbaix diagram is recreated here from the following thermodynamic equations:

$$Pt + 2H_2O \leftrightarrow Pt(OH)_2 + 2H^+ + 2e^- \quad (2\text{-}8)$$
$$E = 0.980 - 0.059\,pH$$

$$Pt(OH)_2 \leftrightarrow PtO_2 + 2H^+ + 2e^- \quad (2\text{-}9)$$
$$E = 1.045 - 0.059\,pH$$

$$PtO_2 + H_2O \leftrightarrow PtO_3 + 2H^+ + 2e^- \quad (2\text{-}10)$$
$$E = 2.000 - 0.059\,pH$$

$$Pt^{++} + 2H_2O \leftrightarrow Pt(OH)_2 + 2H^+ \quad (2\text{-}11)$$
$$\log([Pt^{++}]) = -7.06 - 2\,pH$$

$$Pt \leftrightarrow Pt^{++} + 2e- \quad (2\text{-}12)$$
$$E = 1.188 + 0.0295\log([Pt^{++}])$$

$$Pt^{++} + 2H_2O \leftrightarrow PtO_2 + 4H^+ + 2e^- \quad (2\text{-}13)$$
$$E = 0.837 - 0.1182\,pH - 0.0295\log([Pt^{++}])$$

The Pt Pourbaix diagram for the region of interest with an expanded corrosion section indicated by the contour lines at different Pt^{++} concentrations has been plotted in Figure 2.3. This figure clearly shows the region of dissolution. While the equilibrium concentration of 10^{-10} M appears to be very small it can represent a significant fraction of the available Pt on these lowly loaded electrode surfaces. For example, complete dissolution of a Pt film on a 5mm electrode at a loading of 1.07 μg/cm^2 into 100 ml of electrolyte would only generate a Pt^{++} molar concentration of 10^{-8} M. So an equilibrium concentration of 10^{-10} M represents dissolution of 1% of the Pt on these small RDE electrodes.

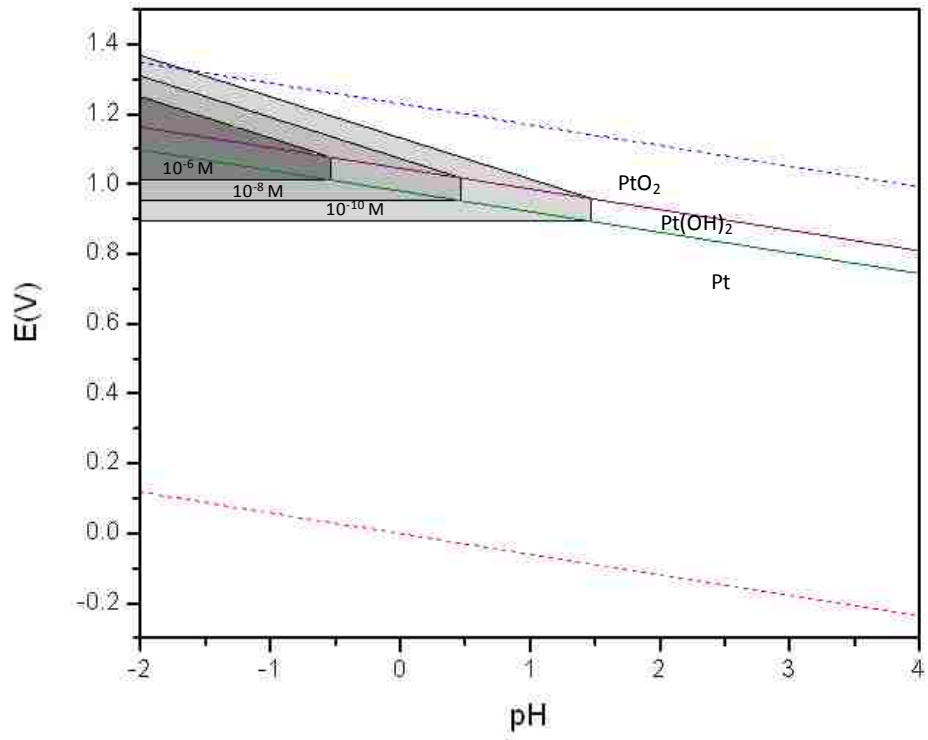

Figure 2.3 – Bulk Pt Pourbaix diagram recreated with expanded corrosion region

2.2.1 Application of the Nernst Equation to Nanoparticles

Electrochemical processes at the nanometer scale may result in Pt dissolution at lower potentials than those predicted based on the Nernst equation alone. To apply this effect to the Nernst equation we take advantage of the relationship between the cell potential E and the chemical potential available from redox reactions ($E = \mu c / e$). So E is related to the Gibbs free energy change ΔG only by a constant: $\Delta G = -nFE$, where n is the number of electrons transferred.

An electrochemical equivalent of the Gibbs-Thomson (GT) equation can provide the effect of interfacial energy on the solubility in terms of particle radius, the same way this effect is applied to chemical potential and vapor pressure. This curvature effect on E_{Pt} can

be calculated by adding the Gibbs-Thomson equation to the Nernst equation. A basic thermodynamic analysis would indicate that the stability decreases with particle size [39].

$$E' = E_o - \frac{RT}{nF}\ln K_{rxn} - \frac{2\gamma\Omega}{rnF} \tag{2-14}$$

Here *E'* is now the equilibrium potential corrected for the effect of local surface curvature, Ω is the molar volume and r is the radius of curvature. If we use a room temperature surface energy (γ) value of 1500 dyne/cm in Eq. (2-14), the variation from equilibrium potential can be calculated as a function of radius of curvature. As can be seen in Figure 2.4, this results in a reduction of ~100 mV in the equilibrium potential at a typical Pt particle diameter of 3 nm [40]. The common crystal surfaces have different surface energies so both the surface energy for Pt(110) of 1553 dyne/cm and Pt(111) of 977 dyne/cm are shown to provide an effective range [41].

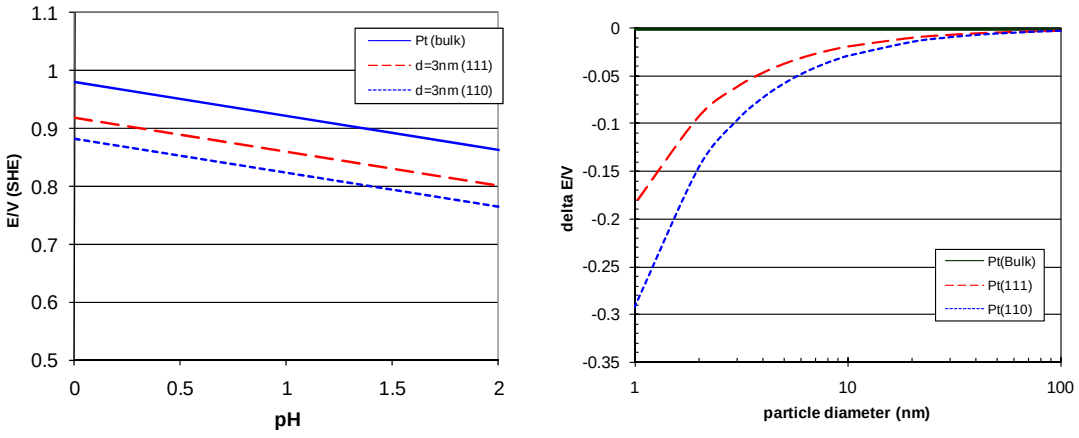

Figure 2.4 - Particle size effect on the equilibrium cell potential and the impact on the Pourbaix diagram (PtO formation) at a 3 nm particle size.

Figure 2.5 shows the new Pt Pourbaix diagram with the Gibbs-Thomson effect calculated for a 3nm particle. An average surface energy of 1000 dyne/cm was used for this calculation as the Pt particles are predicted to be mostly (111) terminated.

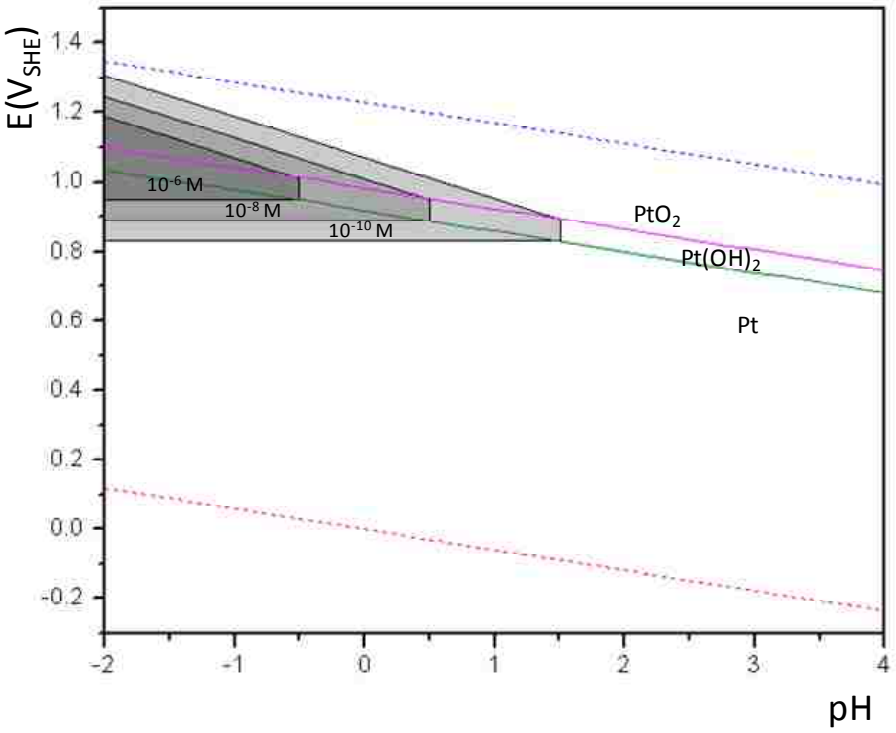

Figure 2.5 - Pt Pourbaix diagram for 3nm particles

2.3 *Previous Sintering Studies*

It is well known in the PEMFC literature that Pt particle growth does indeed occur [30, 42-44]. The reasons for this growth may be due to a number of possible mechanisms, as such, this is an active area of research. Most research conducted on this subject use membrane electrode assemblies (MEA) for aging and measurements of the growth in platinum particle size requires destruction of the MEA to use the most common techniques of x-ray diffraction (XRD) or transmission electron microscopy [45, 46].

An example of a MEA aging study can be seen in Figure 2.6. The narrow particle size distribution found on the pristine Pt/Vulcan is contrasted against the broader particle size distribution for the cycled MEA cathode catalyst. The change in the mean platinum particle diameter also changed significantly from 2.8 to 5.9 nm.

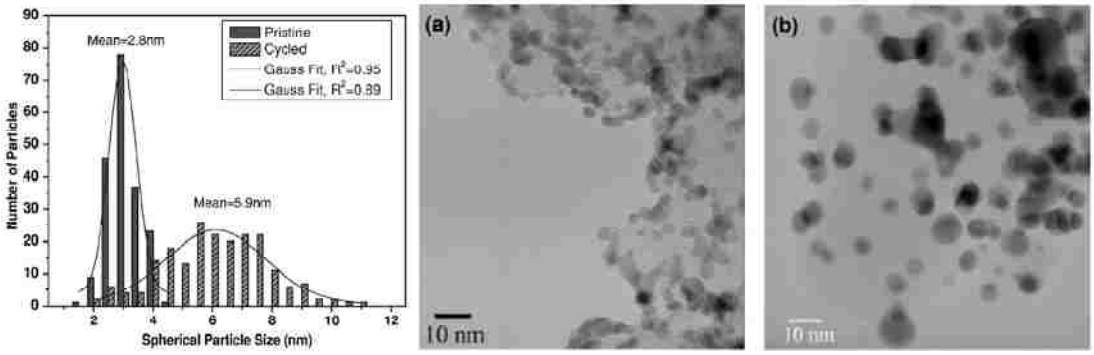

Figure 2.6 - PSDs and TEM micrographs of (a) the pristine Pt/Vulcan powder sample and (b) powders scraped away from the cathode surface of the cycled MEA [46]

Ferreira et al. [46] also examined the catalyst powder particle size distributions through the thickness of the catalyst. The particles closer to the ionomer sintered significantly more, with very broad distributions, when compared to those closest to the gas diffusion layer. They suggested this was related to the availability of hydrogen through the dissolution reprecipitation mechanism. The result was an overall particle size distribution tailing toward large particle sizes. It is generally accepted that a distribution with a tail toward small particle sizes represents nanometer-scale Ostwald ripening, whereas the distribution with a tail toward larger sizes is caused by platinum diffusion/precipitation mechanism or migration and coalescence. The overall particle size distributions can easily be misinterpreted when multiple platinum area loss mechanisms are occurring. Typical X-ray diffraction analysis of particle size growth include platinum particles both on the

carbon support and in the ionomer phase, which is not electrochemically active and would be misleading when determining the active platinum surface area for the aged cathode.

Chapter 3

Research Objectives

Understanding the role of the nanoparticle size and structure on the catalytic activity and degradation is needed to optimize the fuel cell durability and reduce the noble metal loading. Most approaches to study this role utilize commercial catalysts which are incorporated into MEAs. The result is a complex system wherein it is difficult to deconvolute the effect of the nanoparticle on electrocatalytic activity [47].

The focus of this research is the development and study of model surfaces to provide insights into the electrocatalyst deactivation mechanisms. These model surfaces are thin non-wetting layers of Pt on planar supports of glassy carbon. The planar supports enable electrochemical activity measurements and surface analysis such as electron microscopy imaging on the same surface. The imaging of the catalyst surface is performed at intervals during the aging process. High resolution scanning electron microscopy (HRSEM) enables the imaging of particle sizes down to 1 nm, on the same surface used in electrochemical rotating disk electrode (RDE) experiments. This resolution was previously only available with Transmission Electron Microscopy (TEM), but is now possible with modern high resolution scanning electron microscopes (SEM).

Markovic and Ross in 2002 [48], mentioned the need of better model systems for real, i.e. supported, electrocatalyst. They went on to describe the need for regular arrays of metal particles fabricated by lithographic methods, as these particles would have all the same size, composition and shape. At that time the lithographic methods were limited to relatively large particles not useful for studies of catalytic nanoparticles. We propose to

address this need with a significant improvement on these model electrode structures by the development of a nanoparticle array of controlled particle size and inter-particle spacing. This will be accomplished by using block copolymer templates. This technique has been demonstrated in the semiconductor industry on large wafers. This templating technique needs to be adapted to the formation of ordered arrays of catalyst nanoparticles on the surface of small carbon RDE electrodes.

Chapter 4

Experimental Methodology

The experimental details are covered in this chapter. The first part of each section deals with the theoretical background of the applied technique. The focus is on the main analytical tools used in this research, such as cyclic voltammetry and the rotating (ring) disk electrode (R(R)DE) technique. In the second part of the chapter the experimental setup, the electrochemical cells and the sample preparation is described. The experimental procedures applied in this work are introduced and also in this part are details concerning electrolyte preparation, cleaning of the electrochemical cells, and the chemicals used.

4.1 *Cyclic Voltammetry*

Cyclic voltammetry (CV) has become an important and widely used electroanalytical technique in many areas of chemistry. With limited effort, a survey of the potentials at which electrochemical processes occur can be rapidly attained. For this reason cyclic voltammetry is the technique of choice when investigating a new electrochemical system. It is rarely used for quantitative determinations, but it is widely used for the study of redox processes, understanding reaction intermediates and for obtaining stability of reaction products [49]. The technique is based on varying the applied potential on the working electrode periodically between an upper and a lower limit at a constant scan rate while monitoring the current. Repetition of the potential waveform allows the system to come to a steady state. Cyclic voltammetry is applied using a three-electrode configuration. The variable potential is applied to the working electrode (we) and current flows between the working and counter electrode (ce). The changes in the potential are measured with respect

to a reference electrode (re), which receives almost no current, so current only flows between the working and counter electrodes.

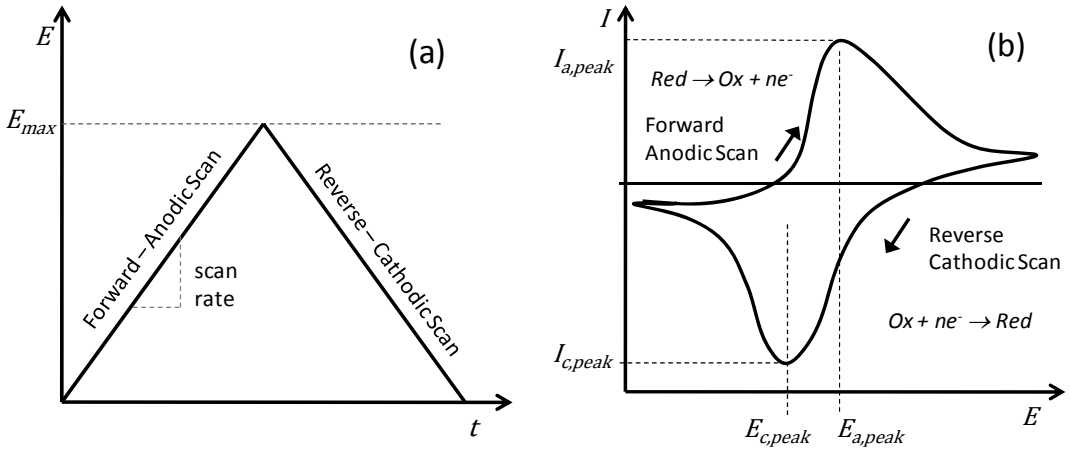

Figure 4.1 - Cyclic Voltammetry (a) Cyclic potential sweep, (b) Resulting cyclic voltammogram

The response obtained from a CV can be very simple, as shown in Figure 4.1 for a reversible redox system. The anodic peak is associated with the oxidative electrochemical reaction, while the cathodic peak is associated with the reductive electrochemical reaction. The value of the current is a direct measure of the reaction rate, while the potential peak positions give the thermodynamics and reaction overpotential.

4.2 *Rotating Disk Electrode*

Kinetic studies of electrochemical reactions require a well defined mass transport. The *rotating disk electrode* (RDE) is a widely used method to study electrochemical measurements under well defined mass-transport conditions. The spinning disk of the RDE drags the fluid at its surface and due to centrifugal force flings the solution outward from the center in a radial direction. This forced convection replenishes the electrolyte at the electrode surface by a flow normal to the surface and brings the reactants dissolved in the

electrolyte to the electrode surface. The mass flow to the electrode surface can easily be controlled by the varying the rotation rate. The diffusion coefficients and kinetic parameters of the electrocatalytic reaction can be calculated from the current-potential relationship at different rotation rates. The RDE is one of the few convective electrode systems for which the hydrodynamic equations have been rigorously solved. Schematics of the rotating disk electrode and *rotating ring disk electrode* (RRDE) are shown in Figure 4.2. The R(R)DE construction details and relevant equations will be briefly discussed.

Figure 4.2 - Schematic of a) rotating disk electrode with indicated fluid path b) ring disk electrode design

The RDE is constructed from a disk electrode material, such as platinum or glassy carbon, imbedded in a rod of insulating material typically made of Teflon. The electrode is attached to a rotary motor, where the rotation leads to very well defined solution flow

pattern. The rotating disk surface acts like a pump, pulling the electrolyte upward and then flinging it outward as shown in the schematic of figure Figure 4.2a. The theoretical treatment of this rotation induced flow was described by Levich, where he described the mass transport of the electrolyte up to the near surface as convective and then diffusion takes over through a small diffusion layer. The diffusion layer thickness of the RDE, δ_{RDE}, is given by [50]:

$$\delta_{RDE} = 1.61 D^{1/3} \omega^{-1/2} \nu^{1/6} \tag{4-1}$$

where D, ω and ν are the diffusion coefficient of the reactant in the electrolyte, the rotation rate of the electrode in rads/s and the kinematic viscosity of the electrolyte respectively. Note that for the RDE the diffusion layer thickness is not time dependent, but only depends inversely on the square root of the rotation rate. Applying Fick´s law the current measured at the disk electrode can be expressed in terms of the concentration of the reactants in the bulk of the electrolyte c_o and at the electrode surface c_s by:

$$I = nFA\frac{D}{\delta}(c_o - c_s) \tag{4-2}$$

where n is the number of electrons transferred in the reaction, F is the Faraday constant and A is the geometric surface area of the electrode. If the reaction rate at the electrode surface is faster than the diffusion of the reactant to the surface then the surface concentration of the reactant is essentially zero and the current is called diffusion limited. The diffusion limited current density I_{dl} can then be calculated by:

$$I_{dl} = nFA\frac{D}{\delta}c_o \tag{4-3}$$

Combining equations (4-1) and (4-3) yields the Levich-equation for the diffusion limited current density on a RDE $I_{d,\,RDE}$:

$$I_{dl} = 0.62nFAD^{2/3}\nu^{-1/6}c_o\omega^{1/2} = B\omega^{1/2} \tag{4-4}$$

where B is called the Levich constant. If the alternate regime is considered where there are no mass transfer effects the measured current would be under kinetic limitation I_K . Combining this with the Levich diffusion limited current I_{dl} results in the *Koutecky-Levich equation* shown equation (4-5), which is graphically depicted in Figure 4.3:

$$\frac{1}{I} = \frac{1}{I_{dl}} + \frac{1}{I_K} = \frac{1}{I_K} + \frac{1}{0.62nFAD^{2/3}\nu^{-1/6}c_o\omega^{1/2}} \tag{4-5}$$

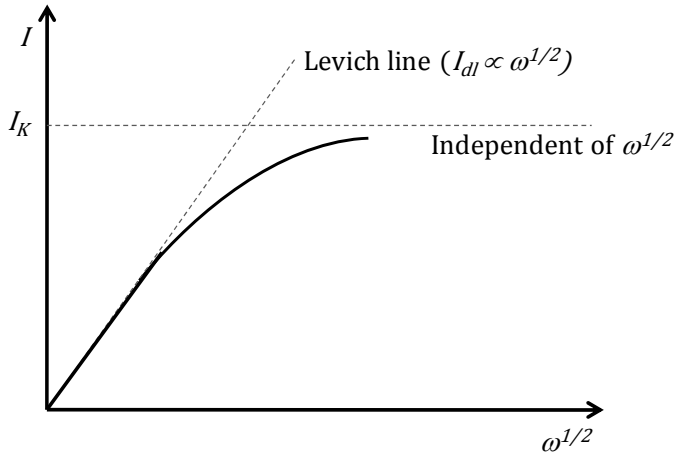

Figure 4.3 – Plot of Koutecky-Levich equation for RDE electrode with slow kinetics

The benefits of the RDE are a controlled time independent mass flow of the reactant to the electrode; a fixed diffusion layer thickness; and the mass flow equations for reactant transport to the surface have been solved and can be conveniently regulated by varying the rotation rate.

A photograph and schematic of the experimental configuration used for the RDE studies in this research are shown in Figure 4.4. The double wall glass electrochemical cell was purchased from Pine Instruments. We used a double frit Ag/AgCl reference electrode or an electrolyte bridge to prevent chloride contamination. A Pt wire or graphite rod was used as the counter electrode. The potentiostat used for these experiments was a Princeton Applied Research VersaSTAT3.

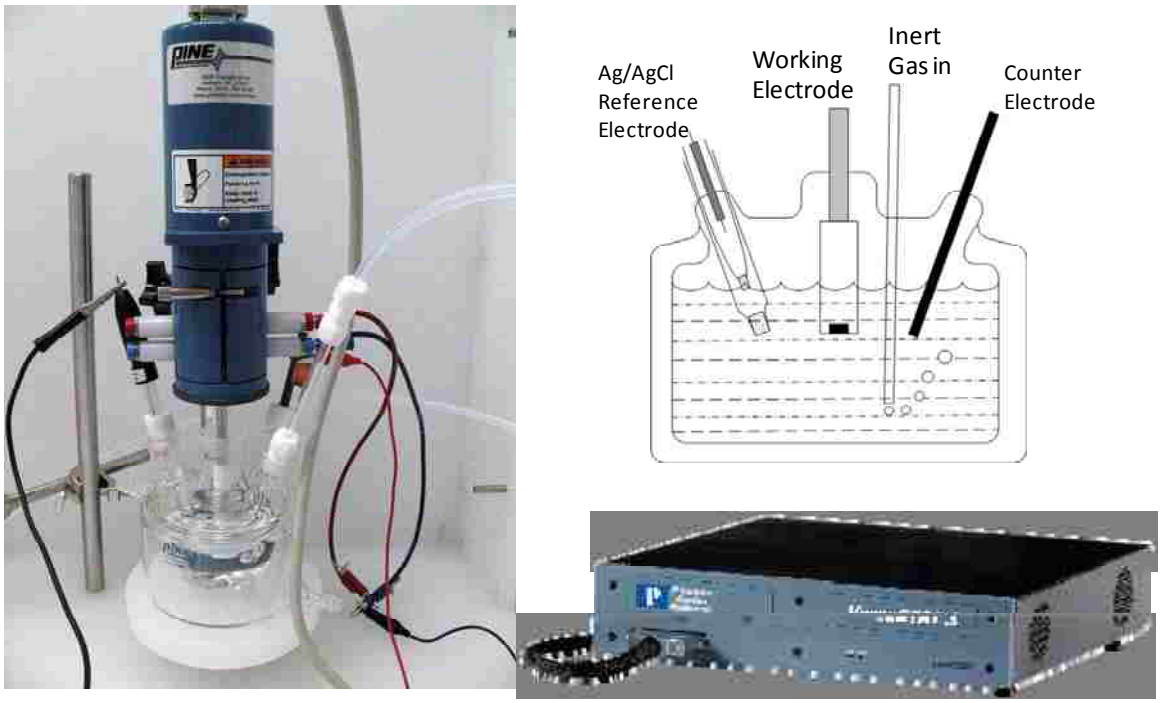

Figure 4.4- Experimental RDE setup and schematic

4.3 *EQCM*

In many electrochemical experiments, mass change occurs as material is deposited or lost from the "working" electrode. To monitor those changes simultaneously with the electrochemical response, the *electrochemical quartz crystal microbalance* (EQCM) is the

standard means of doing so. As a gravimetric probe, the EQCM has been used in many types of electrochemical studies, including: underpotential deposition of metals, corrosion, oxide formation, dissolution studies [51-55].

The EQCM is an extremely sensitive sensor capable of measuring mass changes in the range of ng/cm^2. Sauerbrey was the first to recognize the potential usefulness of the *Quartz Crystal Microbalance* (QCM) technology and demonstrate the extremely sensitive nature of these piezoelectric devices towards mass changes at the surface of QCM electrodes [56]. The results of his work are embodied in the Sauerbrey equation (4-6), which relates the mass change per unit area at the crystal surface to the observed change in oscillation frequency of the crystal:

$$\Delta f = \frac{-2\Delta m f_o^2}{A\sqrt{\rho_q \mu_q}} = -C_f \Delta m \tag{4-6}$$

Where Δf is the observed frequency change in Hz, Δm = the change in mass per unit area in g/cm^2 and C_f is the sensitivity factor for the crystal (56.6 Hz μg^{-1} cm^2 for a 5 MHz AT-cut quartz crystal at room temperature). The crystal sensitivity factor C_f captures all the quartz properties such as the harmonic number n, the resonant frequency f_o, the quartz density ρ_q (2.648 g/cm^3) and the shear modulus μ_q (2.947 x 10^{11} g/cm s^2).

The Sauerbrey equation relies on a linear sensitivity factor, C_f, which is a fundamental property of the QCM crystal. In theory, since only the change in frequency is need to measure the progress of an experiment, the QCM mass sensor does not require calibration. However, the Sauerbrey equation does require that the deposits on the surface are uniform and rigid to yield accurate results.

The change in the crystal frequency is related to the change in mass of attached surface species by the Sauerbrey equation. Only a small modification to the equation is required for operation in liquid mediums. When the QCM comes in contact with a solution, there is a decrease in frequency that is dependent upon the viscosity and the density of the solution. This problem was first treated by Glassford [57], and later by Kanazawa and Gordon [58]. Kanazawa's treatment of the influence of the solution properties on the crystal permits the prediction of the change in resonance frequency which accompanies immersion of the crystal into a viscous medium:

$$\Delta f = -f_o^{3/2}\left(\eta_l \rho_l / \pi \rho_q \mu_q\right)^{1/2} \tag{4-7}$$

Where ρ_L is the density of the liquid in contact with the electrode and η_L is the viscosity of the liquid. This equation represents the observed change in frequency when the sensor is immersed in a liquid, typically around -700 Hz. Again, only the change in frequency is required to monitor the progress of an experiment. So the Sauerbrey equation (4-6) still applies for continuous measurements in the liquid environment.

The EQCM system that was used in these experiments is the SRS QCM200 shown in Figure 4.5 [59]. The working electrode connection from the potentiostat is connected to the top of the QCM oscillator, which is a direct connection to the quartz crystal front surface. The rest of the cell is the typical three electrode configuration. The frequency output from the QCM is converted to a +/- 10V analog signal and is input to the potentiostat through an auxiliary connection for synchronization with the rest of the potentiostat data. The quartz crystals are received with gold electrodes on the surfaces. For our experiments, the surface was first coated with a thin film of either Pt or carbon followed by a very thin layer of Pt.

Using this configuration, experiments were conducted to determine mass loss from Pt dissolution and the mass gain from the oxidative processes as a function of potential.

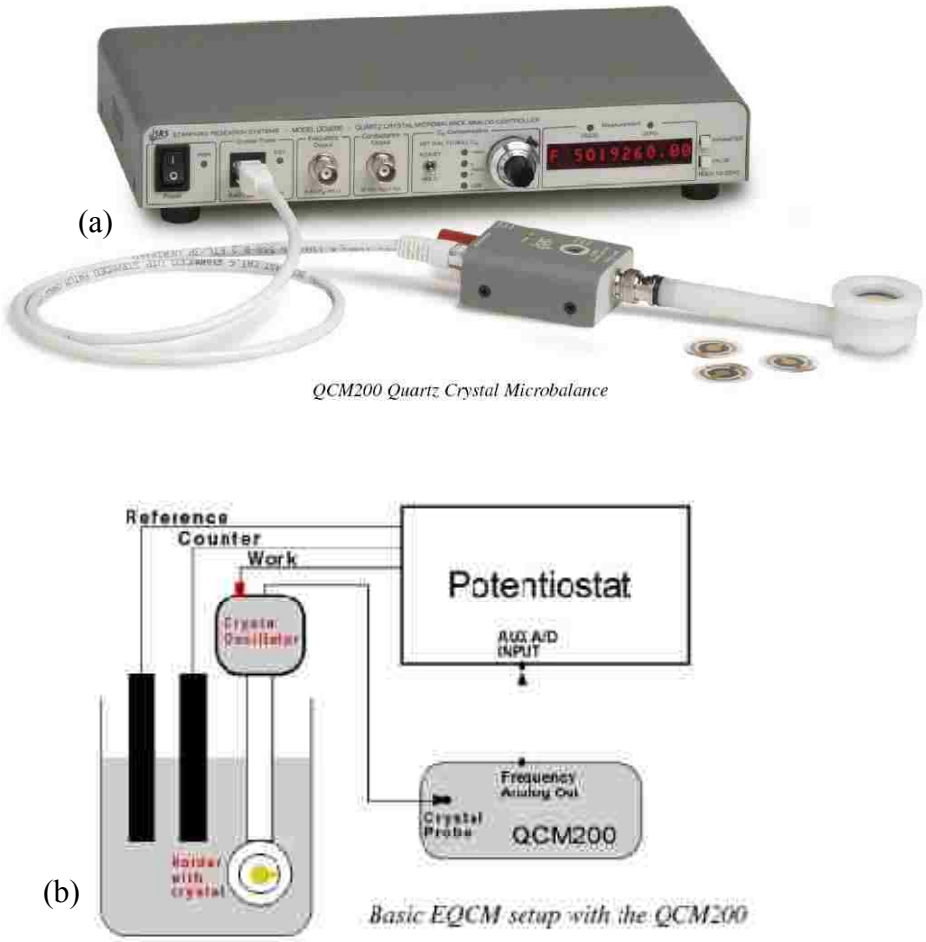

Figure 4.5 - SRS Electrochemical Quartz Crystal Microbalance (a) and schematic (b)

A photograph and schematic of the experimental configuration used for the EQCM studies in this research is shown in Figure 4.6. The double wall glass electrochemical cell was purchased from Adams & Chittenden Scientific Glass. The large Teflon lid on this cell was cut to fit the EQCM handle, a double frit Ag/AgCl reference electrode and a glass

tube for the inert gas. A Pt wire counter electrode was placed in the attached side tube which is connected to the cell via a porous ceramic frit. The potentiostat used for these experiments was a Princeton Applied Research VersaSTAT3.

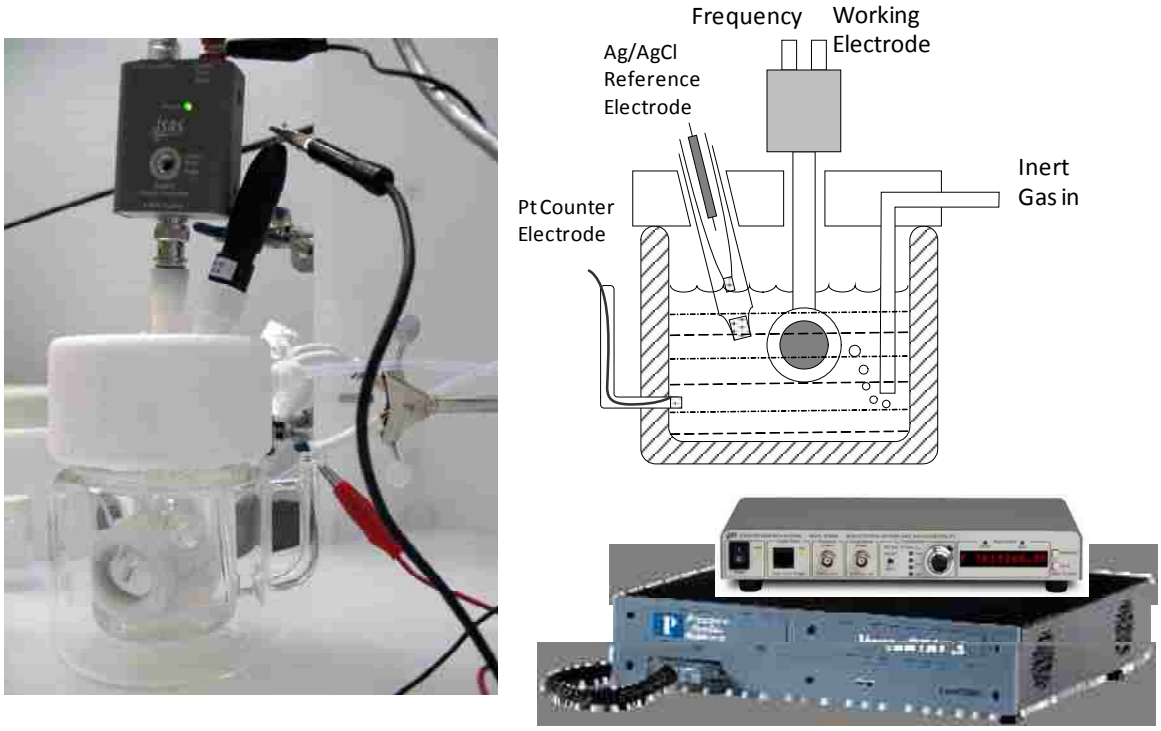

Figure 4.6 - EQCM setup

4.4 *Electrochemical active surface area (ECSA)*

The electrochemical surface area (ECSA) of the fuel cell catalysts can be determined by cyclic voltammetry techniques. The procedure involves cycling the electrode over a voltage range where the charge transfer reactions are adsorption limited at the active surface sites. The number of active sites can be obtained by measuring the total charge for adsorption/desorption of a monolayer.

A typical reaction used when characterizing Pt electrocatalyst is the hydrogen adsorption/desorption (HAD) reaction:

$$Pt\text{-}H_{ads} \leftrightarrow Pt + H^{+} + e^{-} \tag{4-8}$$

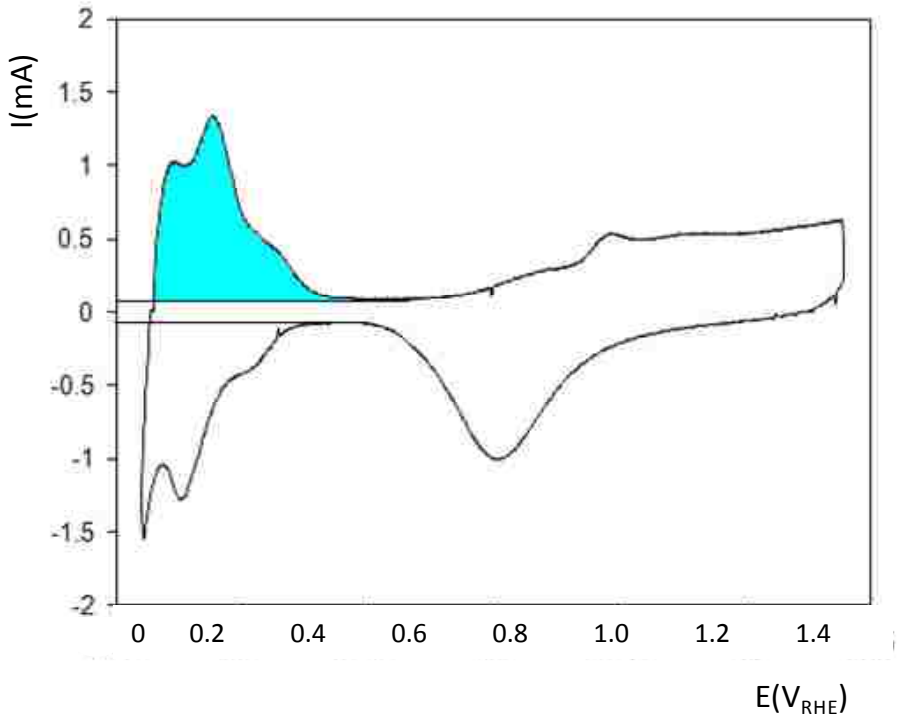

Figure 4.7 - Cyclic voltammogram of Pt Catalysts with hydrogen desorption region highlighted

The cyclic voltammogram in Figure 4.7 of a Pt catalyst in a perchloric acid solution exhibits three characteristic potential regions. The hydrogen underpotential deposition/desorption region (H_{upd}, $0 < E < 0.4$ V_{RHE}) which is followed by the "double-layer" potential region ($0.4 < E < 0.6$ V_{RHE}) and then by the Pt oxidation/reduction region ($0.6 < E < 1.2$ V_{RHE}). The double-layer region represents capacitive charging of the bare platinum metal in the acid solution. No chemical reactions are occurring in this double

layer region, so it can be used to remove the effect of capacitive charging from the reaction regions. The coulombic charge associated with the hydrogen desorption is shown in Figure 4.7 with the capacitive charging removed. The hydrogen oxidation reaction, equation (4-8), is a one electron process so each electron transferred during this reaction represents one platinum atom. This assumes the hydrogen is linearly bonded to only surface atoms. Using an average surface density of 1.3 x 10^{15} atoms/cm^2, the charge required to oxidize a monolayer of protons on Pt is calculated to be 210 μC/cm^2. The ECSA from hydrogen desorption can now be calculated as:

$$ECSA(cm^2) = \frac{q}{Coulombs/cm^2} = \int_{RHE=0}^{RHE=0.4} (I - I_{dl})dt \Big/ 210\mu C/cm^2 \tag{4-9}$$

The other most common method for measuring the electrochemical surface area is oxidative stripping of adsorbed carbon monoxide, known as CO stripping voltammetry.

$$Pt\text{-}CO_{ads} + H_2O \leftrightarrow Pt + CO_2 + 2H^+ + 2e^- \tag{4-10}$$

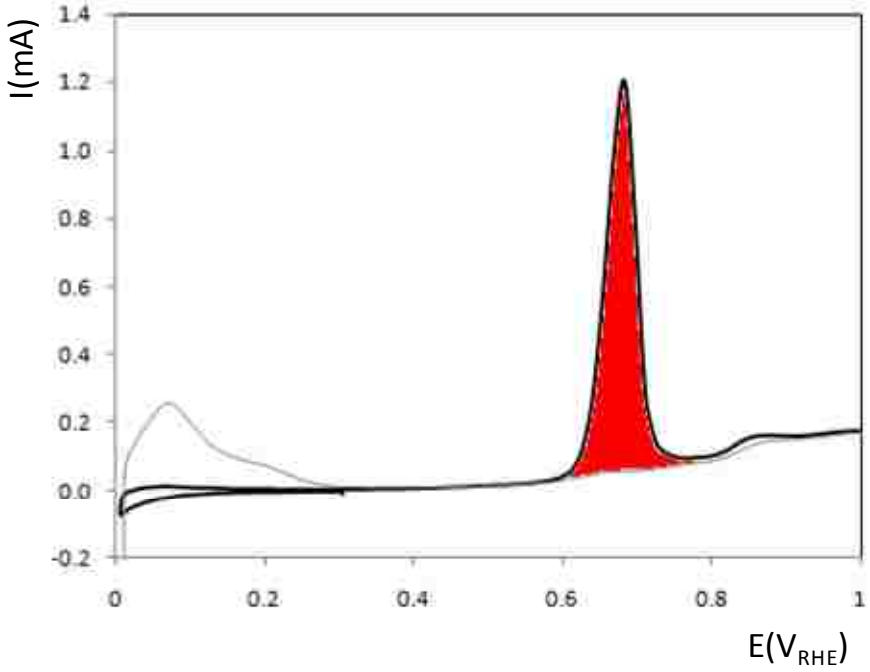

Figure 4.8 - CO stripping voltammogram on Pt Catalysts

This method is conducted by holding the potential fixed in a region where the metal is known to be bare (i.e. no oxide) or hydrogen terminated. CO is bubbled into the electrolyte for a brief period of time, during which time it strongly adsorbs to the Pt surface, even displacing any adsorbed hydrogen if present. Any excess CO in solution is purged with an inert gas before beginning the stripping voltammetry scan.

Figure 4.8 shows a potential hold at 0.3 V_{RHE} followed by a 10 mV/s scan down to 0 V_{RHE} and then the oxidative scan to 1.2 V_{RHE}. Between 0.6 and 0.8 V_{RHE} the CO oxidation takes place. Another voltammetry scan is completed immediately following the stripping scan to be used for background removal. The carbon monoxide oxidation reaction, equation (4-10), is a two electron process so every two electrons transferred during this reaction represents one platinum atom. Again using an average surface density of 1.3 x

10^{15} atoms/cm^2, the charge required to oxidize a monolayer of CO on Pt is calculated to be 420 μC/cm^2. The ECSA from CO stripping voltammetry can now be calculated as:

$$ECSA(cm^2) = \frac{q}{Coulombs / cm^2} = \int_{RHE=0.5}^{RHE=0.9} (I - I_{bkg})dt \Big/ 420\,\mu C / cm^2 \tag{4-11}$$

4.5 *Model Electrode Fabrication and Characterization*

The experimental setup, the electrochemical cells and the sample preparation is described in the following section. The experimental procedures applied in this work are introduced and also in this section are details concerning electrolyte preparation, electrode preparation, cleaning of the electrochemical cells and the chemicals used.

4.5.1 Electrochemical Cell

A typical three electrode electrochemical cell was used to investigate electrode reactions in this research. The cell consisted of the working electrode, which is the location of the catalyst being studied, a counter electrode, which was a 0.020" diameter Pt wire or a 0.25" diameter graphite rod and a reference electrode. The electrolyte was 0.1M perchloric acid in all of these experiments. The material of the cell was glass, selected to minimize reaction with the sample. It is desired for the reference electrode to be as close as possible to the working electrode. However, to avoid contamination, it was necessary to place the reference electrode in a separate compartment or use a reference electrode with a double junction. In this case, the end of the bridge or double junction was placed as close as possible to the working electrode to avoid resistive offsets in the voltage. At the low

currents measured during these experiments it was determined that IR compensation was not required. The unique requirements for each of the voltammetric techniques are described under the individual techniques.

The reference electrode provides a reversible half-reaction with Nernstian behavior, it must be constant over time, and be easy to assemble and maintain. The two reference electrodes used in this study were the saturated calomel electrode (SCE), with the potential determined by the reaction $Hg_2Cl_{2(s)} + 2e^- = 2Hg_{(l)} + 2Cl^-$ and the silver/silver chloride electrode (Ag/AgCl), with potential determined by the reaction $AgCl_{(s)} + e^- = Ag_{(s)} + Cl^-$. The potential of a KCl saturated Ag/AgCl electrode is approximately -0.2V relative to the reversible hydrogen electrode (RHE). As these studies involve platinum as the catalyst, this potential could be verified during experimentation by the onset of hydrogen evolution. All of the potentials reported have been adjusted for comparison to the reversible hydrogen electrode.

Perchloric acid solutions were prepared from concentrated Baker Ultrex Perchloric Acid (67-71%) and HPLC grade water. The 0.1M solution was made by adding 14.7g of the concentrated perchloric acid to a 1L bottle of HPLC water. New glassware was initially cleaned by trichloroethylene vapor, followed by an acetone rinse and then an isopropyl alcohol rinse. Subsequently the glassware was rinsed with concentrated sulfuric acid and then boiled in 18 mega-ohm de-ionized water. After boiling for one half hour the glassware was removed and then rinsed with ultrapure water will still hot. Prior to each experiment, the electrolyte was de-aerated by purging with research grade argon (0.999995 purity). The oxygen reduction reaction (ORR) measurements were carried out in saturated

electrolyte using research grade oxygen. The RDE measurements were performed under a continuous gas flux. The CO stripping measurements were carried out with a short exposure to UHP grade CO.

4.5.2 SEM Imaging

This study of model catalysts structures directly on glassy carbon electrodes is enabled by modern SEM technology. New Scanning Electron Microscopes with low kV, short working distance, field emission (FE) and biased In-Lens detectors result in high resolution, high contrast imaging with very little charging. In this study the catalyst structures were imaged on model supports by high resolution scanning electron microscopy (SEM) using a Hitachi 5200 In-Lens FE SEM. This SEM uses a transmission electron microscopy (TEM) style holder to place the sample into the lens of the microscope, referred to as an in-lens microscope. Pt particles sizes down to 1 nm in diameter can be imaged with this system. A limitation of an In-Lens system is the samples are limited to 5mm in size. The Pine Research Instrumentation© ChangeDisk RDE tips are 5mm in diameter and 4mm in height and were selected for this study.

The catalytic activity of the deposited/sintered Pt particles was measured using rotating disk electrode (RDE) techniques. Cycling between activity measurements and SEM imaging enabled the observation of the catalyst degradation process.

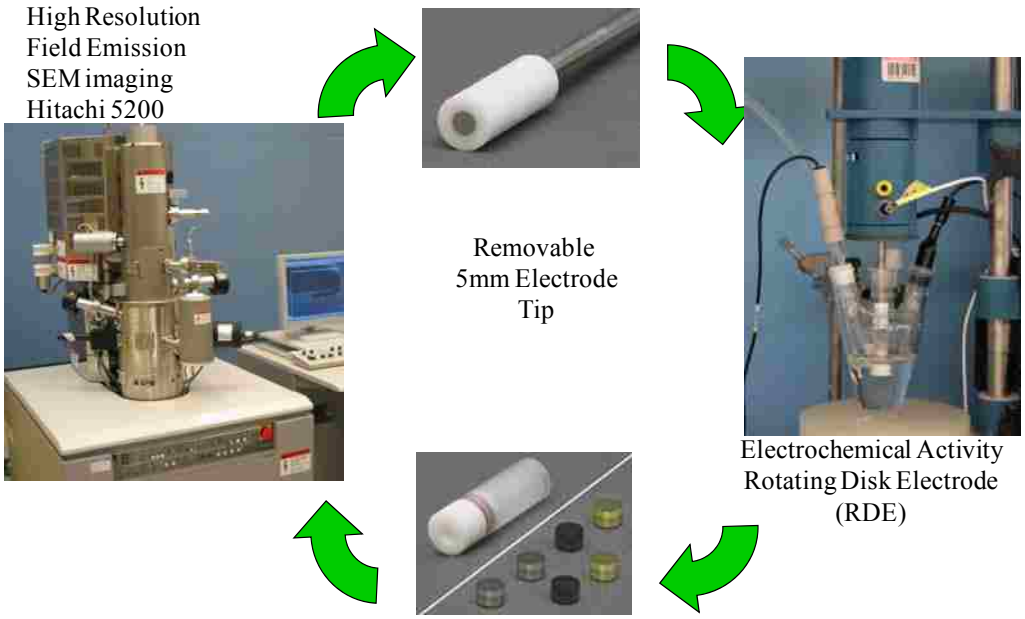

Figure 4.9 - Characterization Cycle between SEM ⇔ RDE

4.5.3 Model Supports

The model supports used in this study were removable 5 mm diameter glassy carbon electrodes purchased from Pine Instruments. These electrodes were prepared by grinding with water on a flat surface using a 600 grit paper, followed by polishing with 5µm alumina solution on a nylon pad and a finish polish with 0.05 µm alumina on a rayon microcloth. The electrode surface is rinsed clean with DI water between each polishing operation. The glassy carbon electrodes are inserted into a Teflon holder, provided in the pine polishing kit, to keep the surface flat during the polishing operation. After polishing the electrodes are cleaned by ultrasonics in de-ionized water.

4.5.4 Catalyst Deposition

To add catalytic metal to these electrodes, high purity platinum material (99.999%) was deposited directly onto the glassy carbon electrode surface using electron beam evaporation. This is a physical vapor deposition (PVD) technique, where 10KV electrons heat the metal until its vapor pressure is high enough to be used for deposition. In a vacuum this vapor travels by line of sight until it collides with a cold surface and condenses. The system pressure during evaporation was 5 x 10^{-7} torr or lower. The platinum film thickness was controlled by a quartz crystal microbalance (QCM), while the rate was maintained at 0.3 Å/s. The QCM as configured on this system is capable of controlling the film thickness to 0.1 Angstroms.

It is important to know how the loading of these model catalysts compares to that of commercial catalysts. Converting typical loading weight percents into an areal density or equivalent film thickness is the best way to make this comparison. Table 4.1 shows the calculated equivalent film loading for a typical 40 wt% Pt catalysts for comparison to these model electrode structures.

Table 4.1: Equivalent Catalyst Loading

Catalysts	***Catalyst Mass / Support Area***	***Equivalent Thickness***
40 wt% Pt on 250 m^2/g XC-72	2.6 mg / m^2 of support	1.2 Å or 0.5 ML
Pt Thin Film on Planar Support	10.7 mg / m^2 of support	5 Å or 2.2 ML
"	21.4 mg / m^2 of support	10 Å or 4.3 ML

Platinum on carbon is non-wetting so a continuous film is not formed during deposition at very low loadings. The growth of this type of film is referred to as Volmer-Weber growth.

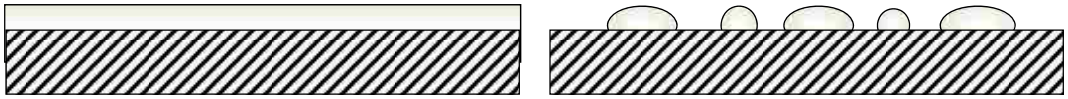

(a) Layer by Layer growth (b) Volmer-Weber growth

Figure 4.10 - (a) Wetting film growth and (b) Non-wetting growth

Effective film thicknesses of 0.5 and 1.0 nm were used in this study. For the remainder of this discussion, a mass loading description of the deposited film will be used instead of an effective film thickness. Platinum has a density of 21.4 g/cm^3, so a film with an effective thickness of 0.5 nm, would have a specific loading of 10.7 mg^{Pt}/m^2. Comparing this to a Vulcan XC-72 catalyst, which has an average surface area of 250 m^2/g and using a typical catalyst loading of 40 wt% Pt, the specific loading would be 2.6 mg^{Pt}/m^2. So the model planar supports used in this study are more highly loaded than the commercial catalyst. This is primarily due to the low planar surface area of the electrode; this higher loading is required to provide enough platinum surface area for electrochemical testing.

Chapter 5

Platinum EQCM

Cathode electrocatalysts in fuel cells are commonly covered with a thin layer of oxide that may have a profound influence over the chemistry, stability and kinetics of the oxygen reduction reaction. Studies concerning the formation and reduction of the anodic oxide film on platinum in aqueous solution have been carried out using electrochemical method such as cyclic voltammetry(CV) and chrono-amperometry in order to evaluate the oxide growth mechanisms (kinetics and thermodynamics). Here we study the platinum oxide formation and reduction and its affect on Pt dissolution using an Electrochemical Quartz Crystal Microbalance (EQCM).

The high mass resolution and in situ capabilities of the EQCM make it useful for observing degradation processes. In combination with additional techniques such as CV, one can distinguish between performance loss caused by particle agglomeration and growth, and degradation related to loss of platinum metal from the catalyst by dissolution. In EQCM experiments, one face of the quartz resonator, which is used as the working electrode is immersed in the electrolyte and electrochemically controlled during a frequency measurement. This allows simultaneous collection of both mass change and electrochemical data. Mass change per unit area, Δm, is calculated from the change in resonant frequency, Δf, using the Sauerbrey equation, $\Delta f = -C_f \Delta m$. The sensitivity factor, C_f, for the crystals used in this study is $56.6\ Hz \cdot cm^2 / \mu g$.

The electrosorption properties of hydrogen and oxygen on Pt electrodes in aqueous media have been widely documented in the electrochemistry literature [60-62]. The EQCM

data are presented as plots of Δm vs. E, known as massograms [63-65], where Δm is the change of the mass at the electrode surface. For changes in mass associated with charge transfer at the electrode surface (faradaic processes), Δm is directly proportional to the current density and hence the massogram is analogous to the voltammogram. In addition, given that observation of a mass flux in the massogram without a corresponding current density in the voltammogram is evidence of a nonfaradaic mass change (i.e. a mass change without an associated charge transfer) on the electrode surface, it is possible to distinguish between faradaic and nonfaradaic processes by comparing a massogram with its corresponding voltammogram [63].

This study is about the oxidation, dissolution and sintering behavior of Pt catalyst in 0.1M of $HClO_4$ solution. The dissolution of Pt in acid solution under potential cycling and potential step has been investigated using EQCM and SEM analysis in order to understand the dissolution mechanism of the electrocatalyst of polymer electrolyte fuel cells.

5.1 *Pt Reduction/Oxidation Explored by EQCM*

These QCM experiments were carried out simultaneously with the voltammetry measurements on Pt coated QCMs. The platinum coating was created by dc magnetron sputter deposition using a 0.99999 purity platinum target. The entire front electrode surface of the 1" diameter, 5 MHz AT-cut quartz was coated with a 10 nm thick chromium adhesion layer followed by a 200 nm Pt layer. All the measurements were made at 293K in a glass electrochemical cell with 0.1M $HClO_4$ solutions purged with ultra high purity argon. The electrochemical setup consisted of the Pt coated EQCM as the working

electrode, a Pt wire as the counter electrode and a KCl saturated Ag/AgCl (SSE) reference electrode. The reference electrode was separated from the main cell by either a salt bridge or a double junction to avoid chloride contamination. Before each measurement the QCM crystal surface was rinsed with ethanol and then distilled water. Immediately prior to use it was cleaned by 2 minutes in a 100 watt oxygen plasma. All potential values shown here have been converted to reference the Reversible Hydrogen Electrode (RHE) potential. The mass per unit area obtained from the Sauerbrey equation is calculated using the geometrically active electrode area of the quartz crystal. This geometrically active area was determined to be 2.85 cm^2 for these Pt coated QCM crystals. This value of mass per unit area was further adjusted by the ratio of the geometric area to the electrochemical active surface area (ECSA) measured using the hydrogen desorption area of the voltammogram. By this method the massogram and voltammogram are referencing the same surface area, the ECSA. The ECSA was typically around 4.1 cm^2 giving a roughness factor of 1.44.

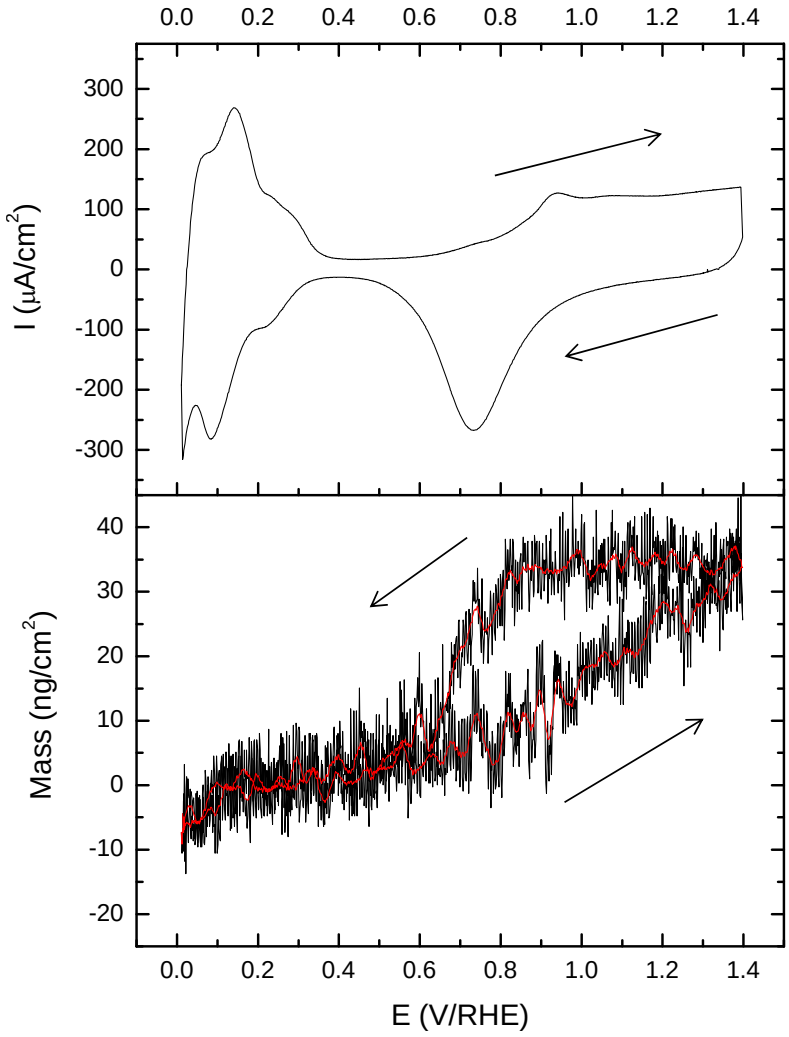

Figure 5.1- Cyclic voltammogram of sputtered Pt film with corresponding mass changes at scan rate of 200mV/s. Arrows show associated scan direction for hysteresis.

To understand the data in Figure 5.1, we must look at the mechanisms of surface oxidation of Pt. As we scan the potential in the anodic direction (increasing potential), the initial peaks ($0 - 0.4V_{RHE}$) in current are associated with the removal of surface hydrogen as shown in equation (5-1). The more weakly bound hydrogen, most likely from the Pt(111) surfaces comes off first followed by the more strongly bound hydrogen on the Pt(100) surfaces [66]. Even though hydrogen is being removed from the surface the

EQCM shows a weight gain. This weight gain is associated with presence of physisorbed water [67]. After the hydrogen has been removed from the Pt surface we reach the double-layer region where the only current is that of capacitive charging of the bare metal surface. This capacitive charging current is always present even when a Faradic reaction is taking place. For this reason all measurements of charge reported here have had this *double-layer* charging current subtracted. Starting at about $0.6V_{RHE}$ the current begins to rise from oxidation of the platinum surface. Early modeling of the initial stages of surface oxide formation at Pt proposed that two distinguishable and successive stages were involved [68-70]. First the deposition of hydroxyls on the surface according to equation (5-2), followed by conversion to platinum oxide according to equation (5-3). The overall reaction is shown in equation (5-4). The EQCM shows an almost steady rise in mass during this oxidation phase.

$$PtH \rightarrow Pt + H^+ + e^- \quad \textbf{(5-1)}$$

$$Pt + H_2O \rightarrow Pt(OH) + H^+ + e^- \quad \textbf{(5-2)}$$

$$Pt(OH) \rightarrow PtO + H^+ + e^- \quad \textbf{(5-3)}$$

$$Pt + H_2O \rightarrow PtO + 2H^+ + 2e^- \quad \textbf{(5-4)}$$

Reversing the scan direction and going in the cathodic direction, we see almost no change in the mass until the PtO reduction peak is reached. This is the reverse of equation (5-4). At this point there is a rapid change in mass associated with the current peak as oxygen is removed from the platinum surface. Once again the potential passes through the double-layer region where the charging current for the cathodic scan can be determined.

As the potential drops below $0.4V_{RHE}$ we see the current associated with the underpotential deposition of hydrogen. The drop in mass in this region is from the displacement of physisorbed water from the Pt surface.

The basis for charging-curve evaluation of surface coverage by electro-chemisorbed species is simply the application of Faraday's lays on a microscopic scale [71]. The charge q transferred for deposition or desorption of an electroactive species such as H or OH is $q=\int i \cdot dt$. On a Pt surface, there are ~ 1.3 x 10^{15} atoms/cm^2, which corresponds to 210 μC/cm^2 for a one electron process. The charging curve for the striping of hydrogen and the deposition of OH and O species on a Pt/QCM are shown in Figure 5.2. The charging current associated with the double-layer capacitance has been removed from this plot. Starting an anodic scan from a potential of 0.0 volts (RHE), the charge increases from the removal of adsorbed hydrogen according to reaction shown in equation (5-1). The charge per unit area is calculated from the current, scan rate and surface area measured from the hydrogen underpotential deposition/desorption. This is a single electron process, so has a surface monolayer limit of 210 μC/cm^2 for Pt. After the double layer region, where no apparent reaction takes place, the charge begins to increase starting at about 0.6V as the growth of a Pt oxide layer begins. At about 0.9V the charging curve associated with platinum oxidation is a straight line. This is in agreement with results shown by Conway [72], where the oxide growth continued in a straight line fashion even into the formation of a multilayer oxide film at higher potentials. In this work all oxide films were < 1 ML, which is 420 μC/cm^2 for this two electron process on Pt as shown in equation (5-4).

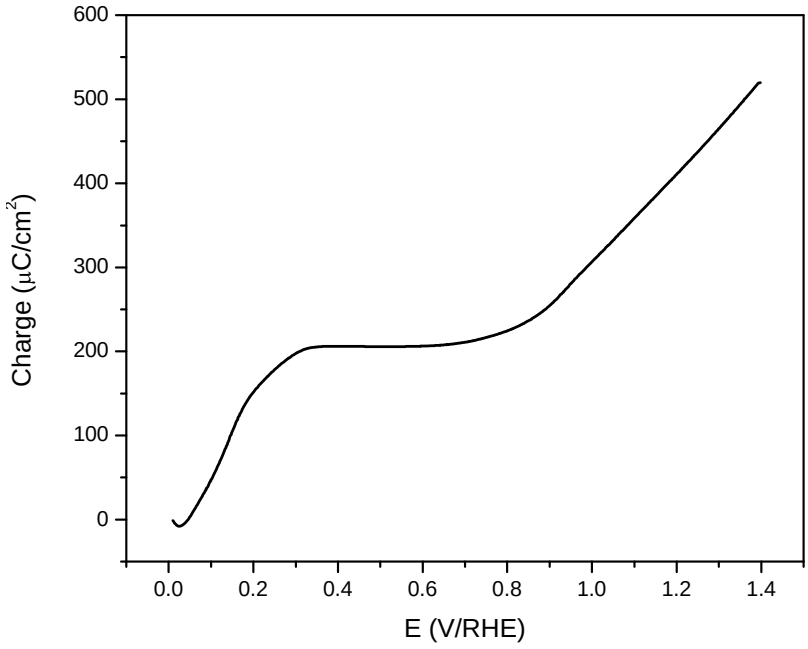

Figure 5.2 - Pt charging curve as a function of potential at a scan rate of 200 mV/s in 0.1M $HClO_4$

Dividing the charge transfer from Figure 5.2, into the QCM mass change from Figure 5.1 and then multiplying by Faraday's constant, we can determine the mass of the species associated with these electrochemical reactions. This is shown in Figure 5.3 where the slopes of four distinct regions are identified. The slopes are expressed in grams per mole of charge. For one electron processes this would be equivalent to the molecular weight of the of the electroactive species.

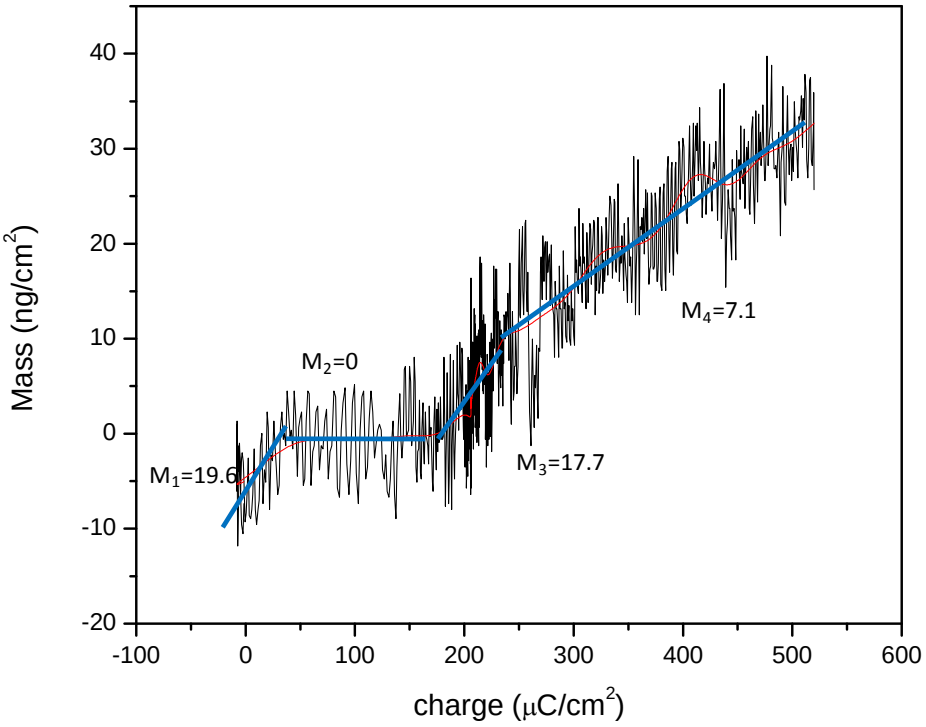

Figure 5.3 - Anodic mass change as a function of cumulated charge at a scan rate of 200 mV/s

The first region identified on this anodic scan mass versus charge plot is associated with the stripping of adsorbed hydrogen. The reaction associated with this region from equation (5-1), should show a mass loss of slope M= 1.0 g/mol. The observed slope of M_1=19.6 g/mol is in reasonable agreement of the information reported about the non-Faradaic adsorption of water with a mass of 18 g/mol at the surface. However this is only observed during the first 50 μC/cm^2 of charge. The second region is relatively flat, M_2= 0, for the remainder of the hydrogen stripping up until 210 μC/cm^2. This matches the expected mass loss for stripping hydrogen. After the double layer region, 210 μC/cm^2, the onset of surface oxidation begins. The initial oxidation has a higher slope with M_3=17.7 g/mol, than the later straight line oxide growth. This first 50 μC/cm^2 of charge is predicted to be associated with the deposition of a hydroxyl layer as shown in equation (5-2). As a one electron process this would represent fractional monolayer, ~1/4 ML of OH in

agreement with the density functional theory (DFT) calculations by Norskov's group [73]. They estimated that the hydroxyl layer was more stable than an oxygen layer up to 1/4 - 1/3 ML. The final region is the oxide growth region and as a two electron process should give a slope of 8 g/mol, which is in good agreement with the measured value of M_4=7.1 g/mol.

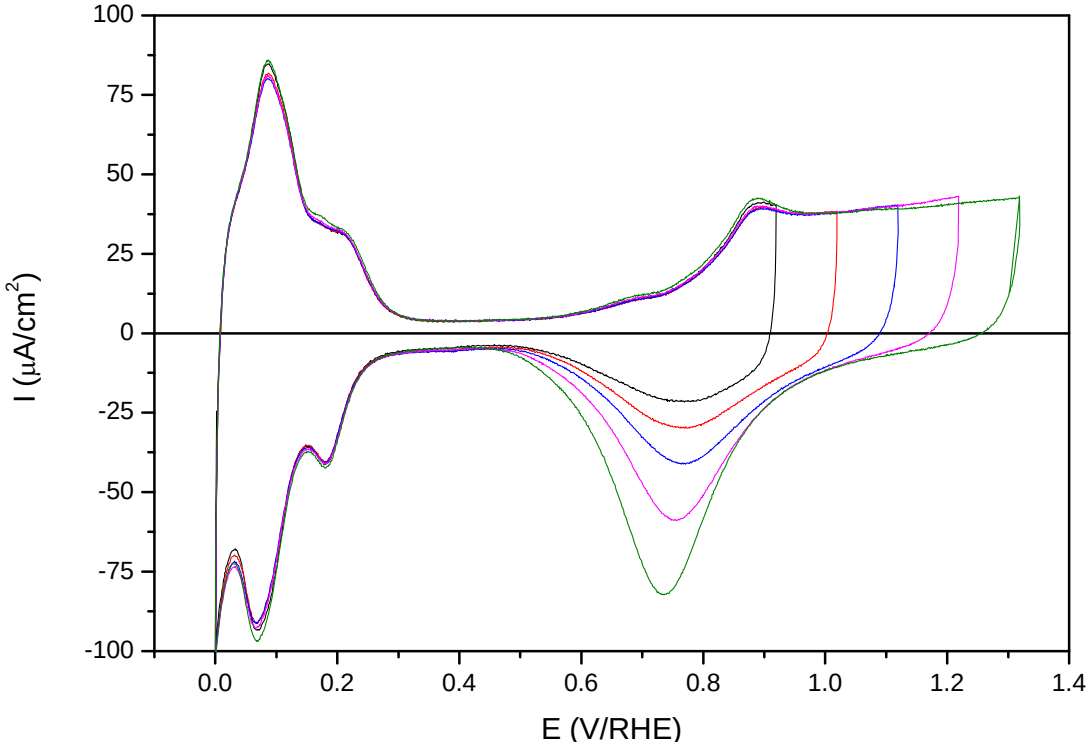

Figure 5.4 - Cyclic voltammograms on Pt coated QCM at 50mV/s in 0.1M $HClO_4$

In Figure 5.4, we show a series of CV oxidation-reduction profiles for the Pt oxide formed on these Pt QCM crystals. The maximum potential was systematically increased after each scan to demonstrate the changes in oxidation reduction process. As can be seen the oxidative process doesn't change with increasing potential. The PtO reduction peak looks very different depending on the amount of oxygen on the Pt. Initially very little shifting in the PtO reduction peak is observed. As the maximum voltage is increase to

1.1V with approximately 1/2 ML of deposited oxide, the peak starts to shift to lower potentials. This is due to a multilayer growth of platinum oxide through place exchange, represented by equation (5-5) [74-76]. Shown in Table 5.1 is a summary of these peak positions and charges.

$$PtO + Pt \rightarrow Pt + PtO \qquad \textbf{(5-5)}$$

Table 5.1 - Oxidative Charge and Reductive Peak Position

Max Scan Potential $V/_{RHE}$	Total Pt Oxide Charge $\mu A/cm^2$ (ML)	PtO Peak position V_{RHE}
0.92	114 (0.27)	0.77
1.02	171 (0.41)	0.77
1.12	236 (0.56)	0.76
1.22	317 (0.75)	0.75
1.32	398 (0.95)	0.73

The long plateau on the anodic sweep happens because platinum oxide is not limited to monolayer coverage. Rather, multilayers of PtO may form [69, 70, 77]. The onset of multilayer formation of PtO at potentials about 1.1V, results in an increased energy required for the reduction peak shifting it to lower potentials [24].

5.2 *EQCM Dissolution Study*

Platinum corrosion rates in fuel cells have been observed to increase when the catalyst is exposed to high voltage and particularly when the cell voltage is cycled [24, 46, 78-81]. It has been suggested that dynamic operation in and out of the platinum passive region can increase the metal vulnerability to corrosive conditions, namely high voltage 0.85 V vs reversible hydrogen electrode, RHE, low pH <1 [62]. Woods and Rand [82], attributed the higher dissolution rate of Pt to insufficient time of passivation when cycled. Johnson et al, reported that Pt^{2+} is produced when an oxidized platinum electrode is reduced [83]. This work demonstrates some of the capabilities of measuring platinum catalyst dissolution using these model electrode structures on with the EQCM. Quantifying the rates of catalyst loss under a cyclic condition carries relevance to predicting and mitigating the catalyst decay in a polymer electrolyte membrane PEM fuel cell during an automotive start-stop operation.

During these EQCM studies, occasionally the mass was observed to systematically decrease during potential cycling. Figure 5.5 and Figure 5.6 show the potential cycling of a Pt coated QCM at 50mV/s between 0 and 1.3V_{RHE}. As can be seen in the figures, the mass continues to drop with each cycle and this biggest observed change in mass is during the PtO reduction. The mass drop per cycle is ~ 60 ng/cm^2, which is equivalent to 0.14 ML of Pt, as one monolayer of Pt is 1ML= 421 ng/cm^2. Similar observations have been made by others and associated with the presence of hydrogen peroxide [51], or chloride contamination [84]. This dissolution could be induced by chloride contamination even though every effort is made to prevent chloride contamination from entering the cell from the Ag/AgCl reference electrode through use of a salt bridge or double frit junction.

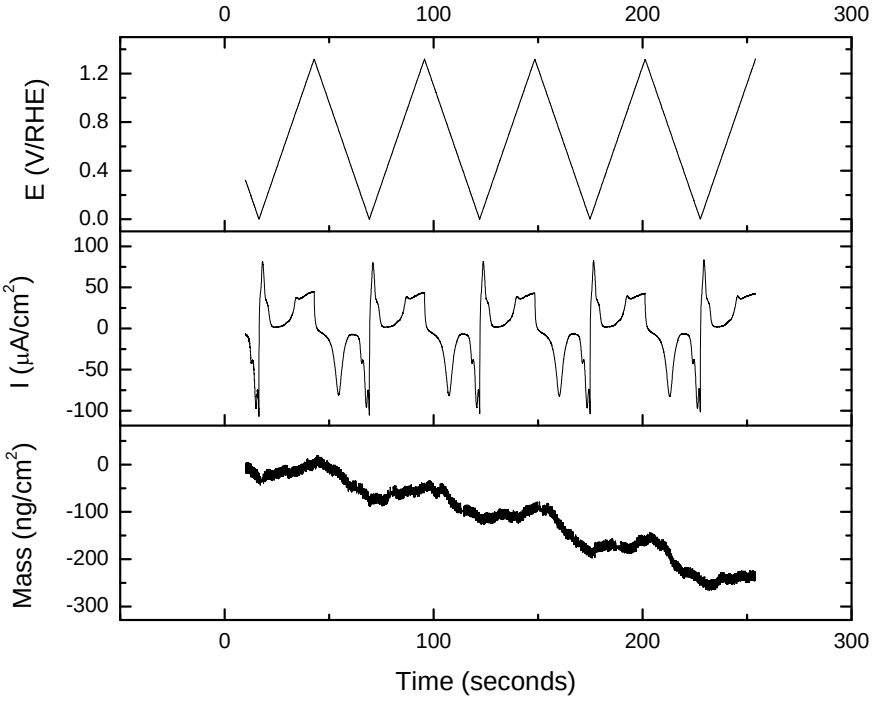

Figure 5.5 - EQCM observed mass loss during CV cycling at 50mV/s (0 - 1.3V_{RHE})

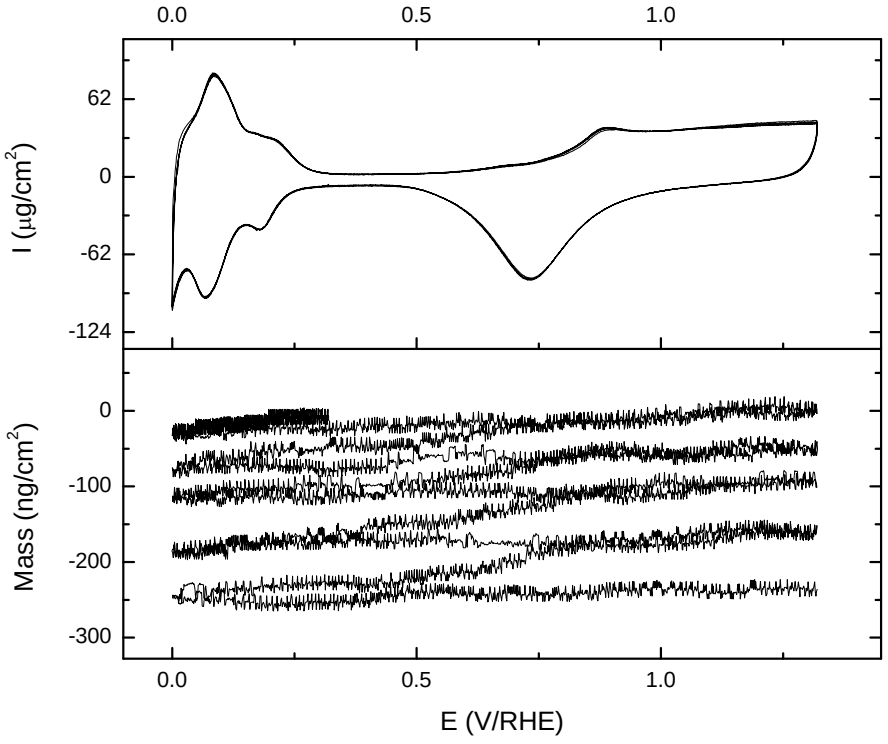

Figure 5.6 - Massogram showing mass loss during potential cycling

Potentiostatic experiments were conducted to directly measure the Pt dissolution rate as a function of potential at room temperature. At high potentials, only a limiting oxide growth was observed. However, at a $1.0V_{RHE}$ in 0.1M $HClO_4$ (pH=1), a small amount of Pt corrosion was observed. Initially the mass increased due to oxidation. The dip during this oxide growth region was believed to have been caused by a gas bubble on the electrode edge. After a mass growth equivalent to ~2 ML of oxide, the mass begins to fall. This behavior is similar in shape to that observed by Dam at elevated temperatures [85]. The drop of 150 ng/cm^2 then levels off. The electrochemical cell contained 70 ml of electrolyte, so if all of this mass change stayed in solution the platinum molar concentration would be $[Pt]=3x10^{-8}$ M, which is only slightly higher than that predicted by Pourbaix [62].

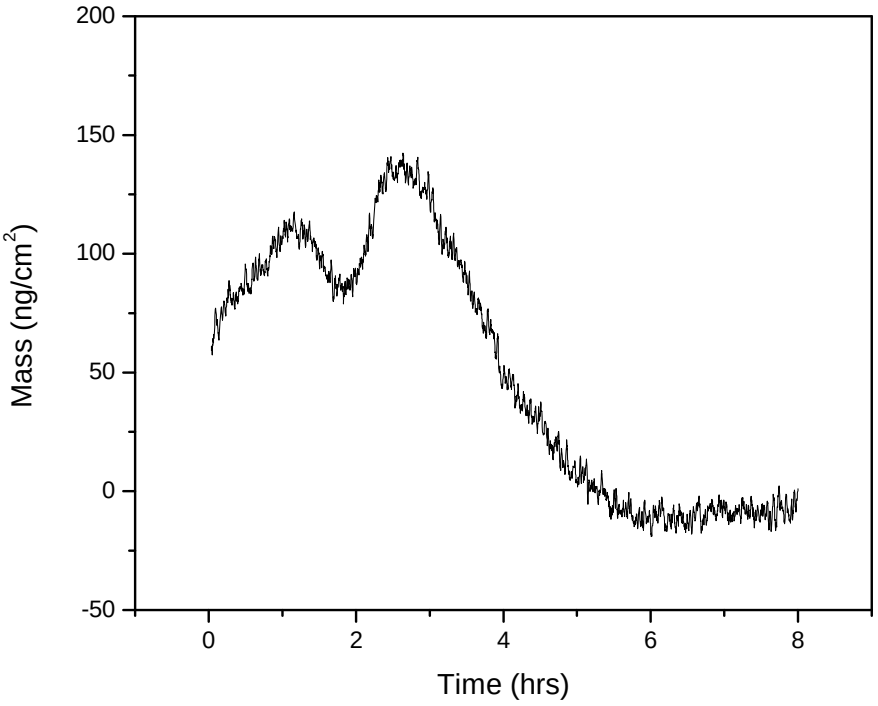

Figure 5.7 - Potentiostatic mass loss at 1.0V

5.3 *EQCM Nanoparticle Sintering Study*

All of the EQCM studies described so far have been on sputter Pt films that fully cover the QCM crystal surface. These crystals have been shown useful for studies of Pt oxidation/reduction and dissolution, but to study sintering a new model surface needed to be fabricated. Pt/C QCMs were fabricated to measure the affects of oxidation/reduction and dissolution on the sintering of carbon supported platinum nanoparticles. The crystal surface was first coated with an adhesion layer of titanium 10 nm thick, followed by a 200 nm thick carbon film. These films were grown by DC magnetron sputter deposition in ultrahigh purity argon. The sputter targets were titanium, 0.9995 purity and graphitic carbon 0.999 pure. Since sputtering is an energetic process the growing carbon film did not maintain the same bonding nature of the bulk target. X-ray photoelectron spectroscopy (XPS) was used to determine the electronic state of the carbon in these deposited films. As can be seen in Figure 5.8, the carbon film is mostly diamond like in nature with only 18% graphitic bonds.

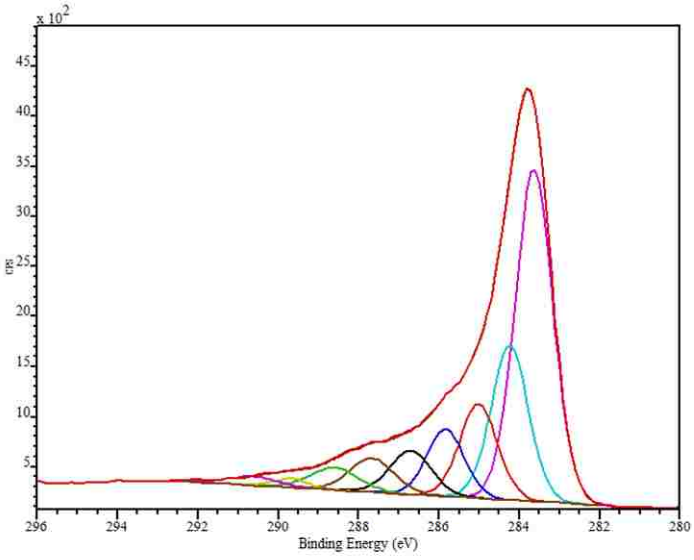

	Energy (eV)	*Sample %*
Diamond	*283.6*	*45.9*
Graphite	*274.2*	*18.3*
C-C-O*	*285.2*	*10.7*
CN, C≡N	*285.8*	*7.9*
C-OC	*286.7*	*5.9*
N-C-O	*287.7*	*5.2*
C=O	*288.6*	*3.6*
COOH	*289.7*	*1.2*
shakeup	*290.6*	*1.3*

Figure 5.8 - XPS results from sputtered carbon film with peak fitting results

Pt was deposited by e-beam evaporation onto this sputtered carbon film. Physical vapor deposition by evaporation with a quartz crystal microbalance allows exceptional control over the deposition rate and quantity. A discontinuous film is formed at low loadings of 2.1 $\mu g/cm^2$ or less, as platinum is non-wetting on carbon. A schematic of the model Pt/C QCM is depicted in Figure 5.9.

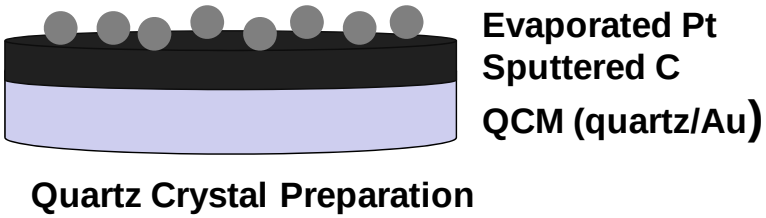

Figure 5.9 - Schematic of Pt/C EQCM sample

Two crystal surfaces were prepared with different Pt loadings of 1.0 and 2.1 $\mu g/cm^2$. The prepared Pt/C crystal surface was then mounted into the EQCM holder as the working electrode and placed into an electrochemical cell with Argon purged 0.1M $HClO_4$ acid. Prior to the measurements, the working electrode was pretreated by a potential cycle between 0 and 1.4 V_{RHE} at a rate of 500 mV/s until the cyclic voltammogram was repeatable, which took 40 cycles. After this initial conditioning, a CO stripping measurement was conducted to determine the Pt electrochemical active surface area (ECSA). This represents the initial surface prior to the aging treatment. The Pt particles were also imaged with a scanning electron microscope (SEM) at this time. The first aging

treatment was 140 potential cycles at 20mV/s between 0 and 1.2V_{RHE} in argon purged electrolyte. The ECSA was again measured and revealed a loss of 13 – 25% of the surface area. Another aging treatment was then performed with 50 potential cycles at 20mV/s between 0 and 1.2V_{RHE} in oxygen saturated electrolyte. The CO stripping measurement revealed another loss of 18 – 23% with only 1/3 of the number of cycles. A summary of these results is shown in Table 5.2, along with a representative CV in Figure 5.10.

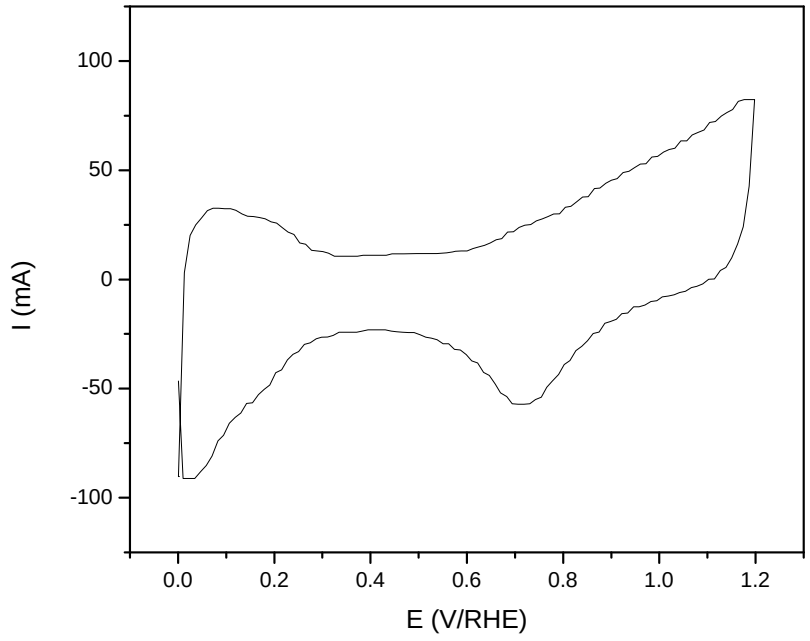

Figure 5.10 - CV of Pt/C QCM

Table 5.2 - Summary of Pt/C QCM aging

Pt/C QCM	1.0 µg Pt/cm^2 ECSA (cm^2)	SEM Image area fraction	2.1 µg Pt/cm^2 ECSA (cm^2)	SEM Image area fraction
Initial Conditioning (0.05 ↔ 1.4V_{RHE}) 500mV/s 40 cycles - Ar	1.27	0.16	2.48	0.33
Aged (0.05 ↔ 1.2V_{RHE}) 20mV/s 140 cycles - Ar	1.11 (0.87)		1.86(0.75)	
Aged (0.05 ↔ 1.2V_{RHE})	0.91 (0.72)	0.06	1.44(0.58)	0.21

20mV/s 50 cycles - O_2				

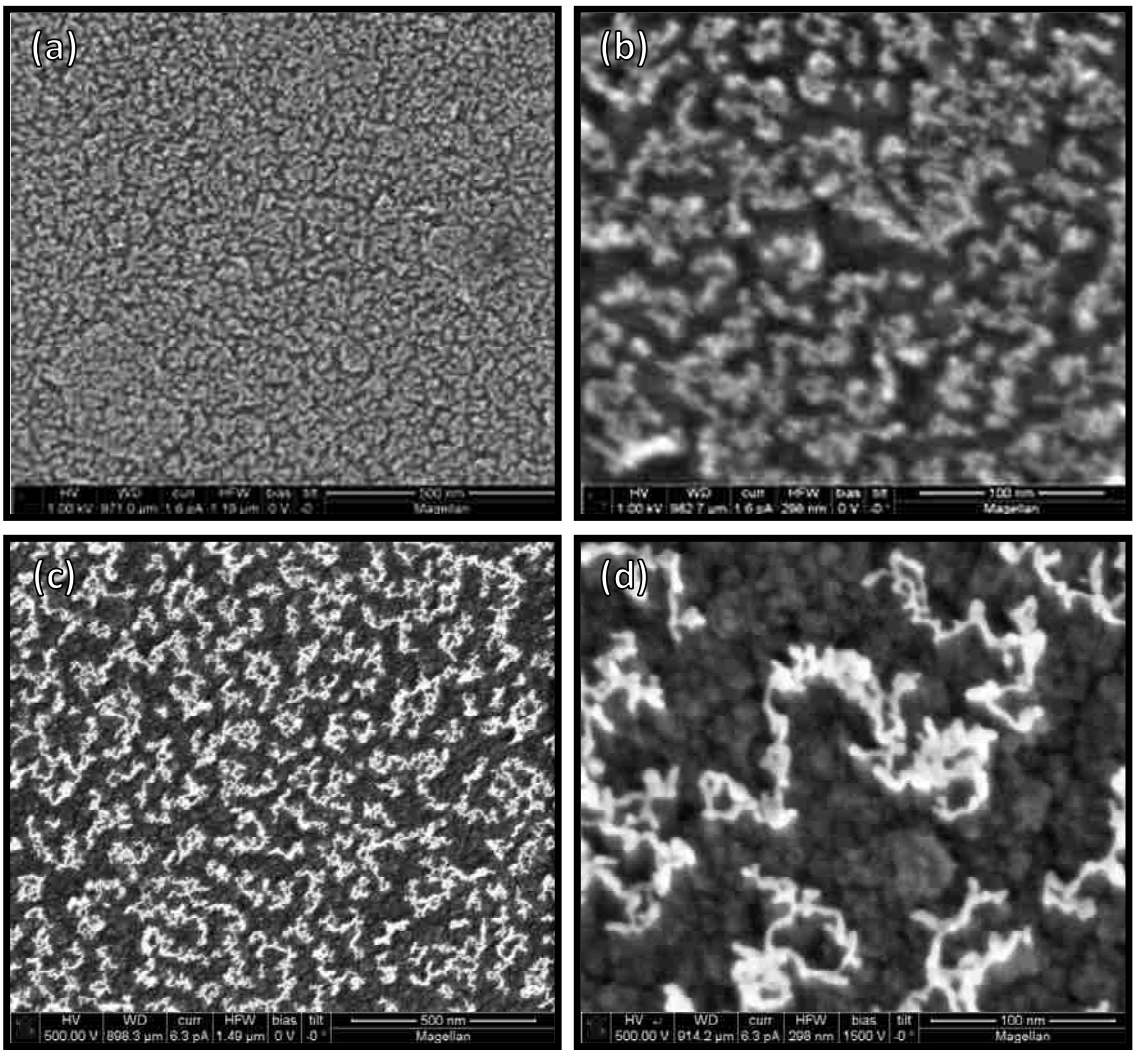

Figure 5.11 - SEM of Pt sintering at a loading of 2.1 ug/cm2 after (a,b)initial conditioning and (c,d) after 190 cycles 0 – 1.2V

These unique Pt/C QCMs are too large to fit in the Hitachi 5200 SEM and so the FEI Magellan™ at Sandia National Labs was used for this imaging. The FEI Magellan™ is capable of sub-nanometer resolution at low electron beam energies. Figure 5.11(a and b) contain the images of the 2.1 μg Pt/cm^2 sample after initial conditioning, while (c and d) show the Pt particles after the aging treatment described above. From the SEM images we

can see that the loss of surface area is from the formation of Pt nanowires. The total metal on the surface was difficult to quantify from these random nanowire formations.

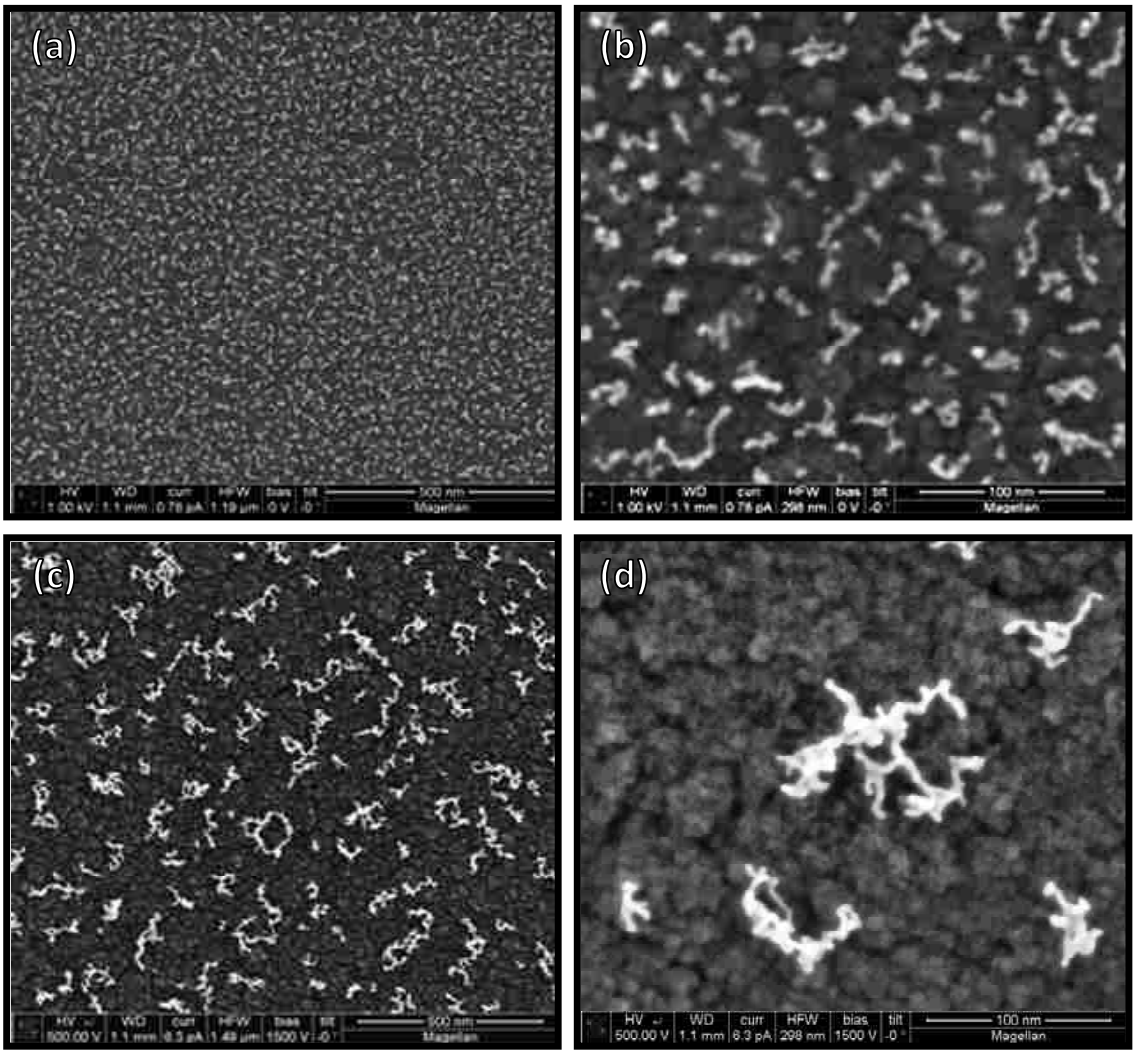

Figure 5.12 - SEM of Pt sintering at a loading of 1.0 ug/cm^2 after (a,b)initial conditioning and (c,d) after 190 cycles 0 – 1.2V

Figure 5.12(a),(b) contain the images of the 1.0 μg Pt/cm2 sample after initial conditioning, while (c),(d) show the Pt particles after the aging treatment described above. From the SEM images a similar sintering behavior to the higher loaded sample is observed again with the formation of Pt nanowires. Sintering is occurring, but into elongated shapes

not into large spherical particles. Elongated nanowire shapes should result in a slower loss of surface area versus spherical particles.

5.4 *Summary*

The electrochemical quartz crystal microbalance (EQCM) has been shown to be a useful technique to assess the durability of fuel cell catalyst materials. When combined with other experimental methodologies such as CV and SEM, EQCM is a powerful tool in research on electro-oxidation of noble-metal electrodes and provides an insight into the interfacial mass balance.

Cycling parameters, such as scan rates and upper voltage limit, have been found to impact the rate of decay in platinum electrochemical area ECSA. While dissolution was observed during potentiostatic testing, potential cycling significantly enhanced the dissolution rate of Pt.

The experimentally determined molecular weight of the Pt surface oxide was 14.2 g/mol assuming a 2 electron process, which implies the addition of O^{-2} to the surface and PtO as the oxide species formed.

Electro-oxidation of platinum does involve the initial deposition of OH as an intermediate surface layer for ~1/4 ML. The oxidation process proceeds with the formation of PtO up to half a monolayer of O that resides on-top of the Pt surface without any place exchange. The process continues with the formation of PtO above 1/2 ML but with the growth of a multilayer through place exchange between O adatoms and the top most Pt

surface atoms. This place exchange occurs at potentials of 1.1 V_{RHE} and above. The interfacial place exchange leads to the development of a multi-layer surface lattice comprising Pt^{2+} cations and O^{2-} anions. Upon reduction this multilayer leads to an enhanced rate of platinum dissolution.

A QCM crystal with Pt nanoparticles on carbon was created by the sputter deposition of a carbon layer. Sintering on this sputtered carbon surface proceeded through the formation of Pt nanowires. The nanowire formation mechanism from either particle agglomeration or ripening in the presence of a surface contaminant was not determined.

Testing protocols involving the formation of a multilayer oxide combined with potential cycling result in the highest rate of platinum dissolution.

Chapter 6

Pt on GC Model Electrode

The focus of this research is the development and study of model electrode surfaces to provide insights into the electrocatalyst degradation. The planar support surfaces enable the use of surface analysis techniques such as electron microscopy imaging on the same surface that is electrochemically tested with cyclic voltammetry.

The model supports used in this study were 5 mm diameter glassy carbon electrodes from Pine Instruments that are press fitted into a removable Teflon RDE tip. The electrodes are polished with 0.05 μm alumina. The Pt catalyst was deposited directly on the glassy carbon (GC) support by e-beam evaporation using high purity Pt metal (99.999%) at a pressure of 5 x 10^{-7} torr or better. The amount of metal deposited was controlled by an in-situ quartz crystal microbalance.

6.1 *Particle size control*

Platinum on carbon is non-wetting so a continuous film is not formed during deposition at very low loadings. The growth of this type of film is referred to as Volmer-Weber (VW) type of growth, also known as island formation. In VW growth the adatom to adatom interactions are stronger than those of the adatom to surface interaction, which leads to a three-dimensional formation of adatom clusters. For this reason, a mass loading description of the deposited film will be used instead of film thickness. Platinum has a density of 21.4 g/cm^3, so a film with a 1 nm thickness would have a mass loading of 2.1 μg/cm^2. Examples of the model catalysts used in this study are shown Figure 6.1.

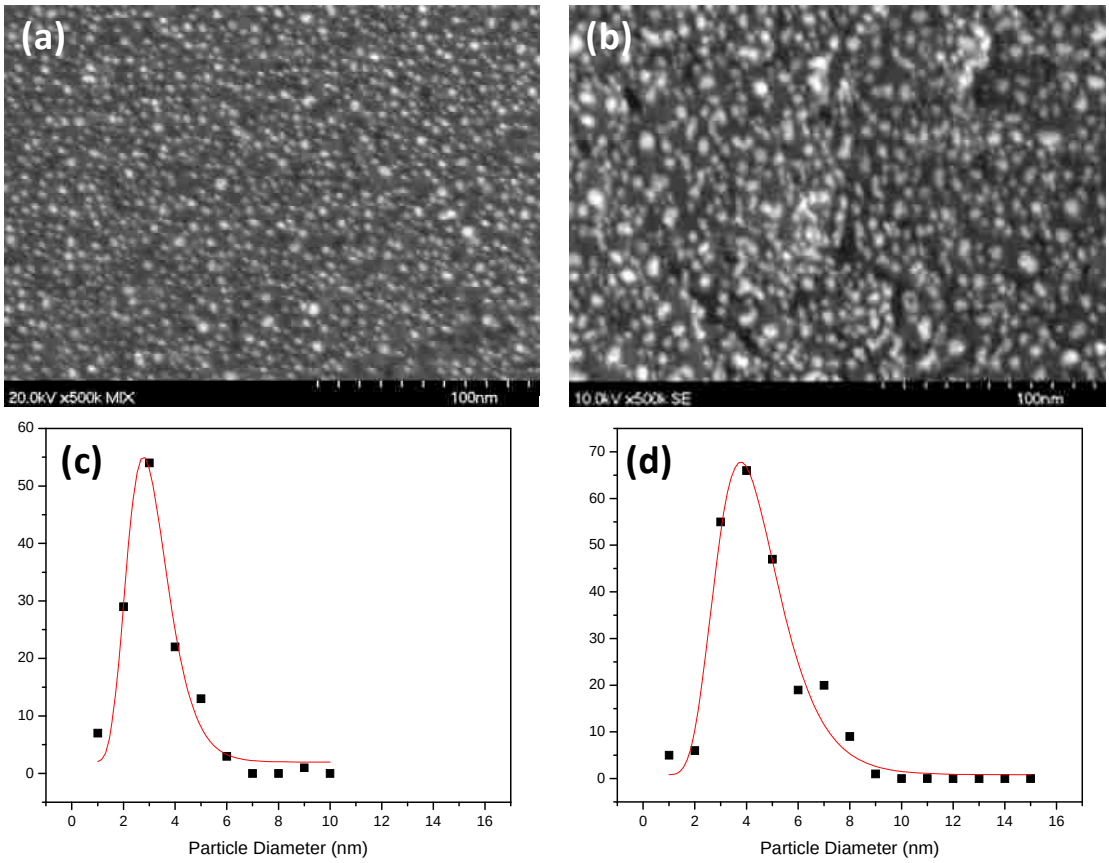

Figure 6.1. - SEM images of Pt nanoparticles on a model glassy carbon support with a surface loading of (a) 1.1 µg/cm^2 and (b) 2.1 µg/cm^2. These samples were heated to 800 °C to generate observed particle size distribution with an average size of 2.7 nm in (c) and 4.3 nm in(d).

Two different particle size distributions can be seen in Figure 6.1, which were generated by depositing a thin layer of platinum followed by anneal step at 800 °C. The anneal involved a temperate ramp of 30 °C/min and holding at 800 °C for 30 seconds in ultrahigh vacuum, < 10^{-9} torr. With a platinum loading of 1.1 µg/cm^2, the result is a log-normal distribution with an average particle size of 2.7 nm. At a platinum loading of 2.1 µg/cm^2, again a log-normal distribution was generated but with an average particle size of 4.3 nm.

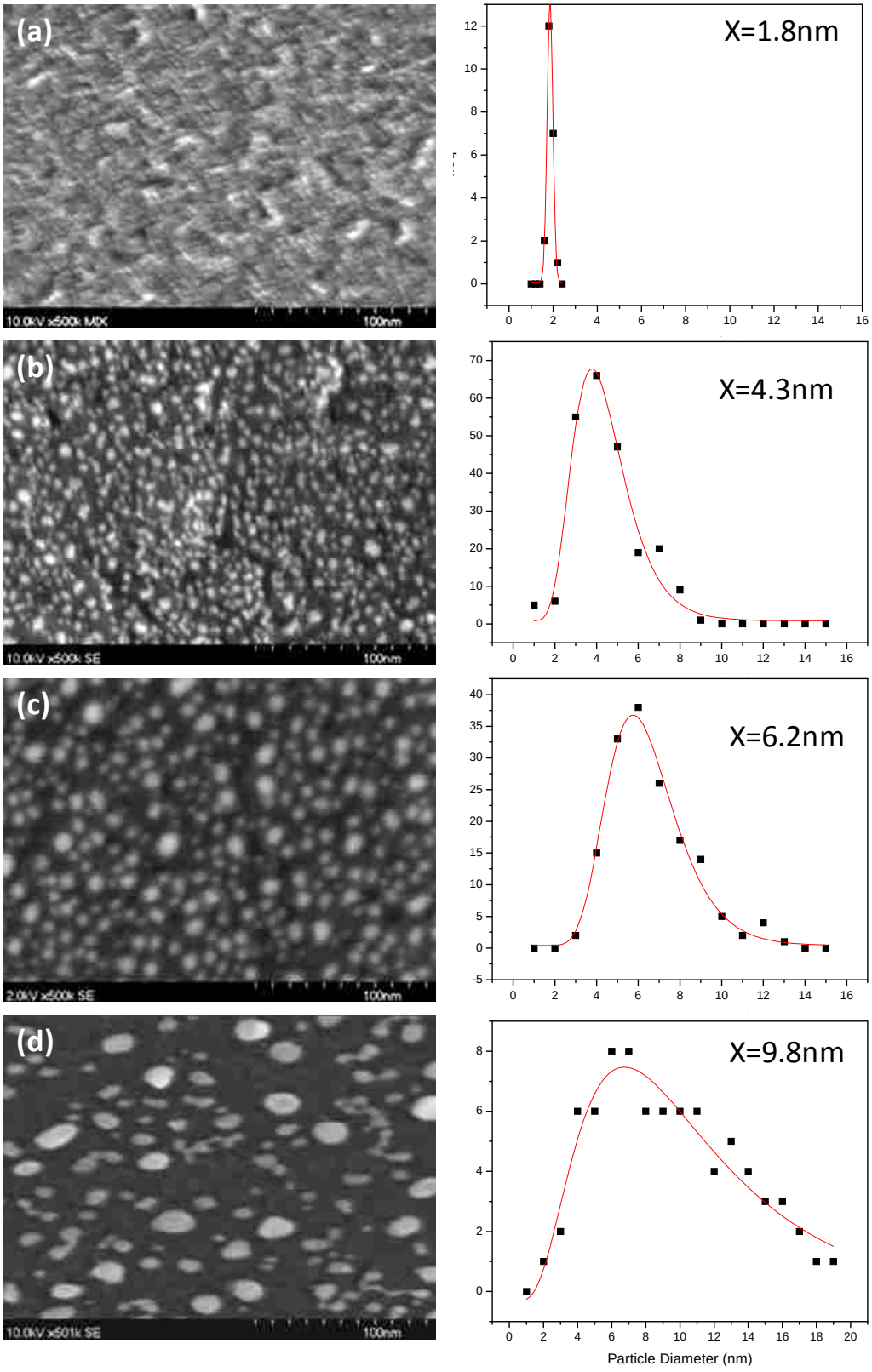

Figure 6.2 - Pt particle size distribution as a function of annealing temperature (a) as deposited, (b) 800°C, (c) 1000°C, (d) 1100°C

In addition to controlling the particle size by changing the amount of metal deposited, the particle size can be altered by changing the annealing temperature. In Figure 6.2, the particle size distributions can be seen starting with the as deposited film at a loading of 2.1 $\mu g/cm^2$. Figure 6.2(a) shows this Volmer-Weber type of growth for Pt on carbon, which resulted in an average particle size 1.8 nm in a very narrow Gaussian distribution. Annealing steps were added to this initial deposition to change the particle size. Each annealing step used a temperature ramp rate of 30 °C/s and holding at the final temperature for 30 seconds in ultrahigh vacuum, $< 10^{-9}$ torr, only the final temperature was varied. At a final temperature of 800 °C, the average particle size was 4.3 nm. With a final temperature of 1000 °C the average particle size was 6.2 nm. When the anneal temperature was increased to 1100 °C, the average particle size increased to 9.8 nm with the dramatic appearance of some large particles up to 20 nm in size.

These model supports were imaged by high resolution scanning electron microscopy (SEM) using a Hitachi 5200. Pt particles sizes down to 1 nm in diameter can be imaged with this system. A custom holder to cleanly mount and remove these glassy carbon electrodes for imaging was created. This arrangement enabled the catalytic activity of the deposited/sintered particles to be measured using rotating disk electrode (RDE) techniques and then cycle between these electrochemical measurements and SEM imaging to observe the catalyst deactivation process. The custom SEM boat can be seen in Figure 6.3. Small set screws on the ends of the boat secure the electrode for transfer into the SEM. Using these custom holders no damage to the Pt nanoparticles was observed when cycling between the electrochemical tests and SEM imaging.

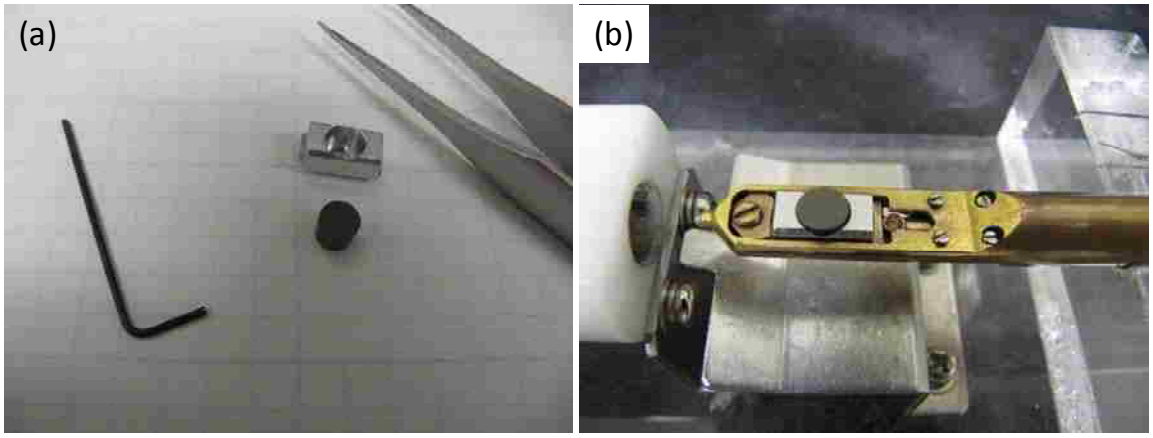

Figure 6.3 - Custom SEM boat for glassy carbon electrodes (a) SEM boat, GCE and tools (b) mounted in the IN-LENS SEM holder

6.2 *Nanoparticle size effects*

The modification to the chemical potential by small nanometer size particles was previously described in section 2.2.1. The application of the Gibbs-Thomson equation to the Nernst equation provided a prediction of the anticipated change in equilibrium electrochemical potential as a function the radius of curvature.

The impact of this nanoparticle size effect can be seen in the RDE data. The most obvious peak in the cyclic voltammogram is the platinum oxide reduction peak during the cathodic scan. The position of this cathodic peak occurs at some offset from the equilibrium potential and therefore should reflect a shift in the equilibrium potential. In Figure 6.4, the peak position shift for the 3.4nm particles was observed to be -70mV, while the peak shift for a 4.1 nm particles was -40 mV relative to the bulk polycrystalline Pt electrode. These changes are in good agreement to the ΔE values predicted by the modified Nernst equation if we assume the surface is mostly Pt(111) of 54 mV and 44 mV for

diameters of 3.4nm and 4.1nm respectively. The peak heights are smaller for the nanoparticles because of a smaller active surface area.

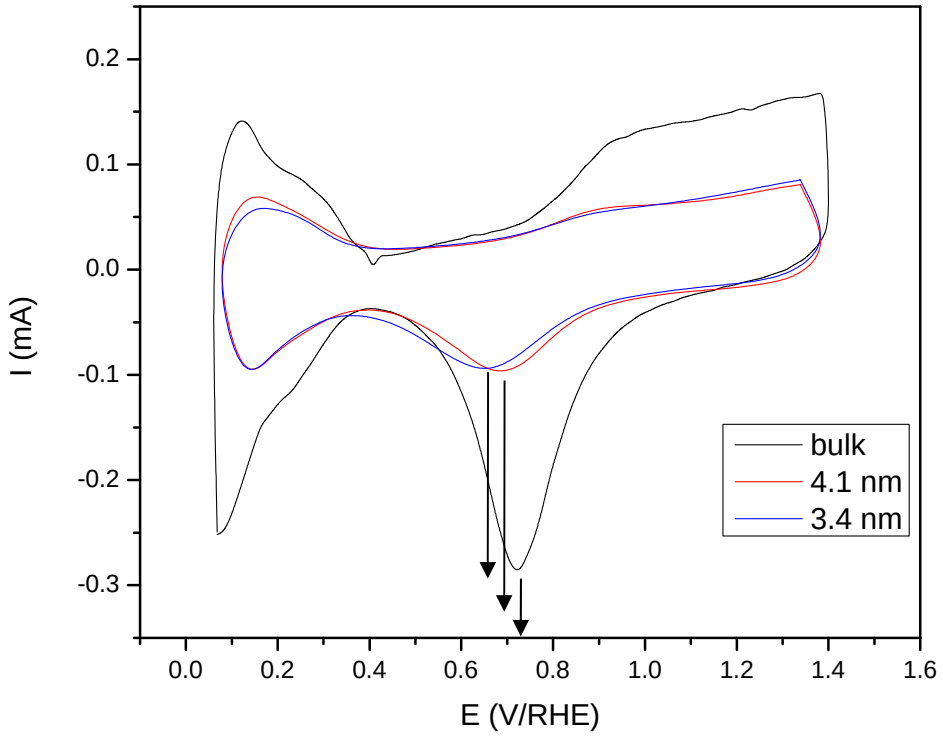

Figure 6.4 - Pt oxide reduction peak shift with cathodic scan at 200 mV/s. Pt nanoparticles on GC of 3.4nm, 4.1nm vs. a bulk polycrystalline Pt electrode.

Figure 6.5 shows a better view of the position of this cathodic PtO peak for a 2.1 μg/cm^2 Pt on glassy carbon contrasted against a polished bulk poly crystalline Pt electrode. The nanoparticle peak is plotted on a different axis to account for the low surface area. A shift of ~40 mV is observed in this peak position, which is typically centered around 760 mV for a solid poly crystalline Pt electrode. This compares very well with the particle size effect previously reported by Mayrhofer [86] and Gasteiger [10]. The Pt oxide formation

peak was difficult to measure accurately due to the very low Pt loading and the gradual nature of platinum oxide formation.

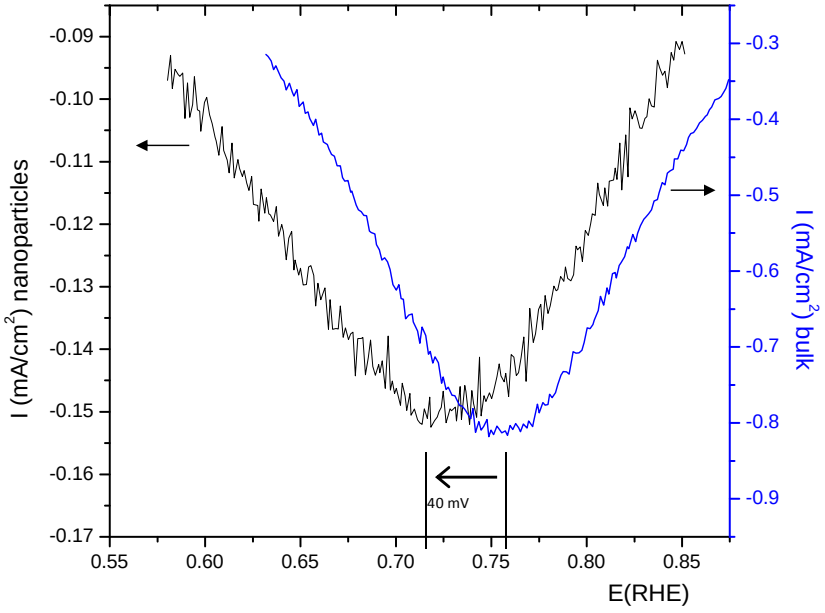

Figure 6.5 - Pt oxide cathodic scan peak shift at 200 mV/s. Pt nanoparticles on GC vs. a bulk polycrystalline Pt electrode

6.3 *Oxygen Reduction Reaction*

The oxygen reduction reaction (ORR), with the overall reaction of $O_2 + 4H^+ + 4e^- \rightarrow 2H_2O$ is a fundamentally important electrocatalytic reaction for fuel cells. There are no electrode materials for which there is even a measurable current from oxygen reduction at the theoretical equilibrium potential of 1.23V versus the normal hydrogen electrode (NHE). Even for the most catalytically active electrode materials, the platinum group metals, measurable reaction currents are only obtained below 1V [48]. The model catalytic electrodes created for these studies must therefore be reasonably active for the ORR to be relevant to studies of fuel cell catalyst degradation.

Evidence that this type of model system is catalytically active is shown in Figure 6.6. The oxygen reduction reaction results from the RDE experiments are shown comparing a model nanoparticle Pt/GC catalyst to a bulk Pt electrode. The image shown is for a 2.1 $\mu g/cm^2$ Pt loaded GC support at a sweep rate of 50 mV/s, a rotation rate of 1600 rpm in oxygen saturated 0.1M $HClO_4$ at 20 °C. The reference electrode used was Ag/AgCl but all data shown is with respect to the reversible hydrogen electrode (RHE). The Pt nanoparticles, measured to be 2.6 nm in size, on glassy carbon exhibit good ORR activity. The slight shift in the half-way potential, $E_{1/2}$, to lower potentials is expected based on the low loading and particle size [87-89].

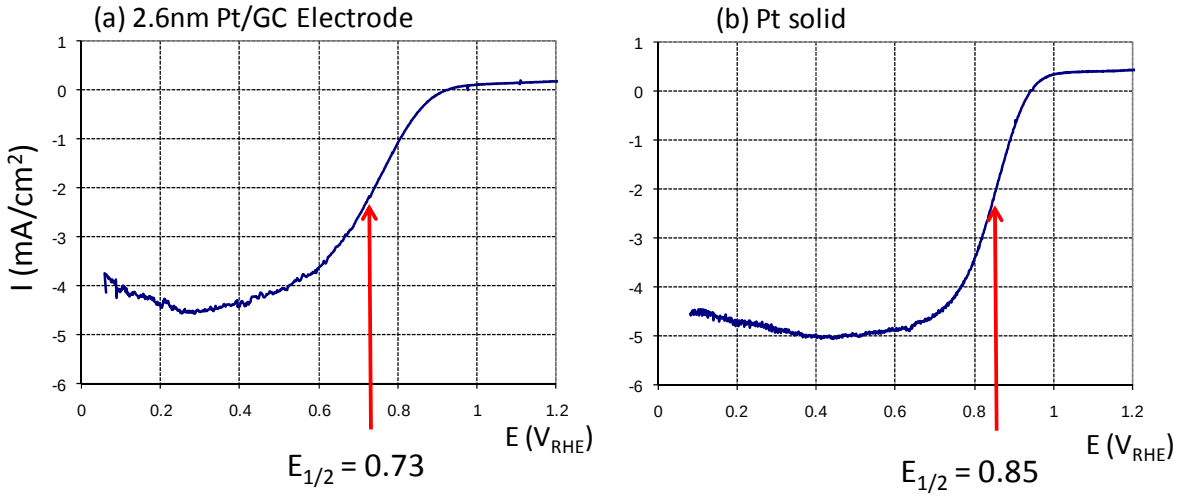

Figure 6.6 - ORR RDE results on model catalyst (a) 2.1 µg/cm² Pt/glassy carbon and (b) solid polycrystalline Pt.

This potential cycle in an oxygen saturated electrolyte was repeated from 0.05 to 1.2 V_{RHE} for 100 cycles. The current density at low potentials decreased by 20%, indicating a loss in active surface area. The electrode was then removed for imaging. The capability of the high resolution SEM microscope are demonstrated well in Figure 6.7.

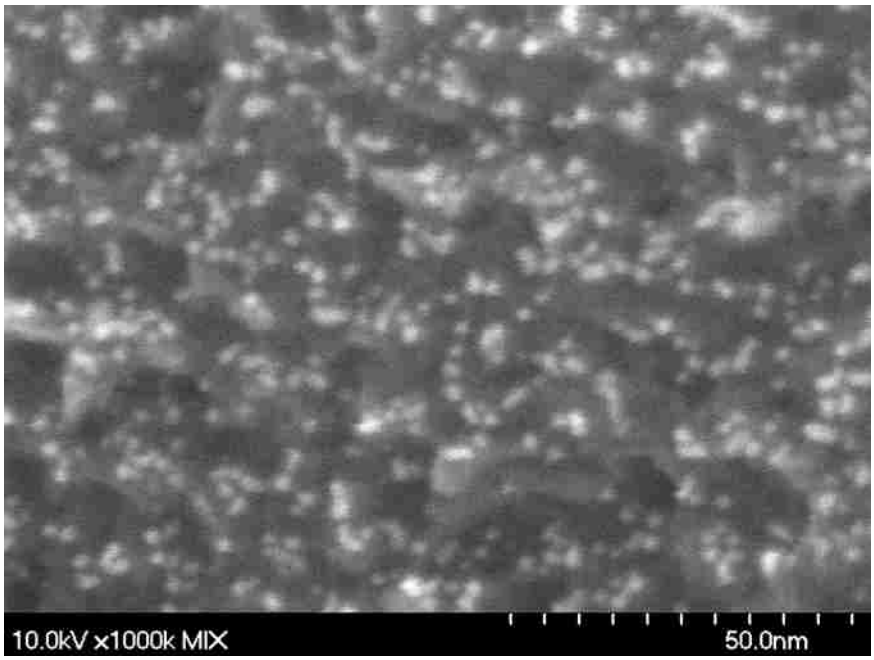

Figure 6.7 - SEM image of Pt/C after ORR cycling. Pt nanoparticles and carbon corrosion are visible

Pt particles, ~1 – 2 nm in size, are visible on the carbon surface. Pitting in the glassy carbon is also observed. The loss of active surface area was determined to be predominately from carbon corrosion and particle detachment. Very few Pt particles are visible in the pits on the glassy carbon surface.

6.4 *Aging studies*

The objective of this study was to evaluate degradation issues of electrode materials such as the catalyst and the carbon support due to potential cycling in acid electrolytes. This would allow us to understand the degradation mechanisms of various electrode processes such as the reduction of oxygen. Electrode degradation is most severe at the PEM cathode due to an oxidizing environment at the cathode.

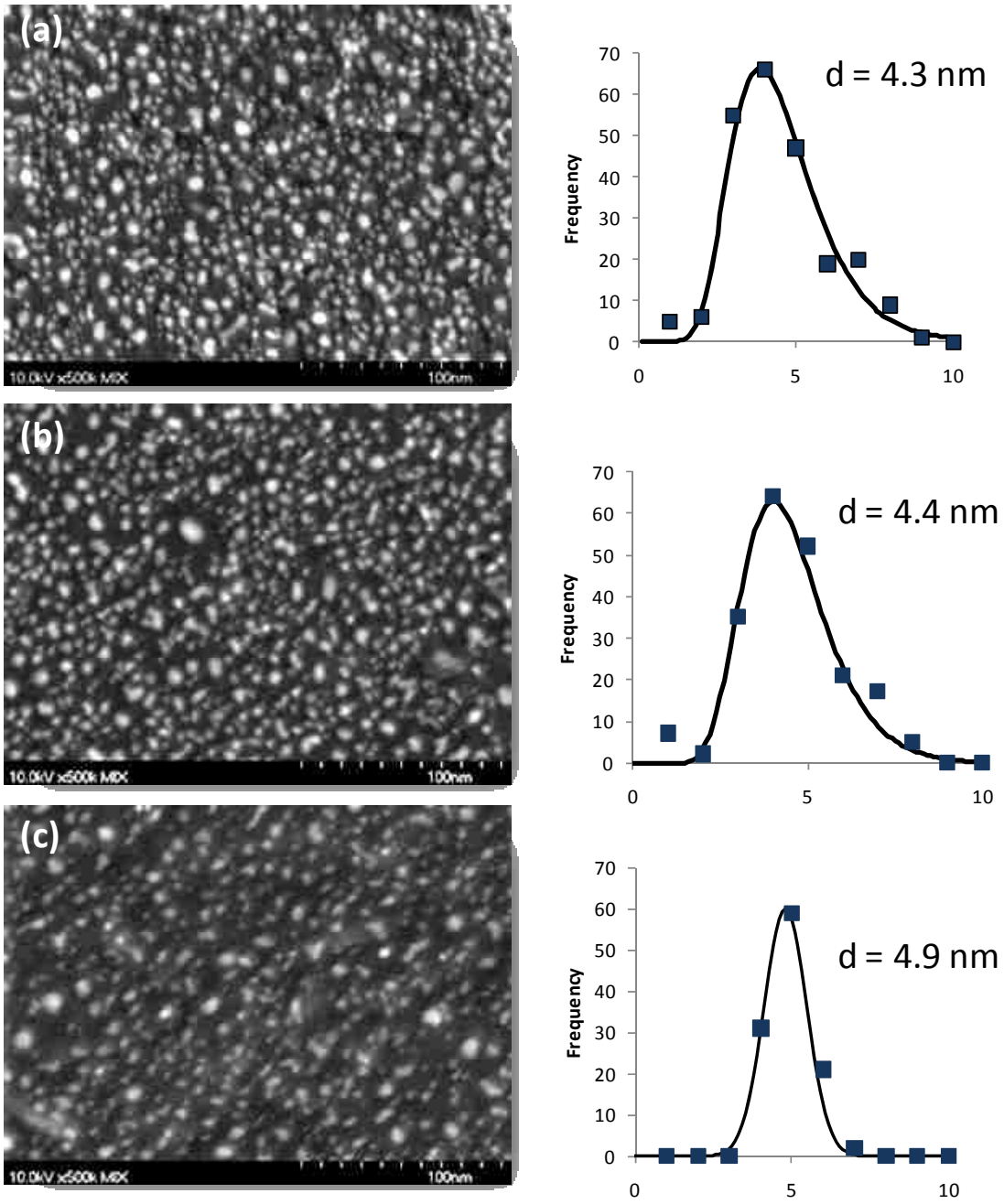

Figure 6.8 - 2.1 µg/cm^2 Pt annealed at 800C (a) initial PSD, (b) after conditioning (0 - 1.4V), (c) 500 cycles 0.6 – 1.2V$_{RHE}$

Figure 6.8 shows an aging study conducted on a 2.1 μg/cm^2 Pt on glassy carbon annealed at 800 °C. The initial particle size distribution was created by annealing the electrode is shown in figure (a). The sample was conditioned by repeat cycling at 500 mV/s from 0 – 1.4 V_{RHE} in argon purged 0.1M $HClO_4$ until the CV was repeatable. This conditioning took 40 cycles and as can be seen in figure (b) had only a minor affect on the particle size distribution. The electrode was then aged for 500 cycles, just through the Pt oxidation/reduction regime (0.6 – 1.2 V_{RHE}). at 50 mV/s in the same argon purged 0.1M electrolyte. As can be seen in figure (c), even though the average particle size increased to 4.9 nm this was mostly due to the loss of small particles. This mechanism is known as Ostwald ripening, where the larger particles grow at the expense of the smaller particles. Ostwald ripening as the predominant mechanism is further supported by the change of the particle size distribution from log normal to a more Gaussian shape. However, the overall particle density dropped more than can explained by Ostwald ripening alone, so surface area loss from Pt dissolution is also occurring.

Another aging study starting with the small particle distribution of the as deposited Pt was conducted in the same Pt oxidation/reduction regime. As can be seen in Figure 6.9, the initial particle size and shape change significantly during the initial condition cycles from 0 – 1.4 V_{RHE} at 500 mV/s. Particle size distributions were not generated due to the unusual Pt elongated shapes which were more like nanowires and not spherical. The diameter of these wires was around 3.0 nm. The CV during this initial conditioning process is shown in figure (d).

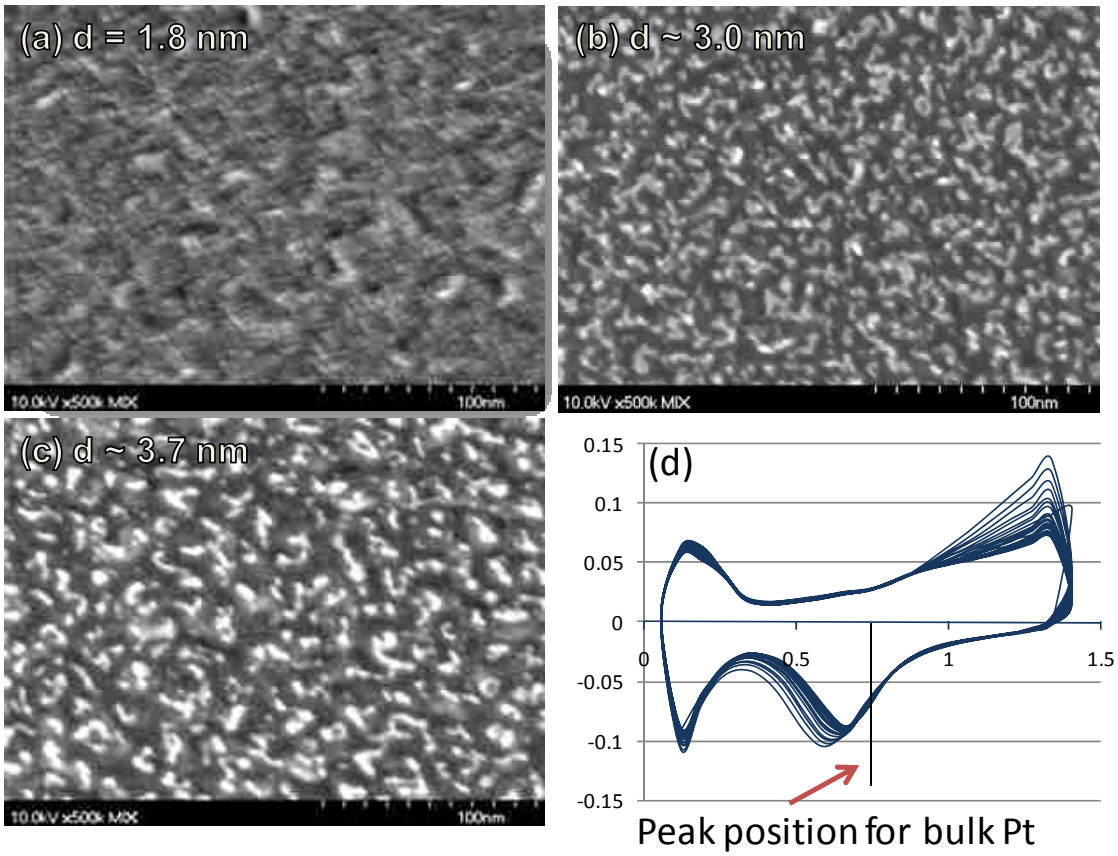

Figure 6.9 - 2.1 µg/cm^2 Pt as deposited (a) initial PSD, (b) after conditioning (0 - 1.4V), (c) 500 cycles 0.6 – 1.2V$_{RHE}$ (d) initial conditioning cathodic peak shift

The growth in particle size and loss of surface can be seen in the CV with the shift to the right of the PtO reduction peak, along with the decrease in the height. The electrode was then aged for 500 cycles, just through the Pt oxidation/reduction regime (0.6 – 1.2 V_{RHE}). at 50 mV/s. These elongated nanowire shapes continued to grow with these additional cycles and the average diameter of the nanowires increased to ~3.7 nm. A summary of the data from these two aging studies is shown in Table 6.1

Table 6.1 – Summary of aging data on 2.1 μg/cm^2 Pt/GC

	2.1 μg/cm^2 (As Dep.)	**2.1 μg/cm^2 (800°C)**
Initial SEM Particle Size	~1.7 nm	4.3 nm
Conditioned SEM Particle Size (ECSA cm^2)	3.0 nm (0.19)	4.4 nm (0.17)
500 cycles (0.6 ↔ 1.2V RHE) Ar SEM Particle Size (ECSA cm^2)	3.7 nm (0.13)	4.9 nm (0.13)

6.4.1 Microscopic Aging Study

In order to gain more insight into the degradation mechanism of fuel cell catalysts, we created an imaging reference mark on the surface of the electrode. This mark was a scratch made by a clean diamond scribe across the surface of the electrode in two directions forming a cross. One of the scribe marks did not go all the way to the electrode edge so that mounting in the SEM could be visually oriented the same each time. Using our non-destructive experimental procedures based on SEM or RDE electrodes combined with an imaging reference mark enabled the investigation of an identical location on a catalyst before and after each electrochemical treatment.

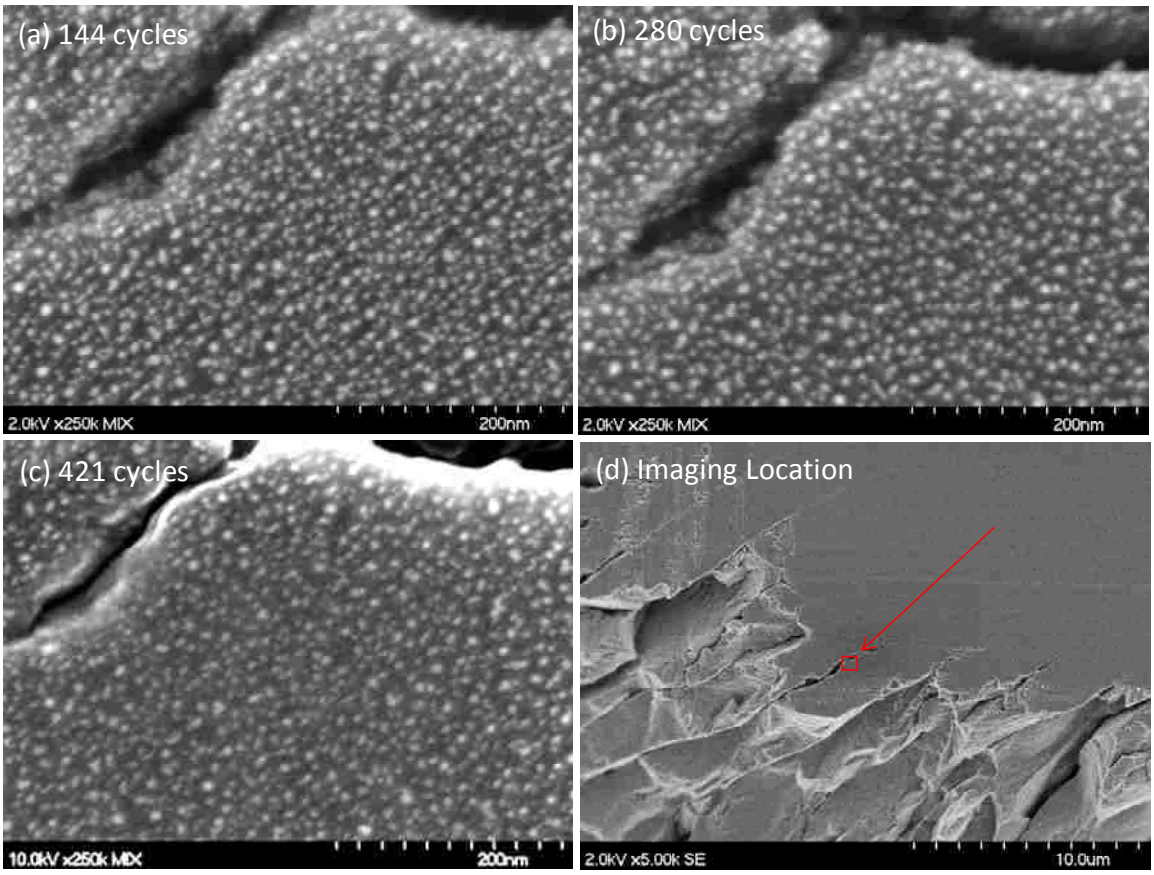

Figure 6.10 - SEM images of the same area during aging process with cycles of 0.6 – 1.2 V_{RHE} at 50mV/s

The results of this imaging of the same location through an aging study are shown in Figure 6.10. The image in Figure 6.10(d) shows the location selected for SEM imaging near the center of the scribed cross. Low magnification imaging enables the general location to be found quickly. Then saved images at magnifications like this allow the high magnification location to be centered for imaging. The aging process consisted of cycles of 0.6 – 1.2 V_{RHE} at 50 mV/s in argon purged 0.1M $HClO_4$ electrolyte. In general only minor changes are observed. After 421 cycles, the particles are starting to look smaller indicating that dissolution of the platinum is taking place. SEM imaging of the same region became increasingly difficult because of e-beam deposition of carbon. This deposition on the imaging location will need to be mitigated before longer imaging studies can be conducted.

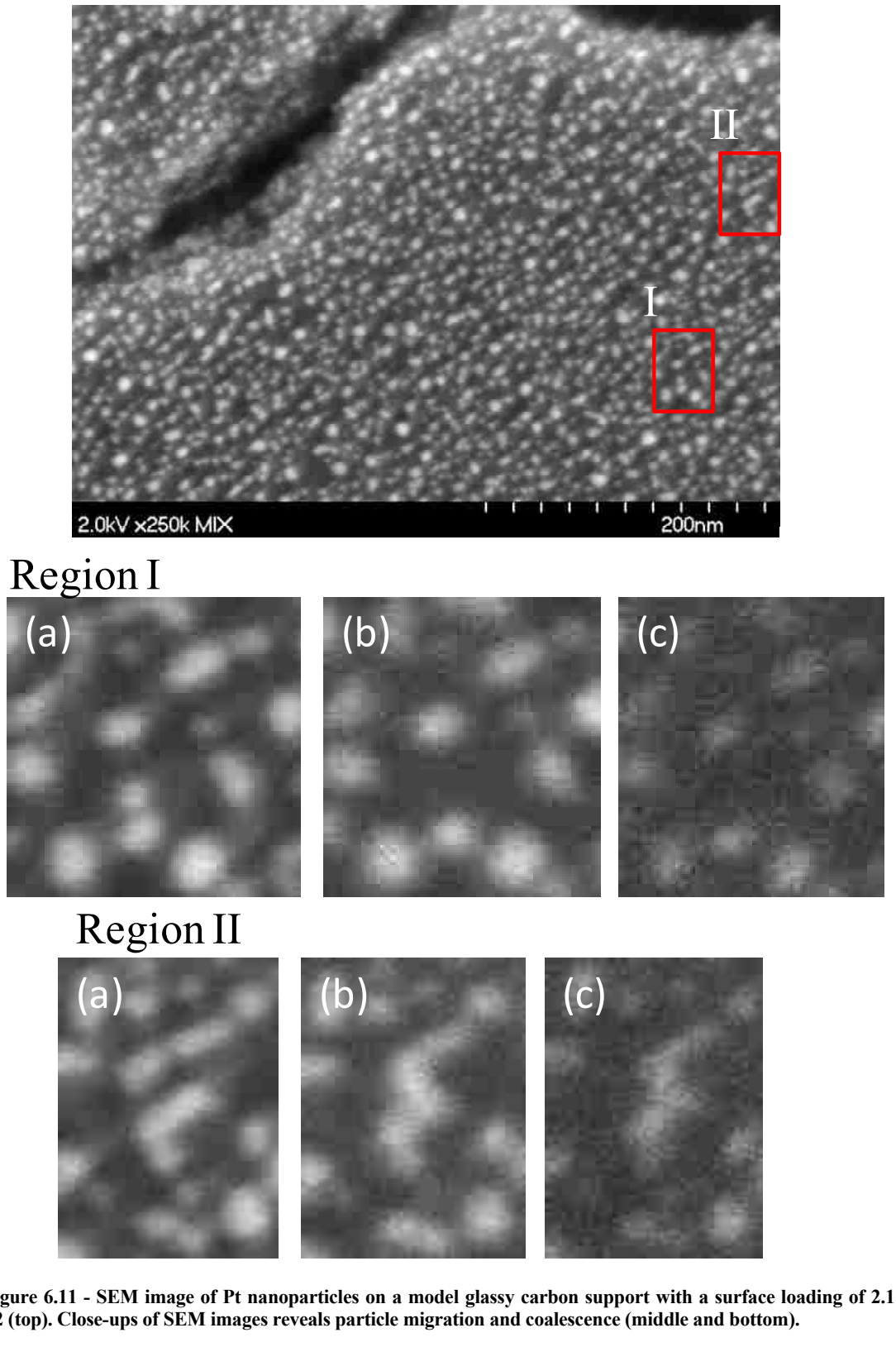

Figure 6.11 - SEM image of Pt nanoparticles on a model glassy carbon support with a surface loading of 2.1 µg/cm2 (top). Close-ups of SEM images reveals particle migration and coalescence (middle and bottom).

Closer examination of the SEM images reveal some migration and coalescence phenomena that occur from the 144 cycles to 280 cycles. These are highlighted in Figure 6.11. In *region I,* two particles present at 144 cycles in the center of the highlighted image become one after 280 cycles. In *region II,* a particle appears to attach itself to another by agglomeration. An elongated shape or *nanowire* begins to form instead of a larger spherical particle.

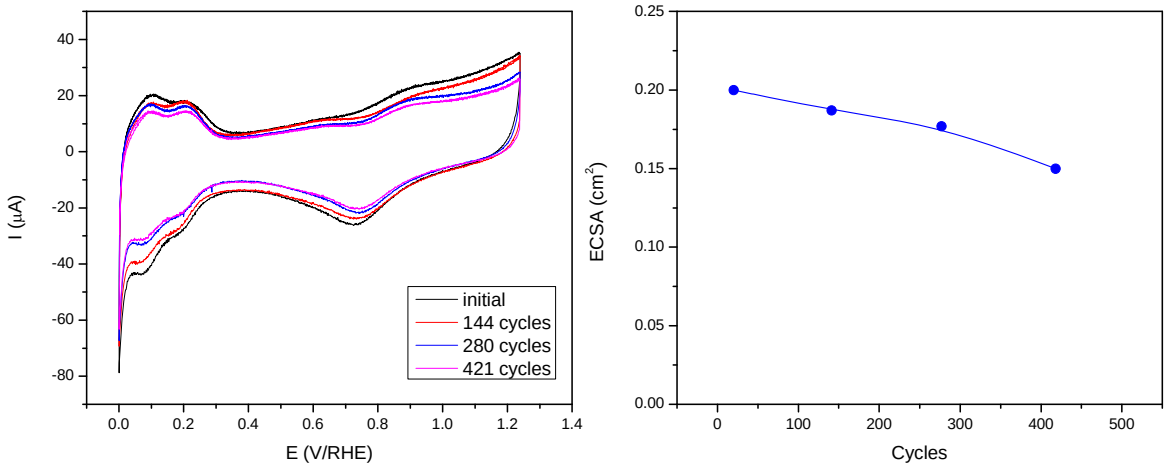

Figure 6.12 - Surface area loss noticeable in the CV and ESCA with potential cycling of 0.6 – 1.2 V_{RHE} at 50mV/s

The electrochemical active surface area ECSA was measured by CO stripping voltammetry initially and after every 140 cycles. The CVs taken at the end of each aging cycle reveal the loss of surface area through the decreasing peak size and reduced hydrogen adsorption/desorption area. The CVs and the CO stripping ECSA results are shown in Figure 6.12.

6.5 *Summary*

Model electrode structures have been developed that are active for the oxygen reduction reaction. It was shown that these electrodes could be transferred between the electrochemical cell and SEM imaging with no impact on the individual Pt nanoparticles. Control of the particle size was demonstrated by changing the quantity of platinum deposited. Loadings of 1 – 2.1 μg Pt per cm^2 of glassy carbon were studied and provide the desired particle sizes of around 3 nm. It was demonstrated that the particle size distribution could be further altered through annealing in ultra high vacuum.

The Gibbs-Thomson modification of the Nernst equation was shown to be a good prediction of the particle size effects on the electrochemical equilibrium potential. This was particular visible in the shift to lower potentials of the PtO reduction peak for small particles.

Initial aging studies demonstrate the usefulness of these model electrode structures for studying catalyst degradation. Degradation mechanisms of particle detachment were observed specifically when potential cycled in oxygen saturated electrolyte; Ostwald ripening and dissolution were observed through the use of particle size distributions; particle migration and coalescence was observed upon close examination of repeat SEM images taken of the same area.

Chapter 7

Nanoparticle Arrays

Up until this point all of the materials analyzed have contained a distribution of particle sizes. To confidently understand catalyst activity and degradation we need to separate particle size effects from other experimental variables. This demands a model electrode structure with catalytic particles of controlled size and spacing. A number of possible methods were considered to generate these nanostructured arrays. Nanosphere templating is an inexpensive bottoms up fabrication approach where a monolayer of nanospheres serves as the template mask for the metal deposition [90-92]. The result, after removal of the nanosphere template, is a 2D array of metal particles at the gaps between nanospheres. It was decided that the spacing between the particles, typically >200 nm was too large for these model electrode structures as it would create an extremely low loading. Direct write approaches using either laser lithography [93], e-beam lithography [94, 95] or directly scratching a polymer surface with an atomic force microscope (AFM) tip[96], have the necessary dimensional capabilities but require expensive equipment and are very time consuming to generate an array over an entire electrode surface.

The use of block copolymers is emerging as a promising and flexible technique with the size capability to be relevant to these studies [97-99]. Two approaches are considered with block copolymer templates, the first generates the metal particles in solution by precipitation in micelles followed by deposition of these colloidal particles onto the desired surface [100-103]. Application of this colloidal deposition approach to carbon supports has the additional challenge of removing all of the polymer from the metal particle. Traditional

removal methods such as heating in air or oxygen plasma would destroy the carbon support. If the polymer is not complete removed it would affect activity and degradation results. The second approach uses a spin coating of the block copolymer onto the support surface. This polymer self assembles into an ordered array that can be used as a template for nanoparticle fabrication by physical vapor deposition [104]. This method was selected for the development of our model electrode structures as it has the dimensional resolution and involves deposition of the metal directly onto the carbon support/

Here we introduce a method of fabricating simple geometric nanostructured particle arrays of controlled size and spacing by adapting a previously developed templating approach using the self-assembly of diblock copolymers composed of polystyrene (PS) and polymethylmethacrylate (PMMA) [105]. Under suitable processing conditions, the PS and PMMA microphases separate by self-assembly into a hexagonal lattice of PMMA cylinders in a matrix of PS with a lattice periodicity below photolithographic resolution limits [104].

7.1 *Block Copolymer Theory*

Block copolymers offer a unique method of controlling structure on the nanoscopic length scale. Diblock copolymers are macromolecules formed by joining two chemically distinct polymer blocks. Each block is a linear series of identical monomers. These blocks are thermodynamically incompatible, much like oil and vinegar, which develop into complex nanostructures as part of a free energy minimization [106]. The unique properties of block copolymer materials rely on their mesoscopic (10 nm scale) self-assembly in molten and solid states. These patterns, referred to as microphases, are driven by chemical incompatibilities between the different blocks that make up the block copolymer

molecules. In the simplest case of a diblock copolymer, minor chemical differences between the two blocks are sufficient to produce excess free energy contributions that are unfavorable to mixing. The microphase shapes depend on the relative polymer length of the two blocks.

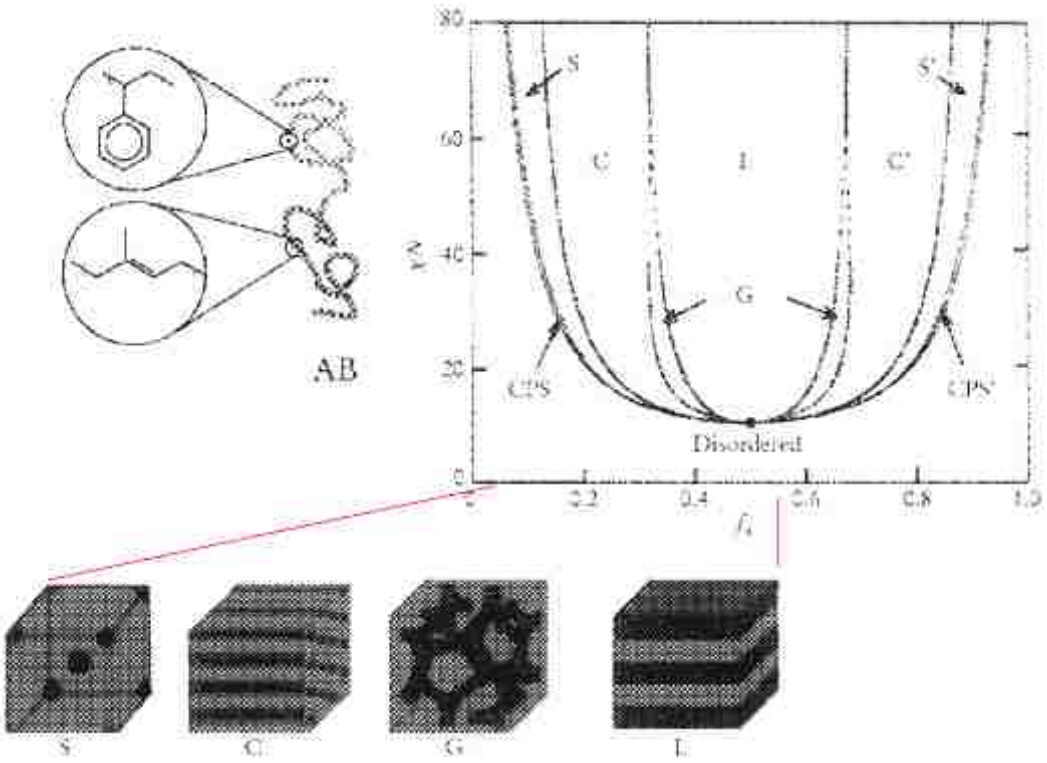

Figure 7.1 - Diblock copolymer phase diagram[106]

Our interest is in cylindrical shapes, which require a block fraction of ~0.3 according to Figure 7.1. At a smaller block fraction spherical shapes would be produced. At larger block fractions lamellar shapes would be created.

7.2 *Copolymer Template Process*

Block copolymer (BCP) thin films have shown excellent promise as templates for nanomanufacturing as they can self-assemble into structures with sub-30 nm length scales and can be integrated into existing manufacturing processes. Dense arrays of spots can be fabricated using cylinder-forming block copolymers with their domains oriented perpendicular to the substrate [107, 108]. Vertically oriented domain structures have distinct advantages in terms of pattern transfer to the underlying substrate and fabrication of high-aspect ratio features [109].

7.2.1 Control of Surface Interactions

Surface energies become significant in diblock copolymer thin films. Typically, one polymer block preferentially wets the substrate surface, which results in alternating sheets of each polymer parallel to the sample surface, a lamellar structure. The perpendicular alignment of block copolymer domains in thin films can be accomplished by several methods, but perhaps the most common means to induce perpendicular domain orientation is to chemically modify and control the interaction between the BCP and the substrate [110]. This control of the polymer-surface interactions can be accomplished with the application of a layer of statistically random copolymer brush or mat.

Random copolymer brushes or mats are widely used for chemical modification of the substrate to control the interfacial interactions or wetting behavior of the blocks of the copolymer and the substrate. Brushes are thin polymer layers in which each chain is chemically grafted to a surface and mats are thin cross-linked networks that may or may not be covalently attached to a surface. Both brushes and mats, when of sufficient

thickness, have the effect of modifying the chemical composition of a surface and controlling the interactions between an overlying material and the substrate.

A good description of a random brush formation is given by Mansky and coworkers. They demonstrated that the interfacial energies between the polystyrene PS and poly(methyl methacryltate) PMMA blocks of P(S-b- MMA) and the substrate can be carefully balanced by grafting an end-hydroxy functionalized P(S-r-MMA) polymer on the Si substrate [111]. In their work, solutions of the random copolymers in toluene (1% w/v) were spin coated onto silicon wafers, The polymer-coated substrates were then heated under vacuum at 140 °C, well above the glass transition temperature (T_g) of both PS and PMMA for a period of 2 days, to allow the terminal OH groups to diffuse to and react with the native oxide layer. After the samples were removed, unattached polymer chains were removed by rinsing with toluene. The thickness of the grafted layers was ~5 nm.

Random copolymer mats are required for applications where the surface does not contain enough hydroxyl groups to form brushes from hydroxyl condensation. Random copolymers with a cross-linking agent are thermally treated >200 °C to create a substrate independent insoluble thin film mat [107].

7.2.2 Polymer Template

The diblock copolymers studied in this work are composed of polystyrene (PS) and poly(methyl methacrylate) (PMMA) because of the familiarity and compatibility of these polymers within the semiconductor device community [112, 113]. We focused on a PS-PMMA copolymer with an average molecular of molecular weight Mn = 67,100 g/mol, polydispersity index of 1.09, and PMMA weight fraction of 30%. The P(S-b-MMA)

copolymers were purchased from Polymer Source, Inc. in Quebec, Canada. In the bulk, diblock copolymers of this molecular weight ratio spontaneously phase separate into a cylindrical morphology [114]. A copolymer with a molecular weight of 67,100 g/mol results in a mean pore diameter of 20 nm with a center to center spacing of 40 nm. Because the polymer template dimensions are determined by the diblock copolymer molecular weight, the size and spacing of the lattice can be varied by choosing either a lower molecular weight copolymer (for smaller features) or a higher molecular weight (for larger features). Examples of this pore control are shown in Figure 7.2.

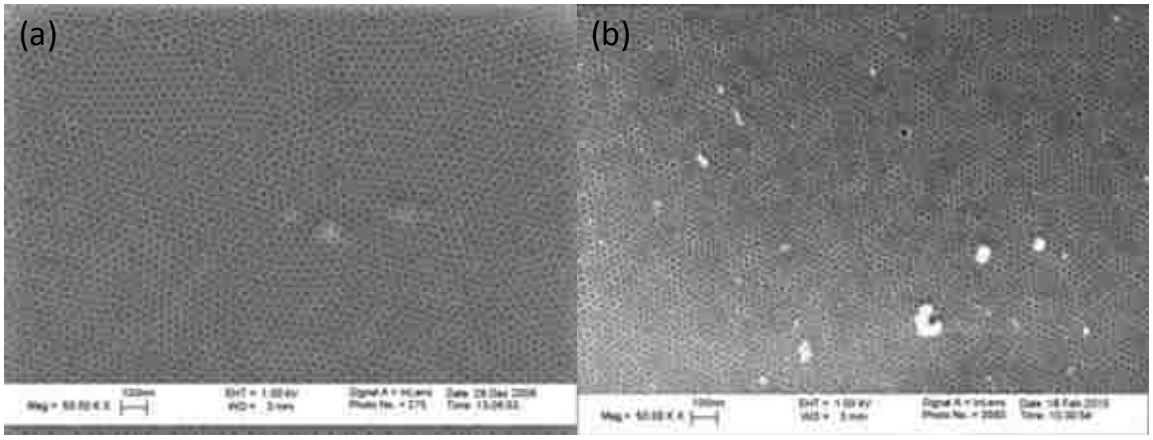

Figure 7.2 - SEM images of copolymer template (a) 20nm pores from a Mn = 67.1 kg/mol and (b) 10nm pores from a Mn=31.5 kg/mol P(S-b-MMA).

We followed the approach established by Guarini and Black by spin-casting the PS–PMMA diblock copolymer from a 1% wt solution of toluene in order to form ~40 nm-thick films on silicon substrates [104, 112-114]. Initially silicon substrates were used to develop the process before transferring the process to carbon substrates. The spun film thickness was previously shown to be critical for the proper ordering of the pores, For a 67.1 kg/mol polymer a film thickness of 35 – 40 nm was desired [105]. A Woollam variable angle

spectroscopic ellipsometer was used to measure the polymer film thickness with the polymer optical properties n=1.441 and k=0.135 at 530 nm. The films were then annealed for 24 hours at 165 °C (well above Tg ~ 105 °C) in vacuum to facilitate microphase separation of the two polymer blocks and provide polymer mobility. Because of the molecular weight ratio of our diblock copolymer (70:30 PS: PMMA), the resulting polymer films consist of 20 nm diameter PMMA cylinders spaced by 40 nm, in a matrix of PS. We removed the PMMA block from the annealed film by exposure to ultraviolet (UV) light ~1.2 J/cm^2, measured at a wavelengths 254 nm and immersion in glacial acetic acid (HOAc) for 5 min. The at wavelengths shorter than 260 nm, the exposure results in cleavage of the PMMA polymer backbone lowering the overall molecular weight allowing dissolution in glacial acetic acid (HOAc) [115]. The purity of the HOAc was found to be critical because a small amount of water does significantly slow down the PMMA removal. Aside from removing the PMMA block, we did not observe any side effects of the UV exposure and acetic acid on the remaining polystyrene film morphology.

7.2.3 Metal Particle Formation

Particle formation is accomplished by vapor deposition through this polymer template followed by lift-off. The process is shown schematically in Figure 7.3 along with an SEM image of the resulting template immediately after removal of the PMMA cores. Post treatments such as annealing at elevated temperatures result in spherical particles.

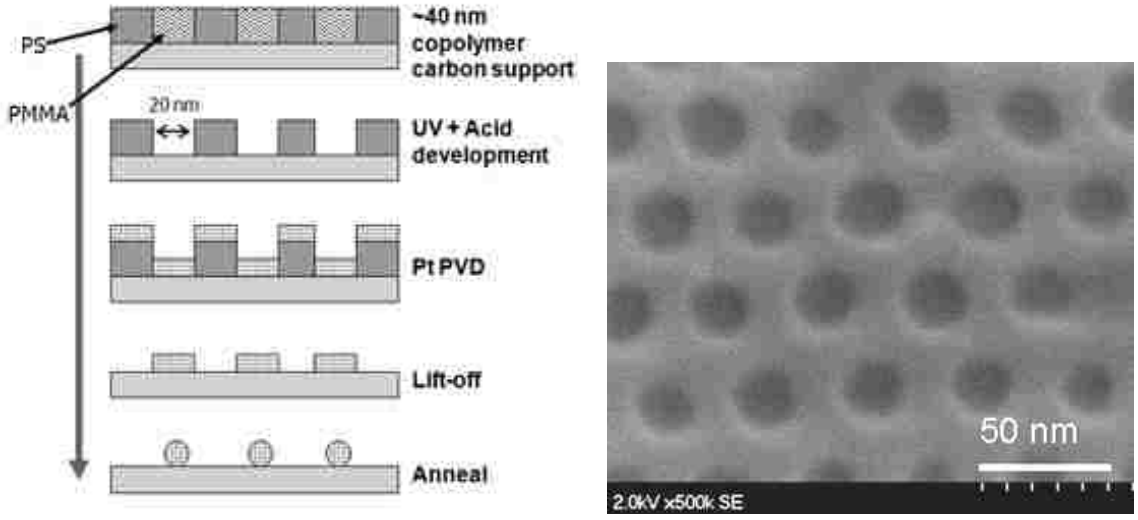

Figure 7.3. - Schematic of the Pt nanoparticle synthesis path using a block copolymer template and a SEM image of the polystyrene template

Immediately before deposition onto the polymer template the substrate was cleaned with an oxygen plasma, known plasma ashing. Plasma ashing parameters were selected to remove the random brush from the bottom of the pores but not remove the polymer template. A Branson barrel asher was used at 50W of RF power for 20 seconds to accomplish this pore clearing step which removed 5 - 10 nm of the overall polymer. The platinum deposition was conducted by e-beam evaporation at pressure of 10^{-7} torr, using 0.99999 purity Pt. The deposition was controlled by a quartz crystal microbalance calibrated for a slow deposition rate of 0.1 Å/s. The quantity or thickness of metal deposited was varied to control the particle size. The metal deposition creates a thin film in the bottom of the pore which through annealing will create a spherical particle. Since our pores are 20 nm in size, the required thickness for a desired particle diameter is $h=d^3/600$, where the particle diameter d is in nanometers. For example a desired particle of a 10 nm

diameter would require a film thickness of 1.67 nm. This relationship is schematically depicted in Figure 7.4.

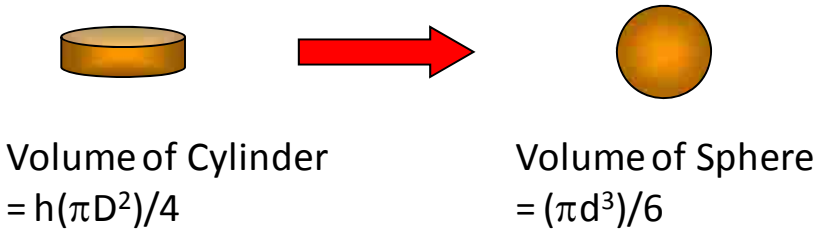

Figure 7.4 - Deposition thickness to particle size relation ship

After the metal deposition has been completed, the polymer template and all of the metal on top of it needed to be removed, through a process known as lift-off. Lift-off involves soaking the substrate in toluene for several minutes with the addition of some ultrasonics, followed by a final rinse with acetone and isopropyl alcohol. SEM images taken partial through the lift-off process are shown in Figure 7.5. The polymer template is visible in both the secondary electron and backscatter electron images. However, the thin platinum metal layer, which is only 2 monolayers thick, is only visible with secondary electrons, which highlight Z contrast.

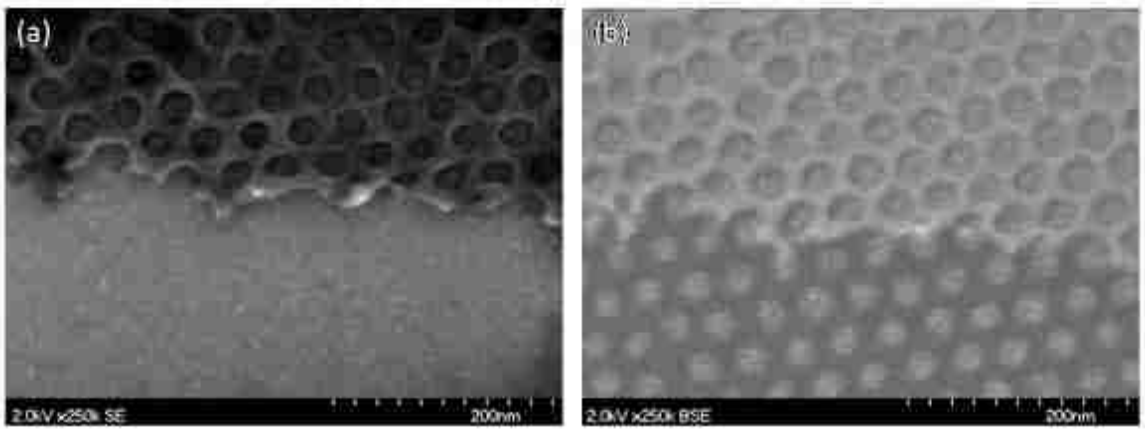

Figure 7.5 – Pt lift-off process (a) secondary electron (SE) image and (b) backscatter electron (BSE) image

7.3 *Pt Nanoparticle Arrays Results*

The block copolymer poly(styrene-b-methyl methacrylate) utilized in this study had a molecular weight of 67.1 kg/mol (46.1-b-21.0) which results in a pore size of 20 nm. The deposited film creates a cylinder at the bottom of the template pore. The resulting particle arrays created by this process are shown in Figure 7.6. All images are of Pt arrays after heating to 700 °C in ultra-high vacuum at with a ramp rate of 30 °C/min and then held for 30 seconds. The results are arrays of spherical particles with the final diameters determined by the deposited Pt thickness demonstrating the control over particle size. The amount of deposited platinum in Figure 7.6 was 4.57 nm(9.8 $\mu g/cm^2$) for (a,d), 1.67 nm (3.6 $\mu g/cm^2$) for (b,e) and 0.57 nm (1.2 $\mu g/cm^2$) for (c,f) which were selected to yield particle diameters of 14, 10 and 7 nm repectively. As can be seen if figures (d) and (e) the desired particle size is in very good agreement with the actual size. However, as can be seen Figure 7.6(c) when the deposited film is too thin it did not form a single particle of the desired size, but instead formed multiple smaller particles. Still some of the desired single 7 nm particles can be seen in the image. This represents a minimum film loading required to generate s single particle. At a pore loading of 1.3 $\mu g/cm^2$ (0.57 nm) the film is only ~ 2 monolayers thick. A film this thin is not continuous and lacks the surface tension required to form a single particle upon heating. Pt particle arrays with these mixed sizes are not desired for studies of the degradation process because the size effect would be convoluted.

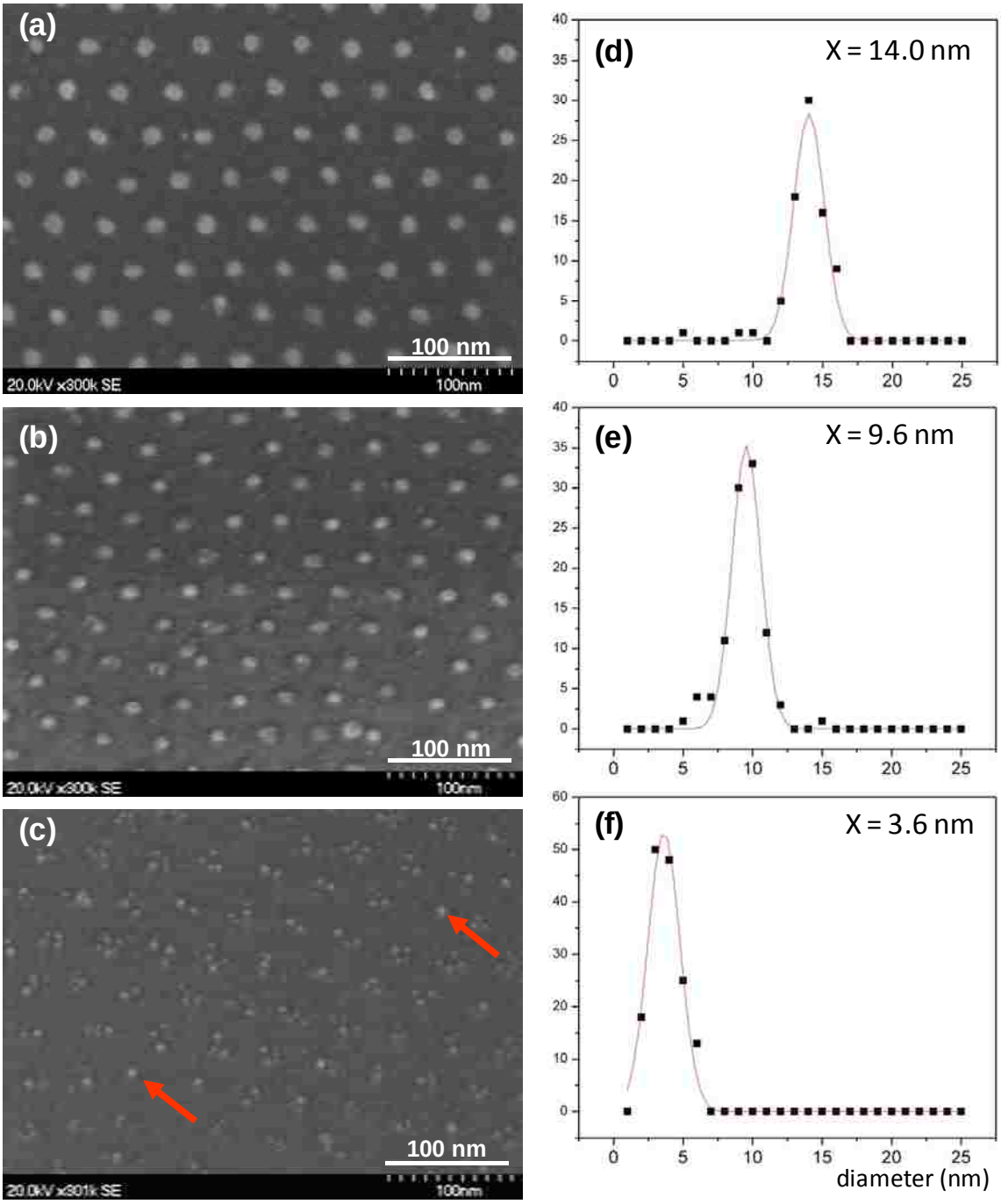

Figure 7.6 - Particle size control (a-c) SEM images of 9.8, 3.6, 1.2 µg/cm2 pore loadings (d-f) corresponding PSDs

7.4 *Nanoparticle Arrays on Glassy Carbon*

The ultimate goal of this polymer template process development was to generate a nanoparticle array on a glassy carbon electrode for electrochemical rotating disk electrode (RDE) experiments. The electrode tips for the Pine Instruments RDE are 5 mm in diameter. Spinning a uniform film of polymer with controlled thickness onto a 5 mm diameter electrode proved to be nearly impossible. The approach we took was to generate a larger wafer of glassy carbon and then cut the electrodes from it after the polymer template was in place. To generate a glassy carbon wafer, glassy carbon plates, 50 mm square, with a thickness of 4 mm were purchased from SPI Supplies®. These plates were machined into wafers ~ 50 mm in diameter which could now be spun for the standard application of the copolymer in a toluene solution.

After some effort trying to get a random brush layer to form on the glassy carbon, it was decided to seek some very experienced help. We sent these thick glassy carbon wafers to Professor Nealey's group at the University of Wisconsin for application of a cross-linked random polymer mat and spin coating of a 67.1 kg/mol P(S-b-MMA) copolymer. The carbon wafers were vacuum annealed and returned for further processing. We cut 5 mm diameter glassy carbon electrodes from these wafers using micro-wire electrical discharge machining EDM. Machining by wire EDM involves a rapidly recurring current discharge between a moving wire and the part being machined. The 50 micron tungsten wire is constantly being refreshed and the machining of the work piece, our carbon wafer in this case, is accomplish by gradual erosion from the discharge. The EDM process is conducted in a dielectric liquid and a screen was installed in the fluid tank to capture our 5 mm diameter electrodes as they floated free from the wafer. A photograph of the AGIE wire

EDM system used is shown in Figure 7.7 along with a schematic of the electrode cutting process. No damage was observed in the polymer surface after this machining process. The polymer film was present all the way to the edge of the cut electrode. Electrodes were cut from the middle of the wafer, avoiding the outer 10 mm to insure good film thickness uniformity.

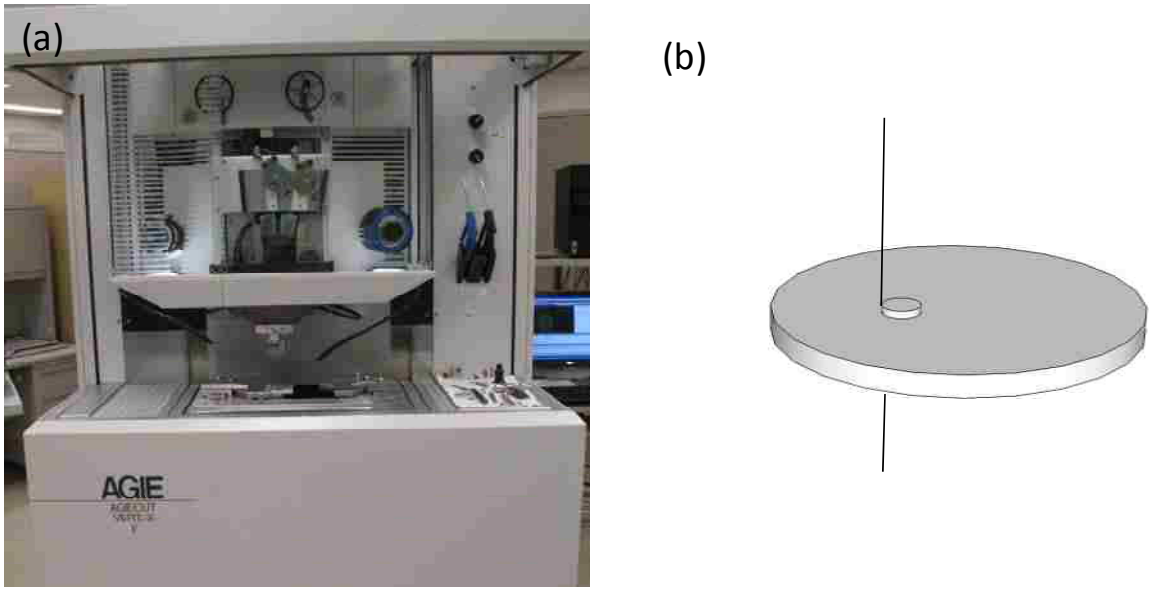

Figure 7.7 - µ-wire EDM cutting of glassy carbon electrodes (a) AGIE system and (b) wafer schematic

The 5 mm electrodes were further processed by exposure to 1.2 J/cm^2 of UV light and a develop time of 5 minutes in HOAc. The cross-linked random mat between the ordered block copolymer and the glassy carbon surface required more plasma ashing to remove than the brush copolymers used on the silicon wafers during the process development. The ashing time was increased to 60 seconds, while the power was kept at 50 watts. For these samples 1.7 nm film (3.6 µg/cm^2) of Pt was deposited by e-beam evaporation to form 10 nm diameter particles. The lift-off process also proved more difficult with the cross-linked

random copolymer mats as the cross-linked template was not soluble in toluene. Hot n-methly-2-pyrrolidone (NMP) was found to be a suitable solvent for remove the random mat layer. The coated electrodes were soaked in 100°C NMP for 1 hour to lift-off the polymer and unwanted metal. This was followed by sequential rinse of acetone and isopropyl alcohol rinse. After the lift-off was verified, the electrode was heated to 700°C for 30 seconds in ultrahigh vacuum. The results of these process steps on the glassy carbon electrode are shown in Figure 7.8.

Figure 7.8 - Glassy carbon array (a) after 1.7 nm Pt deposition, (b) after lift-off and (c) after 700°C anneal

The electrodes were pressed into a Pine Instruments removable electrode Teflon holder and mounted on the RDE shaft. Electrical contact is made to back side by a gold plated, spring loaded pin which is threaded into the RDE shaft. The sample was lowered into an argon purged 0.1 M $HClO_4$ electrolyte. Initial sweeps of 0 – 1.4 V_{RHE} at a scan rate of 500 mV/s were conducted for 40 cycles to clean and activate the surface. The electrode was removed for SEM imaging. As can be seen in Figure 7.9, some of the ordered array is missing and the appearance of particle agglomerates can be seen. The detachment of whole particles was by far the governing process detected under harsh potential cycling conditions (0 – 1.4V_{RHE}).

Figure 7.9 - Pt nanoparticle arrays after initial conditioning, particle movement visible

Figure 7.10 - Particle agglomeration from detachment/reattachment

In many cases the agglomeration does not directly coincide with missing particles from the array, indicating that detachment not surface migration was the predominant mechanism.

7.5 *Summary*

We have developed a process by which catalytic metal nanoparticles of controlled size and spacing can be fabricated directly on RDE electrode surfaces. The catalytic metal is vapor deposited from high purity material directly on the support surface. In order for the metal film to form a single particle of the desired shape the deposition thickness must be > 2 ML. Cross-linked mats of random copolymers required additional cleaning steps to remove as compared to their random brush counterparts. This resulted in longer plasma ashing times before vapor deposition and lift-off in hot NMP.

The detachment of whole particles was by far the governing process detected under the harsh potential cycling conditions (0 –1.4V_{RHE}) used for the initial conditioning.

Chapter 8

Conclusions

The purpose of this research was the development of model electrode structures for studies to clarify the degradation mechanisms and dissolution reaction of the Pt catalyst in acid medium. The ultimate goal would be the reduction of the electrocatalyst degradation through a better understanding of the degradation mechanisms. The developed processes would be very useful for any catalyst studies where a well defined surface, particle size and particle separation are important to clarify particle reactivity and degradation mechanisms.

Three model electrode structures were developed for this purpose; one on quartz crystals for use in electrochemical quartz crystal microbalance; one with Pt nanoparticles of with controlled nanoparticle size distributions directly on glassy carbon electrodes and finally one with ordered arrays of platinum nanoparticles with control over particle size and particle spacing on glassy carbon electrodes.

Using the electrochemical quartz crystal microbalance (EQCM) it was shown that cycling parameters, such as scan rates and upper voltage limit, have an impact on the rate of decay in platinum electrochemical area ECSA. While dissolution was observed during potentiostatic testing, potential cycling significantly enhanced the dissolution rate of Pt. The electro-oxidation of platinum involved the initial deposition of OH as an intermediate surface layer for ~1/4 ML. The oxidation process proceeds with the formation of PtO up to half a monolayer of O that resides on-top of the Pt surface without any place exchange. The process continues with the formation of PtO above 1/2 ML but with the growth of a multilayer through place exchange between O adatoms and the top most Pt surface atoms.

This place exchange occurs at potentials of 1.1 V_{RHE} and above. The interfacial place exchange leads to the development of a multi-layer surface lattice comprising Pt^{2+} cations and O^{2-} anions. Upon reduction, this multilayer leads to an enhanced rate of platinum dissolution. The impact is that testing protocols involving the formation of a multilayer oxide combined with potential cycling result in the highest rate of platinum dissolution.

Model electrode structures developed by direct evaporation on glassy carbon electrodes were shown to be active for the oxygen reduction reaction. It was shown that these electrodes could be transferred between the electrochemical cell and SEM imaging with no impact on the individual Pt nanoparticles. Control of the particle size was demonstrated by changing the quantity of platinum deposited. Loadings of 1 – 2.1 μg Pt per cm^2 of glassy carbon were studied and provide the desired particle sizes of around 3 nm and could be further altered through annealing in ultra high vacuum.

We improved upon platinum nanoparticle glassy carbon electrodes by developing a process by which catalytic metal nanoparticles of controlled size and spacing can be fabricated directly on RDE electrode surfaces. The catalytic metal is vapor deposited from high purity material directly on the support surface. In order for the metal film to form a single particle of the desired shape the deposition thickness must be > 2 ML.

Initial aging studies demonstrate the usefulness of these model electrode structures for studying catalyst degradation. Degradation mechanisms of particle detachment were observed specifically under the harsh potential cycling conditions (0 – 1.4V_{RHE}) used for the initial conditioning and when potential cycled in oxygen saturated electrolyte. Ostwald ripening and dissolution were observed through the use of particle size distributions;

particle migration and coalescence was observed upon close examination of repeat SEM images taken of the same area.

Pt nanoparticle sintering on many of these surfaces was observed to proceed through the formation of Pt nanowires. The nanowire formation was mostly likely from particle agglomeration, followed by a slow ripening process. The nanowire formation occurred when the initial particle distribution contained very small ~1.8 nm particles which are closely spaced. The nanowire formation was also observed on the sputtered carbon surface, which perhaps had enhanced carbon corrosion due to the low amount of graphitic bonding.

Through the use of block copolymer templates on glassy carbon electrodes combined with high resolution scanning electron microscopy, we have demonstrated the *"better model system for real electrocatalyst"* that Markovic and Ross suggested in 2002 [48].

Chapter 9

References

1. Grove, W.R., *Xxiv. On Voltaic Series and the Combination of Gases by Platinum.* Philosophical Magazine Series 3. **14**(86): p. 127 - 130.
2. Carrette, L., K.A. Friedrich, and U. Stimming, *Fuel Cells: Principles, Types, Fuels, and Applications.* Chemphyschem, 2000. **1**(4): p. 162-193.
3. DOE-EERE. *Http://Www1.Eere.Energy.Gov/Hydrogenandfuelcells/Fuelcells/Fc_Challenges.Html*. [cited.
4. Markovic, N.M.P.N.R. and P.N. Ross, *New Electrocatalysts for Fuel Cells from Model Surfaces to Commercial Catalysts.* CATTECH, 2000. **4**(2): p. 110-126.
5. *Fuel Cell Handbook.* Seventh ed. 2004: U.S. Department of Energy.
6. Borup, R., et al., *Scientific Aspects of Polymer Electrolyte Fuel Cell Durability and Degradation.* Chemical Reviews, 2007. **107**(10): p. 3904-3951.
7. Shao-Horn, Y., et al., *Instability of Supported Platinum Nanoparticles in Low-Temperature Fuel Cells.* Topics in Catalysis, 2007. **46**(3-4): p. 285-305.
8. Carrette, L., K.A. Friedrich, and U. Stimming, *Fuel Cells - Fundamentals and Applications.* Fuel Cells, 2001. **1**(1): p. 5-39.
9. Mayrhofer, K.J.J., et al., *Fuel Cell Catalyst Degradation on the Nanoscale.* Electrochemistry Communications, 2008. **10**(8): p. 1144-1147.
10. Gasteiger, H.A., et al., *Activity Benchmarks and Requirements for Pt, Pt-Alloy, and Non-Pt Oxygen Reduction Catalysts for Pemfcs.* Applied Catalysis B-Environmental, 2005. **56**(1-2): p. 9-35.
11. Larminie, J. and A. Dicks, *Fuel Cell Systems Explained*. 2003: John Wiley & Sons, Chichester, England.
12. Schmittinger, W. and A. Vahidi, *A Review of the Main Parameters Influencing Long-Term Performance and Durability of Pem Fuel Cells.* Journal of Power Sources, 2008. **180**(1): p. 1-14.
13. Sethuraman, V.A., et al., *Durability of Perfluorosulfonic Acid and Hydrocarbon Membranes: Effect of Humidity and Temperature.* Journal of the Electrochemical Society, 2008. **155**(2): p. B119-B124.
14. Borup, R.L., et al., *Pem Fuel Cell Electrocatalyst Durability Measurements.* Journal of Power Sources, 2006. **163**(1, SI): p. 76-81.
15. Mitsushima, S., et al., *Consumption Rate of Pt under Potential Cycling.* Journal of the Electrochemical Society, 2007. **154**(2): p. B153-B158.
16. Franco, A.A. and M. Gerard, *Multiscale Model of Carbon Corrosion in a Pefc: Coupling with Electrocatalysis and Impact on Performance Degradation.* Journal of the Electrochemical Society, 2008. **155**(4): p. B367-B384.
17. Wood, D., et al., *Pemfc Component Characterization and Its Relationship to Mass-Transport Overpotentials During Long-Term Testing.* ECS Transactions, 2006. **3**(1): p. 753-763.

18. Zhang, S., et al., *A Review of Platinum-Based Catalyst Layer Degradation in Proton Exchange Membrane Fuel Cells.* Journal of Power Sources, 2009. **194**(2): p. 588-600.
19. Sasaki, K., M. Shao, and R. Adzic, *Dissolution and Stabilization of Platinum in Oxygen Cathodes*, in *Polymer Electrolyte Fuel Cell Durability*. 2009. p. 7-27.
20. Wu, J., et al., *A Review of Pem Fuel Cell Durability: Degradation Mechanisms and Mitigation Strategies.* Journal of Power Sources, 2008. **184**(1): p. 104-119.
21. Lifshitz, I.M. and V.V. Slyozov, *The Kinetics of Precipitation from Supersaturated Solid Solutions.* Journal of Physics and Chemistry of Solids, 1961. **19**(1-2): p. 35-50.
22. Meyers, J.P. and R.M. Darling, *Model of Carbon Corrosion in Pem Fuel Cells.* Journal of the Electrochemical Society, 2006. **153**(8): p. A1432-A1442.
23. Yu, X. and S. Ye, *Recent Advances in Activity and Durability Enhancement of Pt/C Catalytic Cathode in Pemfc: Part Ii: Degradation Mechanism and Durability Enhancement of Carbon Supported Platinum Catalyst.* Journal of Power Sources, 2007. **172**(1): p. 145-154.
24. Darling, R.M. and J.P. Meyers, *Kinetic Model of Platinum Dissolution in Pemfcs.* Journal of the Electrochemical Society, 2003. **150**(11): p. A1523-7.
25. Bett, J.A.S., K. Kinoshita, and P. Stonehart, *Crystallite Growth of Platinum Dispersed on Graphitized Carbon-Black. (Part 2. Effect of Liquid Environment)* Journal of Catalysis, 1976. **41**(1): p. 124-133.
26. Gruver, G.A., R.F. Pascoe, and H.R. Kunz, *Surface-Area Loss of Platinum Supported on Carbon in Phosphoric-Acid Electrolyte.* Journal of the Electrochemical Society, 1980. **127**(6): p. 1219-1224.
27. Granqvist, C.G. and R.A. Buhrman, *Ultrafine Metal Particles.* Journal of Applied Physics, 1976. **47**(5): p. 2200-2219.
28. Ruckenstein, E. and B. Pulvermacher, *Growth Kinetics and the Size Distributions of Supported Metal Crystallites.* Journal of Catalysis, 1973. **29**(2): p. 224-245.
29. Blurton, K.F., H.R. Kunz, and D.R. Rutt, *Surface Area Loss of Platinum Supported on Graphite.* Electrochimica Acta, 1978. **23**(3): p. 183-190.
30. Wilson, M.S., et al., *Surface-Area Loss of Supported Platinum in Polymer Electrolyte Fuel-Cells.* Journal of the Electrochemical Society, 1993. **140**(10): p. 2872-2877.
31. Bonakdarpour, A., et al., *Studies of Transition Metal Dissolution from Combinatorially Sputtered, Nanostructured Pt1-Xmx (M = Fe, Ni; 0 < X < 1) Electrocatalysts for Pem Fuel Cells.* Journal of the Electrochemical Society, 2005. **152**(1): p. A61-A72.
32. Kinoshita, K., *Carbon: Electrochemical and Physicohemical Properties*. 1988: John Wiley & Sons, Inc.
33. Reiser, C.A., et al., *A Reverse-Current Decay Mechanism for Fuel Cells.* Electrochemical and Solid State Letters, 2005. **8**(6): p. A273-A276.
34. Roen, L.M., C.H. Paik, and T.D. Jarvic, *Electrocatalytic Corrosion of Carbon Support in Pemfc Cathodes.* Electrochemical and Solid State Letters, 2004. **7**(1): p. A19-A22.
35. Stevens, D.A., et al., *Ex Situ and in Situ Stability Studies of Pemfc Catalysts.* Journal of the Electrochemical Society, 2005. **152**(12): p. A2309-A2315.

36. Yasuda, K., et al., *Characteristics of a Platinum Black Catalyst Layer with Regard to Platinum Dissolution Phenomena in a Membrane Electrode Assembly.* Journal of the Electrochemical Society, 2006. **153**(8): p. A1599-A1603.
37. Yasuda, K., et al., *Platinum Dissolution and Deposition in the Polymer Electrolyte Membrane of a Pem Fuel Cell as Studied by Potential Cycling.* Physical Chemistry Chemical Physics, 2006. **8**(6): p. 746-752.
38. Pourbaix, M., *Atlas of Electrochemical Equilibria in Aqueous Solutions*. 1966: Pergamon, New York.
39. Tang, L., et al., *Electrochemical Stability of Nanometer-Scale Pt Particles in Acidic Environments.* Journal of the American Chemical Society, 2009. **132**(2): p. 596-600.
40. Allen, B.C., *The Surface Tension of Liquid Transition Metals at Their Melting Points.* Transactions of the Metallurgical Society of AIME, 1963. **227**: p. 1175-1183.
41. Galeev, T.K., et al., *Surface-Properties of Platinum and Palladium.* Reaction Kinetics and Catalysis Letters, 1980. **14**(1): p. 61-65.
42. Virkar, A.V. and Y. Zhou, *Mechanism of Catalyst Degradation in Proton Exchange Membrane Fuel Cells.* Journal of the Electrochemical Society, 2007. **154**(6): p. B540-B547.
43. Xie, J., et al., *Microstructural Changes of Membrane Electrode Assemblies During Pefc Durability Testing at High Humidity Conditions.* Journal of the Electrochemical Society, 2005. **152**(5): p. A1011-A1020.
44. Colon-Mercado, H.R. and B.N. Popov, *Stability of Platinum Based Alloy Cathode Catalysts in Pem Fuel Cells.* Journal of Power Sources, 2006. **155**(2): p. 253-263.
45. Chung, C.G., et al., *Degradation Mechanism of Electrocatalyst During Long-Term Operation of Pemfc.* International Journal of Hydrogen Energy, 2009. **34**(21): p. 8974-8981.
46. Ferreira, P.J., et al., *Instability of Pt/C Electrocatalysts in Proton Exchange Membrane Fuel Cells.* Journal of the Electrochemical Society, 2005. **152**(11): p. A2256-71.
47. Cherstiouk, O.V., P.A. Simonov, and E.R. Savinova, *Model Approach to Evaluate Particle Size Effects in Electrocatalysis: Preparation and Properties of Pt Nanoparticles Supported on Gc and Hopg.* Electrochimica Acta, 2003. **48**: p. 3851-3860.
48. Markovic, N.M. and P.N. Ross, *Surface Science Studies of Model Fuel Cell Electrocatalysts.* Surface Science Reports, 2002. **45**(4-6): p. 117-229.
49. Kounaves, S.P., *Chapter 37 - Voltammetric Techniques*, in *Handbood of Instrumental Techniques for Analytical Chemistry*, Prentice Hall.
50. Bard, A.J., Faulkner, L. R., *Electrochemical Methods: Fundamentals and Applications*. 2nd ed. 2001: John Wiley & Sons, Inc.
51. Umeda, M., et al., *Cathode Platinum Degradation in Membrane Electrode Assembly Studied Using a Solid-State Electrochemical Cell.* Journal of Physical Chemistry C, 2008. **112**(46): p. 18098-18103.
52. Sugawara, Y., et al., *Eqcm Study on Dissolution of Ruthenium in Sulfuric Acid.* Journal of the Electrochemical Society, 2008. **155**(9): p. B897-B902.

53. Salgado, L., et al., *Cyclic Voltammetry and Electrochemical Quartz Crystal Microbalance Studies of a Rhodized Platinum Electrode in Sulfuric Acid Solution.* Journal of Solid State Electrochemistry, 2006. **10**(4): p. 230-235.
54. Chatenet, M., et al., *Understanding Co-Stripping Mechanism from Niupd/Pt(1 1 0) in View of the Measured Nickel Formal Partial Charge Number Upon Underpotential Deposition on Platinum Surfaces in Sulphate Media.* Electrochimica Acta, 2007. **53**(2): p. 369-376.
55. Umeda, M., et al., *Pt Degradation Mechanism in Concentrated Sulfuric Acid Studied Using Rotating Ringâ¯'Disk Electrode and Electrochemical Quartz Crystal Microbalance.* The Journal of Physical Chemistry C, 2009. **113**(35): p. 15707-15713.
56. Sauerbrey, G., *Verwendung Von Schwingquarzen Zur Wägung Dünner Schichten Und Zur Mikrowägung.* Zeitschrift für Physik A Hadrons and Nuclei, 1959. **155**(2): p. 206-222.
57. Glassford, A.P.M., *Response of a Quartz Crystal Microbalance to a Liquid Deposit.* Journal of Vacuum Science and Technology, 1978. **15**(6): p. 1836-1843.
58. Kanazawa, K.K. and J.G. Gordon, *Frequency of a Quartz Microbalance in Contact with Liquid.* Analytical Chemistry, 1985. **57**(8): p. 1770-1771.
59. Koper, M.T.M., *Introductory Lectureelectrocatalysis: Theory and Experiment at the Interface.* Faraday Discussions, 2009. **140**: p. 11-24.
60. Alsabet, M., M. Grden, and G. Jerkiewicz, *Comprehensive Study of the Growth of Thin Oxide Layers on Pt Electrodes under Well-Defined Temperature, Potential, and Time Conditions.* Journal of Electroanalytical Chemistry, 2006. **589**(1): p. 120-127.
61. Harrington, D.A., *Simulation of Anodic Pt Oxide Growth.* Journal of Electroanalytical Chemistry, 1997. **420**(1-2): p. 101-109.
62. Pourbaix, M.J.N., J. Van Muylder, and N. de Zoubov, *Electrochemical Properties of Platinum Metals.* Platinum Metals Review, 1959. **3**(2-3): p. Various pages.
63. Mendez, A., et al., *Eqcm Study of the Adsorption/Desorption Processes of Polyethyleneglycol with Molecular Weight 20,000 on Pt in Perchloric Acid Solution.* International Journal of Electrochemical Science, 2008. **3**(8): p. 918-934.
64. Snook, G.A., A.M. Bond, and S. Fletcher, *The Use of Massograms and Voltammograms for Distinguishing Five Basic Combinations of Charge Transfer and Mass Transfer at Electrode Surfaces.* Journal of Electroanalytical Chemistry, 2002. **526**(1-2): p. 1-9.
65. Bahena, E., et al., *An Eqcm Study of Polyethyleneglycol 8000 Adsorption and Its Coadsorption with Cl- Ions on Pt in Perchloric Acid Solutions.* Electrochimica Acta, 2004. **49**(6): p. 989-997.
66. Karlberg, G.S., et al., *Cyclic Voltammograms for H on Pt(111) and Pt(100) from First Principles.* Physical Review Letters, 2007. **99**(12): p. 4.
67. Birss, V.I., M. Chang, and J. Segal, *Platinum Oxide Film Formation--Reduction: An in-Situ Mass Measurement Study.* Journal of Electroanalytical Chemistry, 1993. **355**(1-2): p. 181-191.
68. Conway, B.E. and D.M. Novak, *Hysteresis in Formation and Reduction of Submonolayer Quantities of Surface Oxide at Pt in an Almost Anhydrous Solvent.* Journal of the Electrochemical Society, 1981. **128**(5): p. 956-962.

69. Vassiliev, Y.B., V.S. Bagotzky, and V.A. Gromyko, *Kinetics and Mechanism of the Formation and Reduction of Oxide Layers on Platinum Part I. Oxidation and Reduction of Platinum Electrodes.* Journal of Electroanalytical Chemistry, 1984. **178**(2): p. 247-269.
70. Vassiliev, Y.B., V.S. Bagotzky, and O.A. Khazova, *Kinetics and Mechanism of Formation and Reduction of Oxide Layers on Platinum : Part Ii. Oxygen Adsorption and Absorption Mechanism at High Positive Potentials.* Journal of Electroanalytical Chemistry, 1984. **181**(1-2): p. 219-233.
71. Conway, B.E., *Electrochemical Oxide Film Formation at Noble Metals as a Surface-Chemical Process.* Progress in Surface Science, 1995. **49**(4): p. 331-452.
72. Conway, B.E. and G. Jerkiewicz, *Surface Orientation Dependence of Oxide Film Growth at Platinum Single Crystals.* Journal of Electroanalytical Chemistry, 1992. **339**(1-2): p. 123-146.
73. Hansen, H.A., J. Rossmeisl, and J.K. Norskov, *Surface Pourbaix Diagrams and Oxygen Reduction Activity of Pt, Ag and Ni(111) Surfaces Studied by Dft.* Physical Chemistry Chemical Physics, 2008. **10**(25): p. 3722-3730.
74. Angerstein-Kozlowska, H., B.E. Conway, and W.B.A. Sharp, *The Real Condition of Electrochemically Oxidized Platinum Surfaces: Part I. Resolution of Component Processes.* Journal of Electroanalytical Chemistry, 1973. **43**(1): p. 9-36.
75. Zolfaghari, A., B.E. Conway, and G. Jerkiewicz, *Elucidation of the Effects of Competitive Adsorption of Cl-and Br- Ions on the Initial Stages of Pt Surface Oxidation by Means of Electrochemical Nanogravimetry.* Electrochimica Acta, 2002. **47**(8): p. 1173-1187.
76. Jerkiewicz, G., et al., *Surface-Oxide Growth at Platinum Electrodes in Aqueous H2so4: Reexamination of Its Mechanism through Combined Cyclic-Voltammetry, Electrochemical Quartz-Crystal Nanobalance, and Auger Electron Spectroscopy Measurements.* Electrochimica Acta, 2004. **49**(9-10): p. 1451-1459.
77. Conway, B.E., G. Tremiliosi-Filho, and G. Jerkiewicz, *Independence of Formation and Reduction of Monolayer Surface Oxide on Pt from Presence of Thicker Phase-Oxide Layers.* Journal of Electroanalytical Chemistry, 1991. **297**(2): p. 435-443.
78. Bindra, P., S.J. Clouser, and E. Yeager, *Platinum Dissolution in Concentrated Phosphoric-Acid.* Journal of the Electrochemical Society, 1979. **126**(9): p. 1631-1632.
79. Darling, R.M. and J.P. Meyers, *Mathematical Model of Platinum Movement in Pem Fuel Cells.* Journal of the Electrochemical Society, 2005. **152**(1): p. A242-A247.
80. Paik, C.H., G.S. Saloka, and G.W. Graham, *Influence of Cyclic Operation on Pem Fuel Cell Catalyst Stability.* Electrochemical and Solid State Letters, 2007. **10**(2): p. B39-B42.
81. Wang, X., R. Kumar, and D.J. Myers, *Effect of Voltage on Platinum Dissolution.* Electrochemical and Solid-State Letters, 2006. **9**(5): p. A225-A227.
82. Rand, D.A.J. and R. Woods, *A Study of the Dissolution of Platinum, Palladium, Rhodium and Gold Electrodes in 1 M Sulphuric Acid by Cyclic Voltammetry.* Journal of Electroanalytical Chemistry, 1972. **35**(1): p. 209-218.
83. Johnson, D.C., D.T. Napp, and S. Bruckenstein, *A Ring-Disk Electrode Study of the Current/Potential Behaviour of Platinum in 1.0 M Sulphuric and 0.1 M Perchloric Acids.* Electrochimica Acta, 1970. **15**(9): p. 1493-1509.

84. Ofstad, A.B., et al., *Assessment of Platinum Dissolution from a Pt/C Fuel Cell Catalyst: An Electrochemical Quartz Crystal Microbalance Study.* Journal of the Electrochemical Society, 2010. **157**(5): p. B621-B627.
85. Dam, V.A.T. and F.A. de Bruijn, *The Stability of Pemfc Electrodes - Platinum Dissolution Vs Potential and Temperature Investigated by Quartz Crystal Microbalance.* Journal of the Electrochemical Society, 2007. **154**(5): p. B494-B499.
86. Mayrhofer, K.J.J., et al., *The Impact of Geometric and Surface Electronic Properties of Pt-Catalysts on the Particle Size Effect in Electocatalysis.* Journal of Physical Chemistry B, 2005. **109**(30): p. 14433-14440.
87. Mayrhofer, K.J.J., et al., *Measurement of Oxygen Reduction Activities Via the Rotating Disc Electrode Method: From Pt Model Surfaces to Carbon-Supported High Surface Area Catalysts.* Electrochimica Acta, 2008. **53**(7): p. 3181-3188.
88. Bett, J.A.S., Washingt.El, and K. Routsis, *Effect of Crystallite Size on Activity of Platinum Black for Cathodic Oxygen Reduction.* Journal of the Electrochemical Society, 1970. **117**(3): p. C118-&.
89. Bett, J. and Lundquis.J, *Platinum Crystallite Size Considerations for Electrocatalytic Oxygen Reduction.1.* Electrochimica Acta, 1973. **18**(5): p. 343-348.
90. Hulteen, J.C., et al., *Nanosphere Lithography: Size-Tunable Silver Nanoparticle and Surface Cluster Arrays.* Journal of Physical Chemistry B, 1999. **103**(19): p. 3854-3863.
91. Haynes, C.L. and R.P. Van Duyne, *Nanosphere Lithography: A Versatile Nanofabrication Tool for Studies of Size-Dependent Nanoparticle Optics.* Journal of Physical Chemistry B, 2001. **105**(24): p. 5599-5611.
92. Winzer, M., et al., *Fabrication of Nano-Dot- and Nano-Ring-Arrays by Nanosphere Lithography.* Applied Physics a-Materials Science & Processing, 1996. **63**(6): p. 617-619.
93. Lau, D. and S. Furman, *Fabrication of Nanoparticle Micro-Arrays Patterned Using Direct Write Laser Photoreduction.* Applied Surface Science, 2008. **255**(5): p. 2159-2161.
94. Sung, J., et al., *Nanoparticle Spectroscopy: Plasmon Coupling in Finite-Sized Two-Dimensional Arrays of Cylindrical Silver Nanoparticles.* Journal of Physical Chemistry C, 2008. **112**(11): p. 4091-4096.
95. Teo, K.B.K., et al., *Fabrication and Electrical Characteristics of Carbon Nanotube-Based Microcathodes for Use in a Parallel Electron-Beam Lithography System.* Journal of Vacuum Science & Technology B, 2003. **21**(2): p. 693-697.
96. Kishi, A. and M. Umeda, *Nano Peel-Off Fabrication Pattern with Polymer Overcoat Layer on Glassy Carbon Electrodes for Pt Electrodeposition.* Applied Surface Science, 2009. **255**(22): p. 9154-9158.
97. Hamley, I.W., *Nanotechnology with Soft Materials.* Angewandte Chemie-International Edition, 2003. **42**(15): p. 1692-1712.
98. Hamley, I.W., *Nanostructure Fabrication Using Block Copolymers.* Nanotechnology, 2003. **14**(10): p. R39-R54.

99. Krishnamoorthy, S., et al., *Tuning the Dimensions and Periodicities of Nanostructures Starting from the Same Polystyrene-Block-Poly(2-Vinylpyridine) Diblock Copolymer.* Advanced Functional Materials, 2006. **16**(11): p. 1469-1475.
100. Boyen, H.G., et al., *A Micellar Route to Ordered Arrays of Magnetic Nanoparticles: From Size-Selected Pure Cobalt Dots to Cobalt-Cobalt Oxide Core-Shell Systems.* Advanced Functional Materials, 2003. **13**(5): p. 359-364.
101. Glass, R., M. Moller, and J.P. Spatz, *Block Copolymer Micelle Nanolithography.* Nanotechnology, 2003. **14**(10): p. 1153-1160.
102. Spatz, J.P., et al., *Ordered Deposition of Inorganic Clusters from Micellar Block Copolymer Films.* Langmuir, 2000. **16**(2): p. 407-415.
103. Gu, Y., et al., *Aging Studies of Pt/Glassy Carbon Model Electrocatalysts.* Journal of the Electrochemical Society, 2009. **156**(4): p. B485-B492.
104. Black, C.T., et al., *Integration of Self-Assembled Diblock Copolymers for Semiconductor Capacitor Fabrication.* Applied Physics Letters, 2001. **79**(3): p. 409-11.
105. Guarini, K.W., et al., *Nanoscale Patterning Using Self-Assembled Polymers for Semiconductor Applications.* Journal of Vacuum Science & Technology B, 2001. **19**: p. 2784-8.
106. Bates, F.S. and G.H. Fredrickson, *Block Copolymers-Designer Soft Materials.* Physics Today, 1999. **52**(2): p. 32-8.
107. Han, E., et al., *Effect of Composition of Substrate-Modifying Random Copolymers on the Orientation of Symmetric and Asymmetric Diblock Copolymer Domains.* Macromolecules, 2008. **41**(23): p. 9090-9097.
108. Black, C.T., *Polymer Self-Assembly as a Novel Extension to Optical Lithography.* ACS Nano, 2007. **1**(3): p. 147-150.
109. Stoykovich, M.P. and P.F. Nealey, *Block Copolymers and Conventional Lithography.* Materials Today, 2006. **9**(9): p. 20-29.
110. Han, E., et al., *Photopatternable Imaging Layers for Controlling Block Copolymer Microdomain Orientation.* Advanced Materials, 2007. **19**(24): p. 4448-4452.
111. Mansky, P., et al., *Controlling Polymer-Surface Interactions with Random Copolymer Brushes.* Science, 1997. **275**(5305): p. 1458-1460.
112. Guarini, K.W., C.T. Black, and S.H.I. Yeuing, *Optimization of Diblock Copolymer Thin Film Self Assembly.* Advanced Materials, 2002. **14**(18): p. 1290-+.
113. Guarini, K.W., et al., *Process Integration of Self-Assembled Polymer Templates into Silicon Nanofabrication.* Journal of Vacuum Science & Technology B (Microelectronics and Nanometer Structures), 2002. **20**(6): p. 2788-92.
114. Black, C.T. and K.W. Guarini, *Structural Evolution of Cylindrical-Phase Diblock Copolymer Thin Films.* Journal of Polymer Science, Part A (Polymer Chemistry), 2004. **42**(8): p. 1970-5.
115. Conforti, P.F. and B.J. Garrison, *Electronic Structure Calculations of Radical Reactions for Poly(Methyl Methacrylate) Degradation.* Chemical Physics Letters, 2005. **406**(4-6): p. 294-299.